Breaching Flow Slides and the Associated Turbidity Currents
Large-Scale Experiments and 3D Numerical Modelling

Alhaddad, S.M.S.

DOI
10.4233/uuid:f41b33db-30ce-42d5-9cad-06d12c50d90f

Publication date
2021

Document Version
Final published version

Citation (APA)
Alhaddad, S. M. S. (2021). *Breaching Flow Slides and the Associated Turbidity Currents: Large-Scale Experiments and 3D Numerical Modelling*. [Dissertation (TU Delft), Delft University of Technology]. https://doi.org/10.4233/uuid:f41b33db-30ce-42d5-9cad-06d12c50d90f

Important note
To cite this publication, please use the final published version (if applicable).
Please check the document version above.

BREACHING FLOW SLIDES AND THE ASSOCIATED TURBIDITY CURRENTS

LARGE-SCALE EXPERIMENTS AND 3D NUMERICAL MODELLING

BREACHING FLOW SLIDES AND THE ASSOCIATED TURBIDITY CURRENTS

LARGE-SCALE EXPERIMENTS AND 3D NUMERICAL MODELLING

Proefschrift

ter verkrijging van de graad van doctor
aan de Technische Universiteit Delft,
op gezag van de Rector Magnificus Prof. dr. ir. T.H.J.J. van der Hagen,
voorzitter van het College voor Promoties,
in het openbaar te verdedigen op donderdag 7 januari 2021 om 10:00 uur

door

Said M. S. ALHADDAD

Civiel Ingenieur, Technische Universiteit Delft, Nederland,
geboren te Gaza, Palestina.

Dit proefschrift is goedgekeurd door de

promotor: prof. dr. W.S.J. Uijttewaal
copromotor: dr. R.J. Labeur

Samenstelling promotiecommissie:

Rector Magnificus,	voorzitter
Prof. dr. W.S.J. Uijttewaal,	Technische Universiteit Delft
Dr. R.J. Labeur,	Technische Universiteit Delft

Onafhankelijke leden:

Prof. dr. A. Bezuijen,	Universiteit Gent, België
Dr. J.T. Eggenhuisen,	Universiteit Utrecht
Prof. dr. M.J. Franca,	IHE, Technische Universiteit Delft
Prof. dr. M. Hicks,	Technische Universiteit Delft
Prof. dr. C. van Rhee,	Technische Universiteit Delft

Keywords:	Flow slide, breaching, turbidity current, sediment entrainment, pick-up function, erosion model, erosion rate, self-accelerating current, surficial slides, large eddy simulation
Printed by:	Ridderprint | www.ridderprint.nl
Front & Back:	Jim Wyers, Gympie Times.

ISBN 978-94-6366-345-8

An electronic version of this dissertation is available at
http://repository.tudelft.nl/.

When a person dies, all their deeds come to an end except three:
ceaseless charity,
beneficial knowledge,
and a pious child who prays for them.

Prophet Mohammed

CONTENTS

SUMMARY

Breaching Flow Slides and the Associated Turbidity Currents: Large-Scale Experiments and 3D Numerical Modeling

Underwater slope failure is a common problem in the fields of geotechnical, dredging and hydraulic engineering, posing a major risk to submerged infrastructure and flood defences along coasts, rivers, and lakes. The term 'flow slide' refers to a specific, complex failure mechanism of underwater slopes, which occurs when a substantial amount of sediment moves downslope and eventually redeposits, forming a milder slope. A distinctive feature of flow slides is that the sediment running downslope is transported as a sediment-water mixture rather than as a sediment mass, and thus it behaves as a viscous fluid. Breaching is a particular type of flow slide, described as a slow (~mm/s), gradual, retrogressive erosion of submerged slopes that are steeper than the soil internal friction angle. Breaching has remained unexplored until it was identified in the 1970s by the Dutch dredging industry as an important production mechanism for stationary suction dredgers. In that period, breaching was not known as a failure mechanism of underwater slopes outside of the field of dredging. In the Netherlands, breaching is now an important consideration in the safety assessments of dikes.

Breaching flow slides are accompanied by the generation of turbidity currents, which can be described as buoyancy-driven underflows generated by the action of gravity on the density difference between the water-sediment mixture and the ambient water. These currents pose a serious threat to submarine structures placed at the seafloor, such as oil pipelines and communication cables. Breaching-generated turbidity currents run over and directly interact with the eroding, submarine slope surface (breach face), thereby enhancing further sediment erosion. The investigation and understanding of this interaction are critical to understand and predict the failure evolution during breaching. This is an important consideration for avoiding the risks of breaching during dredging and for the design of effective mitigation measures to protect hydraulic structures. In this dissertation, the evolution of the breaching failure and the associated turbidity currents are investigated through large-scale laboratory experiments and numerical modelling.

This study begins by surveying the state-of-the-art knowledge of breaching flow slides, with an emphasis on the relevant fluid mechanics, providing a better insight into the physics and identifying the relevant knowledge gaps. Then, existing breaching erosion closure models were employed in combination with the three-equation model of Parker et al. (1986) and applied to a typical case of a breaching submarine slope. The sand erosion rate and hydrodynamic properties of the turbidity current were found to vary substantially between the erosion closure models, motivating further experimental studies on breaching flow slides, including detailed flow measurements, for validation purposes and improving the current understanding of the breaching phenomenon.

At the Laboratory of Fluid Mechanics of Delft University of Technology, a set of unique large-scale experiments was conducted in which various non-vertical initial breach faces were tested, providing the first quantitative data for such initial conditions. Direct measure-

ments of breaching-generated turbidity currents are thus provided, illustrating their spatial development and visualizing the structure of their velocity and sediment concentration. The analysis of the experimental results indicated that breaching-generated turbidity currents are self-accelerating; sediment entrainment and flow velocity enhance each other in a positive feedback loop. The turbidity currents accelerate downslope, and consequently the sand erosion rate increases downslope until a certain threshold, likely imposed by turbulence damping. This leads to the steepening of the breach face which induces the collapse of coherent sand wedges (surficial slides). These slides considerably enhance local sediment erosion and affect the hydrodynamics and thus increase the erosive capacity of the turbidity current. Even though breaching is a gravity-induced failure in the first place, the generated turbidity current seems to start dominating the failure just after its onset until the final deposition of the sediments. Owing to several difficulties encountered during the lab experiments, obtaining measurements of turbulence quantities of the flow was not possible. The lack of such measurements hampers the estimate of the flow-induced bed shear stress and hence the prediction of erosion during breaching. This motivated the use of an advanced 3D numerical model as a complementary tool to the experimental work, to gain additional insights into the behavior and structure of breaching-generated turbidity currents.

Large eddy simulations of breaching-generated turbidity currents were conducted, providing deeper insights into their hydrodynamics and physical structure. Through these turbulence-resolving simulations, it was shown that the proposed numerical tool can reasonably reproduce several distinctive aspects of the flow, such as the vertical density distribution, and the spatial development down the breach face. A limitation of the model is that it underestimates the thickness of the current. The numerical results confirm the self-accelerating behavior of breaching-generated turbidity currents as indicated by the experimental results. Considering the challenging conditions of breaching, a new breaching erosion closure model was proposed and validated using the series of the laboratory experimental data obtained within this study. Good agreement is observed between experimental and numerically predicted erosion rates. Breaching-generated turbidity currents are found to exhibit a self-similar behavior; velocity, concentration, Reynolds stress, and turbulent kinetic energy profiles take a self-similar shape. Based on a sensitivity analysis, sand erosion during breaching is found to be susceptible to the *in situ* porosity; the lower the *in situ* porosity, the higher the sand resistance to erosion.

The experimental measurements acquired within this study may be utilized for the validation of existing and new numerical models used to simulate breaching flow slides. These models, based on the findings of this research, must be capable of reasonably reproducing the hydrodynamics and sediment transport of turbidity currents. The self-accelerating behavior of this current implies that it is quite dangerous, and that breaching could be a triggering mechanism for sustained turbidity currents in deep water. The knowledge gained from this dissertation may help towards the design of robust mitigation measures against breaching flow slides and towards the optimization of the sand production process during dredging while minimizing the associated risk for the surrounding environments. In addition, it may lead to a more accurate interpretation of the process responsible for the encountered submarine slope failures.

SAMENVATTING

Bresvloeiingen en de Bijbehorende Troebelingsstromingen: Grootschalige Experimenten en 3D Numerieke Modellering

Het bezwijken van een onderwatertalud is een veelvoorkomend probleem in de geotechniek, bagger- en waterbouw, en vormt een groot risico voor onderwaterinfrastructuur en waterkeringen langs kusten, rivieren en meren. De term 'zettingsvloeiing' verwijst naar een karakteristiek, complex faalmechanisme van onderwatertaluds dat optreedt wanneer een aanzienlijke hoeveelheid sediment naar beneden stroomt en tenslotte een flauwer talud vormt. Een onderscheidend kenmerk van zettingsvloeiingen is dat het sediment, dat naar beneden vloeit, wordt getransporteerd als een sediment-watermengsel in plaats van een sedimentmassa en zich dus gedraagt als een viskeuze vloeistof. Bresvloeiing is een bepaald type zettingsvloeiing dat wordt beschreven als langzame (~mm/s), geleidelijke, terugschrijdende erosie van een onderwatertalud dat steiler is dan de inwendige wrijvingshoek van het desbetreffend materiaal. Bresvloeiing was een onbekend fenomeen totdat het in de jaren zeventig door de Nederlandse baggerindustrie werd geïdentificeerd als een cruciaal productiemechanisme voor stationaire zuigers. Buiten de baggerindustrie stond bresvloeiing in die periode niet bekend als een faalmechanisme van onderwatertaluds. Tegenwoordig is in Nederland bresvloeiing een doorslaggevend onderdeel bij de veiligheidstoetsing van dijken.

Bresvloeiingen gaan gepaard met het teweegbrengen van troebelingsstromingen, die worden gekenmerkt als dichtheid-gedreven stromingen. Deze stromingen worden opgewekt door de werking van de zwaartekracht op het dichtheidsverschil tussen het water-sedimentmengsel en het water eromheen. Voor objecten die op de zeebodem zijn geplaatst, zoals oliepijpleidingen en communicatie kabels, vormen deze stromingen een groot gevaar. Bresvloeiing-gegenereerde troebelingsstromingen stromen langs en staan in direct contact met het eroderende, onderzeese taludvlak (bresvlak), waardoor verdere erosie van het sediment versterkt wordt. Het onderzoeken en het begrijpen van deze interacties zijn van cruciaal belang om het faalmechanisme tijdens bresvloeiing te begrijpen en te voorspellen. Daarnaast zijn de onderzoeksresultaten van belang om risico's te vermijden tijdens baggeren, om doeltreffende maatregelen te ontwerpen voor de verdere bescherming van waterkeringen. In dit proefschrift zijn het faalmechanisme van bresvloeiing en de bijbehorende troebelingsstromingen onderzocht middels grootschalige laboratoriumexperimenten en numerieke modellering.

Het eerste onderdeel van dit onderzoek bestaat uit het in kaart brengen van de meest recente kennis over bresvloeiingen, met nadruk op de essentiële vloeistofmechanica, zodat een beter inzicht wordt verkregen in de fysica en relevante kennisleeinten geïdentificeerd kunnen worden. Vervolgens zijn bestaande erosiemodellen voor bresvloeiing gebruikt in combinatie met een model van Parker et al. (1986) en toegepast op een typisch geval van bresvloeiing in een onderwatertalud. De snelheid van het eroderen van het zand en de hydrodynamische eigenschappen van de troebelingsstromingen bleken aanzienlijk te verschillen tussen de erosiemodellen, wat nader experimenteel onderzoek naar bresvloeiingen moti-

veerde. Hierbij horen ook gedetailleerde metingen van de stroming voor validatie doeleinden en het vergroten van de huidige kennis over bresvloeiing.

In het waterlaboratorium van de Technische Universiteit Delft is een reeks unieke, grootschalige experimenten uitgevoerd, waarbij verschillende initiële, niet-verticale onderwatertaluds getest zijn. De experimentele data waren de eerste ooit voor dergelijke begincondities. De indirecte metingen van bresvloeiing-gegenereerde troebelingsstromingen geven inzicht in de ruimtelijke ontwikkeling ervan, en in de structuur van de stroomsnelheid en sedimentconcentratie. Op basis van de analyse van de experimentele data is gevonden dat bresvloeiing-gegenereerde troebelingsstromingen zichzelf versnellen; het meevoeren van het sediment en de stroom versterken elkaar in een positieve terugkoppeling. De troebelingsstromingen versnellen talud afwaarts en ten gevolge hiervan neemt de snelheid van het eroderen van het zand toe tot een bepaalde drempelwaarde, wat waarschijnlijk samenhangt met demping van de turbulentie. Op den duur leidt dit proces tot het steiler worden van het bresvlak en het instorten van coherente zandwiggen (surficial slides). Deze zandwiggen verhogen de lokale erosie van het sediment behoorlijk en beïnvloeden de hydrodynamica en daarmee de erosiecapaciteit van de troebelingsstroming. Hoewel bresvloeiing hoofdzakelijk een door de zwaartekracht gedomineerd faalmechanisme is, lijkt de bresvloeiing-gegenereerde troebelingsstroming het bezwijkproces te domineren tot de uiteindelijke afzetting van de sedimenten. Door verscheidene problemen die tijdens de laboratoriumexperimenten werden ondervonden, was het binnen dit onderzoek niet mogelijk om metingen van de turbulentie van de stroming te verkrijgen. Het ontbreken van dergelijke metingen bemoeilijkt de schatting van de stromingsgeïnduceerde bodemschuifspanning en daarmee de voorspelling van de erosie tijdens bresvloeiing. Dit gaf aanleiding tot de inzet van een geavanceerd 3D numeriek model als aanvullend instrument op het experimentele werk.

Large eddy simulaties van bresvloeiing-gegenereerde troebelingsstromingen werden uitgevoerd, waardoor nieuwe inzichten werden verkregen in de hydrodynamica en de fysieke structuur van deze stromingen. Het voorgestelde numerieke model bleek de verschillende aspecten van de stroming redelijk te kunnen reproduceren, waaronder de verticale dichtheidsverdeling en ruimtelijke ontwikkeling langs het bresvlak. Een beperking van het model is dat de laagdikte van de troebelingsstroming onderschat wordt. De resultaten uit het numerieke model bevestigen het zelfversnellende gedrag van bresvloeiing-gegenereerde troebelingsstromingen zoals gevonden in de analyse van de experimentele data. Hiertoe werd een nieuw bresvloeiing-erosiemodel opgesteld en gevalideerd met behulp van de experimentele data. Overeenkomstig de metingen blijken de brekende troebelingsstromingen, de snelheid, dichtheid, Reynoldsstress en turbulente kinetische energieprofielen gelijkvormig. Op basis van een gevoeligheidsanalyse uitgevoerd met het model blijkt dat erosie van zand tijdens bresvloeiing afhankelijk is van de porositeit; hoe lager de in situ porositeit, hoe hoger de weerstand van het zand tegen erosie.

De experimentele data die binnen dit onderzoek verkregen zijn, kunnen worden gebruikt voor de validatie van nieuwe numerieke modellen die ontwikkeld worden om bresvloeiingen te simuleren. Met de bevindingen van dit onderzoek kunnen deze modellen verder verbeterd worden zodat de hydrodynamica en het sedimenttransport van bresvloeiing beter voorspeld kunnen worden. Op basis van de bevindingen van dit onderzoek moeten deze modellen in staat zijn om de hydrodynamica en het sedimenttransport van bresvloeiingen voldoende nauwkeurig te reproduceren. Het zelfversnellingsgedrag van de troebelingsstroming impli-

ceert dat het aanzienlijk gevaarlijk is en dat aanhoudende troebelingsstromingen in diep water geïnitieerd kunnen worden door bresvloeiingen. De nieuwe kennis die uit dit proefschrift is verkregen, kan verder gebruikt worden bij het ontwerpen van robuuste maatregelen tegen bresvloeiing-gegenereerde troebelingsstromingen en bij het optimaliseren van het zandproductieproces tijdens baggeren, waarbij het bijbehorende risico voor de omgeving geminimaliseerd kan worden. Daarnaast voorziet het in een nauwkeurigere interpretatie van het proces dat verantwoordelijk is voor het falen van onderwatertaluds.

1

INTRODUCTION

1.1. BACKGROUND

Slope failures are ubiquitous in both subaerial and underwater environments, causing severe damage all over the world. Therefore, the topic of slope failures receives the attention of researchers in a broad area of scientific fields such as soil mechanics, natural hazards, sedimentology, and dredging and hydraulic engineering.

Referring to the slope movement, the term 'land slide' is popularly encountered in the literature as the overarching term for all the various types of mass transport downslope. Under this generic term, the particular term 'flow slide' is used to refer to slope failures occurring underwater. To avoid conceptual and nomenclatural problems, flow slide is specifically defined here as the downslope movement of a large amount of sediments, present on an underwater slope. These sediments deposit eventually, creating a milder slope than the pre-event one. A key feature of flow slides is that the sediment failing downslope is transported as a sediment-water mixture rather than as a sediment mass and thus it behaves as a viscous fluid. In other words, the behavior of the failing sediment suddenly changes from solid-like to fluid-like.

Flow slides pose a severe risk for submerged infrastructure, and coastal, river and estuarine flood defences (*Koppejan et al.*, 1948), as they can altogether undermine a hydraulic structure, resulting in significant damage. They could also result in a high number of casualties as that documented for some historical flow slides (*De Jager*, 2018). The common occurrences of flow slides have been well documented in the Netherlands and in particular in the southwestern delta region (Zeeland), where hundreds of flow slides have taken place since the nineteenth century (*Van Duinen et al.*, 2014). This has resulted in the destruction of some flood defenses and consequently the loss of lives and lands (*Mastbergen et al.*, 2019). Figure 1.1 shows the damage caused by flow slide events that took place in two different years in Zeeland. Owing to the unpredicted nature of flow slides and to the fact that flow slides

Some parts of this chapter have been published in Alhaddad, S., Labeur, R. J., and Uijttewaal, W. (2021). Preliminary Evaluation of Existing Breaching Erosion Models. In Proceedings of the tenth international conference on Scour and Erosion, Arlington, Virginia, October 17-20 2021.

usually remain entirely underwater, the onset and active phase of natural events have never been monitored. The available observations were made after the flow slides had already finished. This observational impediment, together with the complexity of flow slides, has resulted in a poor understanding of the physical processes governing them.

Figure 1.1: Damage resulting from flow slide events in Zeeland, the Netherlands in 1971 (*Mastbergen and Schrijvershof*, 2016) (**left**) and in 1964 (**right**) (*Mastbergen et al.*, 2019).

Two end members of flow slides are distinguished in the literature: liquefaction flow slides and breaching flow slides. The former occurs in loosely-packed sand, which shows a contractive behavior under shear forces; the soil structure collapses abruptly and a large amount of the soil body flows downslope. The latter, on the other hand, does not take place as an abrupt collapse. Rather, sand grains peel off particle by particle, forming a turbidity current propagating over the slope surface (breach face) (*Van Rhee and Bezuijen*, 1998). In fact, breaching is a less-recognized type of failure. This has resulted in the inaccurate interpretation of the process behind many slope failures as liquefaction (*Van Den Berg et al.*, 2002; *Mastbergen et al.*, 2019). Recent studies, nevertheless, have revealed that breaching, rather than liquefaction, is the dominant failure process in underwater slopes of fine sand (*Van den Berg et al.*, 2017) and the main driver of observed flow slides in nature (*Beinssen and Mastbergen*, 2017). This implies that expanding the current knowledge about the breaching failure mechanism is a matter of urgency and significance.

It is to be noted that the term breaching here does not refer, as conventionally, to the phenomenon of the eventual failure of hydraulic structures due to overtopping. Instead, it denotes the relatively slow, gradual, retrogressive erosion of submerged slopes steeper than the soil internal friction angle. Breaching has escaped the attention of researchers, because it was confused with soil liquefaction (*Eke et al.*, 2011). This is due to the fact that both failure modes produce very similar post-event morphology (see Figure 1.2). Currently, in the Netherlands, breaching is critically involved in the safety assessments of dikes (*Van Duinen et al.*, 2014).

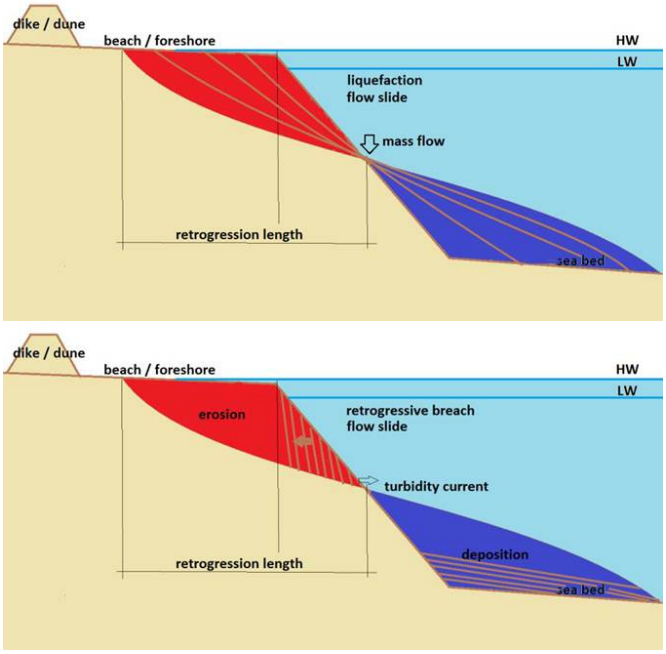

Figure 1.2: A schematic representation of the pre-event and post-event morphology for a liquefaction flow slide (**top**) versus a breaching flow slide (**bottom**) (*Mastbergen et al.*, 2014).

Unlike static liquefaction, breaching is mostly encountered in densely-packed sand, which dilates under shear forces (*Van Rhee*, 2015). Dilatant sand undergoes an increase in pore volume under shear deformation, leading to the generation of negative pore pressure, which considerably retards the erosion process. Owing to the pressure difference, an inward hydraulic gradient is generated, forcing the ambient water to flow into the pores, releasing the negative pressure. As a consequence, the sand particles located at the sand-water interface become unstable and gradually peel off, almost particle by particle. These particles mix with the ambient water, creating a sustained turbidity current running along the breach face and then down the slope toe (*Eke et al.*, 2011). In addition to the particle-by-particle failure, *Van Rhee and Bezuijen* (1998) and *You et al.* (2014) observed a periodic collapse of coherent sand wedges, termed surficial slides, in their experiments. The current understanding of these slides remains scant. Breaching can last for many hours, propagating towards nearby or remote coastlines or river banks and hence posing a significant risk (Figure 1.3). Moreover, this mode of failure could cause instabilities during the construction of submerged slopes (*Van Rhee*, 2015). Such hazardous situations could be avoided by a good understanding of the triggering mechanisms and the evolution of breaching events.

1

Figure 1.3: Ongoing breaching flow slides: Amity Point captured on 18 August 2014 (**left**), Ameland Island Southwest, the Netherlands, 2017 (**right**) (*Mastbergen et al.*, 2019).

Turbidity currents are buoyancy-driven underflows that can be observed in oceans, lakes, estuaries, and reservoirs. The fluid-sediment mixture within the turbidity current has a density higher than the density of the ambient fluid, resulting in an excess hydrostatic pressure, which drives the current downstream. The presence of sediments inside the current is the reason for the higher density of the current. When the turbidity current propagates downslope, it interacts simultaneously with the bed at the bottom boundary and with the ambient fluid at the upper boundary, producing turbulence (*Salinas et al.*, 2019). These currents are one of the primary sediment transport mechanisms on Earth, delivering prodigious amounts of sediments from shallow to deep water. Moreover, they pose a serious threat to submarine structures placed at the seafloor, such as oil pipelines and communication cables that transfer the majority of the data throughout the world (*Carter et al.*, 2014; *Paull et al.*, 2018). Thus, breaching flow slides can pose a hazard directly and indirectly to neighbouring or distant submerged infrastructure.

Unlike turbidity currents generated by other triggering mechanisms, breaching-generated turbidity currents do not have a distinctive propagating front at the breach face (Figure 1.4). This is because the sand particles peel off everywhere along the slope, leading to the simultaneous formation of a current from the upstream end until the breach base (*Eke*, 2008). This current induces shear stress over the breach face, thereby promoting sediment erosion and thus strengthening itself (*Mastbergen and Van Den Berg*, 2003); when more sediments are suspended in the current, it can become denser and thus faster. In addition, the periodic surficial slides disintegrate and are fed to the turbidity current, increasing its erosive capacity even more (*Van Den Berg et al.*, 2002).

Quantitative data of the erosion caused by breaching-generated turbidity currents is still missing, leaving the question open whether it could play a considerable role in the problem of breaching flow slides. Moreover, very little is known about the interaction of turbidity currents with slope surfaces composed of densely-packed particles, as in a breach face. In this case, dilatancy plays a considerable role in retarding the erosion process (*Bisschop et al.*, 2016). The conventional sediment entrainment relations of turbidity currents (e.g., *Akiyama and Fukushima* (1985); *Garcia and Parker* (1993)) were developed for a current traveling over mildly sloping beds composed of loosely-packed sediment. This means that they are not appropriate for breaching. Nevertheless, a few attempts were made to develop a breaching

erosion closure model accounting for the sediment entrainment by turbidity currents during breaching (i.e., *Mastbergen and Van Den Berg* (2003); *Van Rhee* (2015)). A key feature of these erosion closure models is that they account for a sloping bed steeper than the internal friction angle as well as the retarded erosion by the dilative behavior of the granular material. However, these erosion closure models have never been validated against real data for breaching including measurements of breaching-generated currents. Furthermore, these erosion closure models do not account for the influence of surficial slides on sediment erosion.

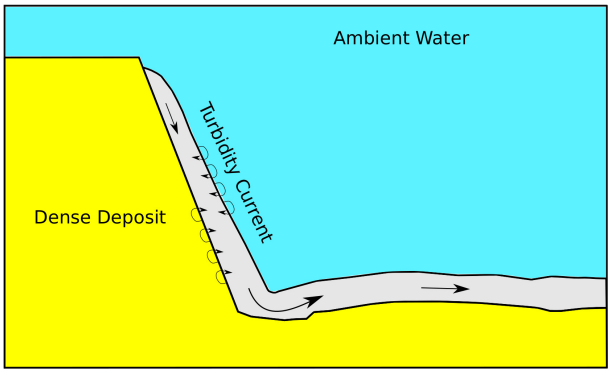

Figure 1.4: Schematic representation of breaching flow slides and the accompanying turbidity current.

Breaching has remained unexplored until it was identified by the Dutch dredging industry in the 1970s. It is considered an effective production mechanism for stationary suction dredgers. This explains why the vast majority of the state-of-the-art knowledge of breaching comes from dredging research (e.g., *Breusers* (1977); *Van Rhee and Bezuijen* (1998)). The sand mining process with a suction dredger is demonstrated in Figure 1.5; the suction pipe is inserted into the bed, forming a very steep slope around the suction mouth. As a result, the breaching process starts and subsequently turbidity currents generate, which work as the carrier of sand from the breach face to the suction mouth. The sand is sucked into the pipe and delivered to the dredger, while the steep slope keeps traveling in a radial direction. This is an efficient method of sand mining, since the suction pipe does not have to move towards the breach face during sand collection. When the suction is halted at the end of the dredging process, the breaching failure may continue for several hours without interruption until a breach face milder than the internal friction angle of sand is formed (*Van Den Berg et al.*, 2002; *Eke et al.*, 2011). This procedure may, however, pose a major risk for the stability of nearby infrastructure and foreshores. To avoid such horrific risks, a deeper insight into the evolution of breaching is required.

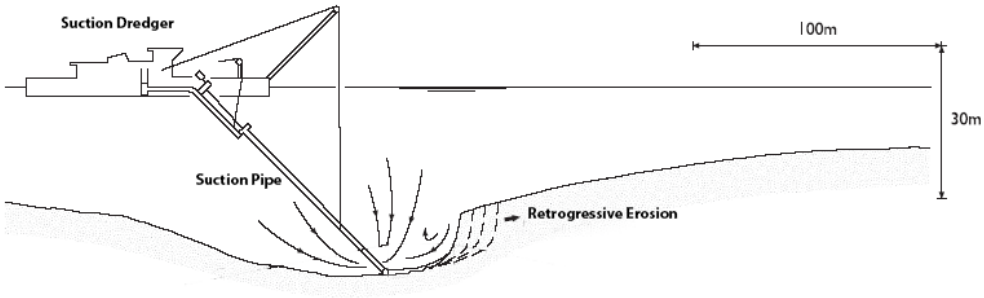

Figure 1.5: Sand-water flow from the breach face to a stationary suction dredger (modified from *Van Den Berg et al.* (2002)).

1.2. MPM-FLOW PROJECT

The ability to predict the risk of flow slides is a necessary consideration for the design, construction, maintenance and safety assessment of flood defenses. This necessity is currently more prominent in the light of the influence of climate change, in particular the sea level rise, on low-lying coastal areas around the globe. Moreover, the prediction of the evolution of breaching is important, as a breaching failure might not terminate underwater (during sand mining), propagating instead towards nearby infrastructure or foreshores. To this end, physical lab experiments must be carried out. However, such experiments are often difficult to do and costly, as they require sufficiently large scales and thus large test facilities. Numerical modeling is an attractive alternative, serving as a virtual laboratory and allowing the test of various what-if scenarios. To date, detailed numerical modeling of flow slides has not been successful. This provides a motivation for the development of advanced numerical tools that can deal with flow slides.

This research is part of a 4-PhD interdisciplinary project called 'Understanding Flow Slides in Flood Defences (MPM-Flow)'. This project aims to develop an integral numerical solution method to simulate flow slides through the improvement of a numerical technique called Material Point Method (MPM) (*Sulsky et al.*, 1994; *Kafaji*, 2013). To this end, a thorough understanding of the underlying physical processes of flow slides is a key research priority. Unfortunately, the current understanding of these is still poor, due to the complexity of flow slides involving both geotechnical and hydraulic aspects.

To pursue the goal of the interdisciplinary project, four PhD students conducted individual complementary research focused on a particular aspect of the problem at hand. *Wobbes* (2019) focused on the mathematical aspect of the MPM, attempting at the improvement of mathematical and numerical solutions for physics-based models used with the MPM. *Silva* (2020) mainly focused on the geotechnical aspects of flow slides. To gain a deeper insight into the soil mechanical processes of flow slides, *Silva* (2020) conducted small-scale laboratory experiments, focusing on the influence of sand characteristics on the type, behaviour and evolution of soil failure. Her research resulted in a detailed data set concerning the soil body, which can be used for validation purposes of numerical models. Marco Bolognin primarily focused on the validation of the MPM results against available data of slope failures. He also carried out field experiments, obtaining direct measurements of flow slides, which were used

to validate his simulation results obtained by the MPM (personal communication).

As noted before, flow slides involve fluid mechanical processes and this is where the present research comes into play. Soil movement triggers turbulent soil-water flow, which travels over the eroding slope surface. Detailed data of velocities and concentrations of this flow are key for the validation of the dedicated numerical models, among which is the MPM. More importantly, understanding the underlying hydraulic processes and the interaction between the turbulent flow and slope surface are crucial to identify the numerical improvements needed to the MPM to properly simulate flow slides. The main objective of this study is outlined in the next section.

1.3. OBJECTIVES AND RESEARCH QUESTIONS

The objective of the current study, in general, is to expand the current knowledge about the hydraulic aspects of breaching flow slides and, in particular, to develop an insightful understanding of the two-way coupled interaction between the breaching-generated turbidity currents and the breach face. To this end, the following key research questions are to be answered:

1. How do breaching-generated turbidity currents evolve along the breach face?

2. What is the influence of turbidity currents on the breaching process?

3. Can we develop an erosion closure model that adequately predicts the erosion during breaching? How should it be formulated?

In the process of answering these research questions, we aim at developing a better understanding of the failure evolution during breaching flow slides.

1.4. METHODOLOGY

Direct measurements of breaching-generated turbidity currents are crucial for understanding the coupled interaction between the turbidity current and the slope surface, as well as for the validation of numerical models. Such measurements are also the key for the development of advanced breaching erosion closure models in order to improve the reliability of numerical simulations. However, there is insufficient data available disclosing the velocity distribution or sediment concentration in these currents. This is because these currents have proven very difficult to measure directly in the field as well as in the laboratory. The complexity of monitoring them in the field can be attributed to the fact that breaching events are still unpredictable and the ensuing turbidity currents are sufficiently powerful to damage the measuring equipment deployed in their track. On the other hand, the difficulty of obtaining laboratory data is mainly associated with the physical structure of these currents. For instance, they have high sediment concentrations, and they are very thin (few centimeters), requiring advanced, high-resolution measuring instruments. To answer Question 1 and Question 2, novel, large-scale, physical model experiments on breaching flow slides will be conducted. In these experiments, a wide range of initial slope angles will be tested, so as to provide the first experimental data for such initial conditions. Measurements of flow thicknesses, velocities, and sediment concentrations will be considered, to study the spatial and temporal evolution of the turbidity currents and the underwater slope morphology.

The validation of the breaching erosion closure models used in the literature (i.e., *Mastbergen and Van Den Berg* (2003); *Van Rhee* (2015)) was hampered by the paucity of direct measurements of breaching-generated turbidity currents. Having performed large-scale lab experiments on breaching flow slides, quantitative data of breaching-generated turbidity currents and erosion rates will be available. These measurements will be utilized to provide the first insights into the performance of the existing breaching erosion closure models. In the case that the existing erosion closure models are not capable of sufficiently predicting the erosion rate, an existing erosion closure model will be adopted and extended to improve its erosion predictability. Nevertheless, it is expected that the experimental data, which will be obtained within this study, will not be sufficient to infer certain necessary quantities, such as shear stresses and turbulence. Therefore, an existing three-dimensional (3D), turbulence-resolving numerical model will be extended to suit the specific conditions of breaching. The main advantage of such a model over the lab experiments is that it provides access to all flow quantities everywhere in the considered case. The model, once validated against the experimental data, will be used to verify the proposed erosion closure model and to complement the experimental work. Through the numerical simulations, the applicability and validity of the numerical model will be tested. In addition, limitations of the model in characterizing the breaching-generated turbidity currents will be documented. Following this methodology, Question 3 can be answered.

Not only will the knowledge obtained within the present research improve our understanding of the nature of the breaching failure, and the structure and behavior of the accompanying turbidity currents, but it will also point out the capabilities required from the MPM to properly simulate breaching flow slides. As a result, key directions for future research and development of MPM can be defined.

1.5. DISSERTATION OUTLINE

This dissertation is structured as follows. Chapter 2 surveys the state-of-the-art knowledge of breaching flow slides and presents a detailed explanation of the main associated physical processes, from the triggering mechanism up to the end of the failure event. This aims to provide a better insight into the physics and to identify the relevant knowledge gaps. In addition, existing breaching erosion closure models are employed in combination with the three-equation model of *Parker et al.* (1986) and applied to a typical case of a breaching subaqueous slope. This demonstrates the implications of using different breaching erosion closure models for the sand erosion rate and the hydrodynamics of breaching-generated turbidity currents. This also serves as a motivation for carrying out new experimental studies on breaching flow slides.

In Chapter 3, the experimental setup and results of large-scale breaching experiments are presented. These experiments are carried out in a 0.22 m wide, 2 m high breaching tank in which the initial slope angle of the sand can be varied. High-resolution, one-dimensional visualization of flow fields is provided, thereby yielding the first quantitative visualization of velocity and concentration profiles of a breaching-generated turbidity current. Additionally, the temporal morphological evolution of the breach face is studied. Furthermore, an analysis of the surficial slides is carried out, attempting to understand the reason behind their occurrence.

Chapter 4 presents numerical large eddy simulations of breaching-generated turbidity currents. Through these simulations, the chapter considers the validity, applicability and

advantage of the proposed numerical model for the investigation of the flow characteristics. Furthermore, a breaching erosion closure model is proposed and validated using the series of laboratory experimental data presented in Chapter 3. Numerical results are discussed, in particular, those concerning the velocity, density and turbulence structure of breaching-generated turbidity currents as well as the associated sediment erosion.

In an integral way, Chapter 5 discusses the results presented in Chapters 2-4 and presents the potential implications of their findings. This dissertation ends with Chapter 6, where the main conclusions are drawn and some recommendations are provided for future studies on breaching flow slides.

2

THE STATE-OF-THE-ART KNOWLEDGE

This chapter starts with surveying the state-of-the-art knowledge of breaching flow slides, with an emphasis on the relevant fluid mechanics. The governing physical processes of breaching flow slides are explained. The chapter highlights the important roles of the associated turbidity current and the surficial slides in increasing the erosion rate of sediment. It also identifies the shortcomings of the current breaching erosion closure models. Then, the three-equation model of Parker et al. (1986) is utilised to describe the coupled processes of breaching and turbidity currents. For comparison's sake, the existing breaching erosion closure models are considered: Breusers (1977), Mastbergen and Van Den Berg (2003), and Van Rhee (2015). The sand erosion rate and hydrodynamics of the current vary substantially between the erosion closure models. Crucially, these erosion closure models do not account for the surficial slides, nor have they been validated due to the scarcity of data on the associated turbidity current. The findings of this chapter motivate further experimental studies, including detailed flow measurements, to develop an advanced erosion closure model compatible with the problem's conditions. This will improve the fidelity of numerical simulations. Finally, some key future directions are defined for research on this topic.

This chapter has been published as Alhaddad, S., Labeur, R. J., and Uijttewaal, W. (2020). Breaching Flow Slides and the Associated Turbidity Current. Journal of Marine Science and Engineering, 8 (2), 67. https://doi.org/10.3390/jmse8020067

2.1. INTRODUCTION

Submerged slope failure is a common problem in both geotechnical and hydraulic engineering, causing worldwide significant damages. The phenomenon of flow slide takes place when a large amount of underwater sediment moves downslope and eventually redeposits, creating a milder slope. The term "flow slide" stems from the fact that the sediment failing from the slope is transported as a sediment-water mixture and not as a sediment mass (*Beinssen and Mastbergen*, 2017). Flow slides pose a severe risk for submerged infrastructure, and coastal and river flood defences, as they can completely undermine a hydraulic structure (see Figure 2.1). Besides, flow slides of submerged slopes are an important production mechanism in dredging activities, possibly threatening the stability of nearby infrastructure or foreshores. The assessment of the risk of flow slides is important for the construction and reinforcement of flood defences (*Alhaddad et al.*, 2019).

The existing literature reports many historical cases of large submarine flow slides worldwide (e.g., *Koppejan et al.*, 1948; *Kramer*, 1988; *Silvis and Groot*, 1995; *Mastbergen et al.*, 2019). There is a long history of flow slide events in the Netherlands (*Mastbergen et al.*, 2015), particularly in the southwestern estuary of the Netherlands (Zeeland), where hundreds of flow slides have been observed since 1800 (*Van Duinen et al.*, 2014). However, the observations were made after the flow slides had already occurred, as their timing is unpredictable, implying that the temporal development of the failure was not monitored. Flow slides have been widely studied through post-event field observations, lab experiments, and numerical models, but are still not sufficiently understood. This is because they exhibit a complicated failure mechanism, including both geotechnical and hydraulic processes.

Figure 2.1: Damage to a river dike caused by a flow slide, from US Army Corps of Engineers (**left**) (*Rogers*, 2012). A large collapse of beach at Inskip Point in Queensland due to a breaching event, from Rainbow Beach Helicopters Australia (**right**) (*BBC*, 2018) .

It was common to consider flow slides to be caused by soil liquefaction occurring in loose sand. In recent years, however, flow slides have also been observed in dense sand induced by a less-known failure mechanism termed breaching. Liquefaction is a process by which the soil structure collapses abruptly after an increase in pore water pressure, which in turn results in a dramatic reduction of the effective stress and the associated shear resistance. Consequently, the soil body flows downslope, behaving as a viscous fluid. Fine, loosely-packed sand is more susceptible to static liquefaction due to its contracting behavior under shear forces. When loosely-packed sand is subjected to shear force, the grains tend to a denser packing, forcing the pore water out of the pores (Figure 2.2a), which increases the pore

pressure and reduces the effective stress (*Schiereck and Verhagen*, 2012). Liquefaction usually starts near the slope toe, leading to a retrogressive failure of the entire slope (*Torrey III*, 1988). The time scale of a static-liquefaction flow slide is short, probably a matter of seconds or minutes (*Van Rhee*, 2015). In contrast, breaching occurs slowly and perhaps lasts for several hours or even longer than one day, depending on the slope geometry (*Weij et al.*, 2016).

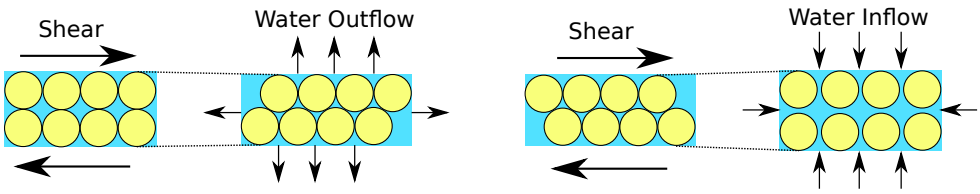

Figure 2.2: behavior of loosely-packed sand (**left**) versus densely-packed sand (**right**) under shear force.

Even though the two sub-mechanisms, liquefaction and breaching, are fundamentally different and the failure evolution over time is also different, they both result in a flowing soil-water mixture and a very similar post-event morphology. This implies that it is challenging to know the extent to which the two sub-mechanisms played a role in any flow slide event observed. Recent studies, however, have indicated that the dominant failure process in submerged slopes of fine sand (*Van den Berg et al.*, 2017) and the main trigger of observed flow slides is breaching (*Beinssen and Mastbergen*, 2017). This conclusion suggests that it is important to gain a deeper insight into the breaching failure mechanism.

This chapter sheds light on breaching flow slides and presents a detailed explanation for the main associated physical processes, from the triggering mechanism up to the end of the failure event. The aim is to provide a better insight into the physics and to identify the relevant knowledge gaps. Existing breaching erosion closure models were employed in combination with the three-equation model of *Parker et al.* (1986) and applied to a typical case of a breaching subaqueous slope. That shows the implications of using different breaching erosion closure models for the sand erosion rate and the hydrodynamics of breaching-generated turbidity currents. As a result, this chapter provides evidence that advanced breaching erosion closure models are required, and thus, suggests further experimental studies on breaching flow slides. Finally, some open questions are posed and key future directions are defined for research on this fascinating topic.

2.2. PHENOMENOLOGY
2.2.1. BREACHING FLOW SLIDES

Breaching is a common term in hydraulic engineering, mostly referring to the ultimate failure caused by the overtopping of dams, embankments, and sand barriers (*Eke et al.*, 2011), but it is used here in a more restrictive manner. Specifically, it is a gradual retrogressive failure of a very steep subaqueous slope, which is steeper than the angle of repose (*Van Den Berg et al.*, 2002). The Dutch dredging industry in the 1970s first identified breaching as an important production mechanism for stationary suction hopper dredgers. Currently, breaching is incorporated into corresponding safety assessments of dikes in the Netherlands, as it is an important failure mechanism (*Van Duinen et al.*, 2014).

Breaching takes place in dense sand, as it shows dilative behavior under shear forces (*Van Rhee and Bezuijen*, 1998; *Van Den Berg et al.*, 2002). Dilatancy refers to the volume increase of a granular material, during shear deformation, resulting from the increase in pore volume. This leads to a negative pore pressure, and hence an increase in the effective stress. Consequently, the erosion process is significantly retarded. The pressure difference involves an inward hydraulic gradient, forcing the ambient water to flow into the pores (Figure 2.2b). This restores the hydrostatic pressure, and thus only the particles located at the sand–water interface are destabilised and fall downslope one by one. These particles are suspended in water and form a turbulent, sand-water mixture flow, referred to as a turbidity current, propagating over and interacting with the breach face (*Eke et al.*, 2011; *Van den Ham et al.*, 2014).

During the particle-by-particle failure, the negative pore pressure dissipates locally, weakening the sand near the sand–water interface and leading to a thin surficial slide (a collapse of a coherent sand wedge), which leads to an abrupt drop in the pore pressure. This reinforces the sand deposit and converts the failure process back to particle-by-particle failure. In large-scale flume experiments on breaching, *Van Rhee and Bezuijen* (1998) observed the occurrence of surficial slides. The variant involving particle-by-particle failure and surficial slides was termed "dual-mode slope failure" by *You et al.* (2014). However, *Van den Berg et al.* (2017) did not agree with this term and considered it misleading, debating that the particle-by-particle failure and surficial slides are inherent properties of breaching and strongly linked to each other.

Experimental investigation carried out by *Van Rhee and Bezuijen* (1998) showed that two types of breaching can be distinguished: stable and unstable (Figure 2.3). The breaching process is considered unstable when the face of the steepening slope increases in height over time, leading to uncontrolled retrogressive failure of the slope. Stable breaching is characterised by the fact that the height of the breaching face decreases over time and disappears quickly. Whether the breaching is stable or unstable relies on the initial breach height and slope angle, and the sand characteristics (*Van Rhee*, 2015).

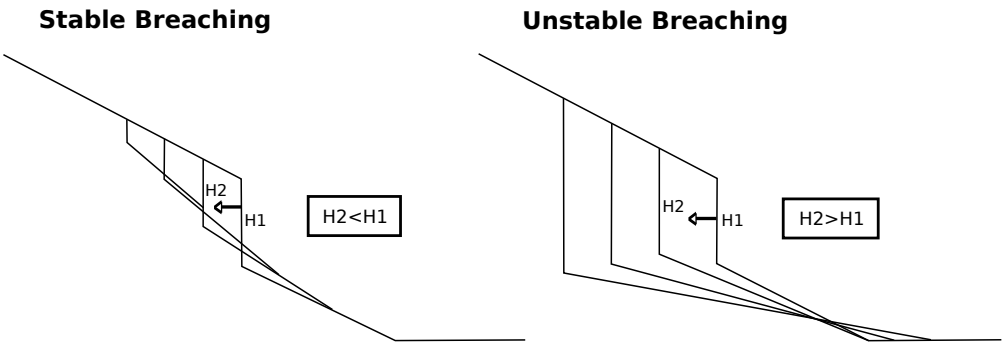

Figure 2.3: Schematic illustration of the two types of breaching, stable breaching (**left**) and unstable breaching (**right**); H is the breach height and the horizontal axis represents time (adapted from *Van Rhee* (2015)).

If the subaqueous slope is steeper than the angle of repose, the downslope component of gravitational force is greater than the sand's shear resistance. In such a case, retrogressive erosion occurs until a slope milder than the angle of repose is formed, even if the flow-induced shear stress is negligible. Due to the generation of a turbidity current, an extra bed-shear stress develops and the erosion rate increases (*Mastbergen and Van Den Berg*, 2003). The following subsection presents an overview of turbidity currents and their importance in sediment transport, in order to pave the way for the description of the role of turbidity currents in breaching flow slides and identifying the relevant knowledge gaps.

2.2.2. TURBIDITY CURRENT

Turbidity currents belong to the greater group of gravity-driven flows, the overarching term for flows driven by gravitational forces resulting from the density gradient in a fluid. Traditionally, turbidity currents are defined as "particle-laden gravity-driven underflows in which the particles are largely or entirely suspended by fluid turbulence" (*Meiburg and Kneller*, 2010). This turbulence is generated due to the ongoing motion of current over the lower boundary of the sediment bed and the shear stress generated at the upper boundary of the current. The motion of this current is generated by the density difference between the sediment-water mixture and the ambient water (*Meiburg and Kneller*, 2010).

Turbidity currents can be encountered in the oceans, lakes, estuaries, and reservoirs (*Islam et al.*, 2008; *Liu et al.*, 2012). They are an important consideration for the management of siltation and water quality in reservoirs and lakes (*Hu and Cao*, 2009). In fact, turbidity currents represent an important sediment transport mechanism, as they carry sediment from the continental shelves towards the deep sea (*Piper and Normark*, 2009). Therefore, these currents are considered to be the reason for the excavation of many submarine canyons and fans (*Pirmez and Imran*, 2003). According to *Talling et al.* (2015) and *Zordan et al.* (2017), the current understanding of bed erosion by turbidity currents remains very limited. These currents can travel at surprisingly swift velocities (*Krause et al.*, 1970), up to 20 m/s (*Hsu et al.*, 2008), and are, therefore, from an engineering viewpoint, extremely dangerous for the stability of submarine structures placed at the seabed, such as oil pipelines, well heads, and telecommunication cables (*Meiburg et al.*, 2015).

Very few field measurements of turbidity currents are reported in the literature (e.g., *Xu et al.* (2004); *Andrieux et al.* (2013); *Azpiroz-Zabala et al.* (2017)), as these currents often occur

unexpectedly and may also destroy the measurement instruments located in their path. This explains why current understanding of turbidity currents is based mainly on laboratory experiments and numerical modelling.

Turbidity currents are not conservative flows, because they freely exchange the suspended sediments with the bed sediments through erosion and deposition. When the current is adequately swift, it picks up more sediments from the erodible bed than it deposits, increasing the suspended sediment concentration, and thus accelerating the flow, known as ignition or self-accelerating current (*Parker et al.*, 1986; *Sequeiros et al.*, 2018). In contrast, when the turbidity current decelerates, it starts releasing the suspended sediments at the bed, reducing the gravitational force, and thus decelerating until all the suspended material settles down.

Turbidity currents can be formed by numerous triggering mechanisms, such as submarine slope failures, storm-induced retrogressive failure of canyon walls (*Salaheldin et al.*, 2000), hyperpycnal flows (*Mulder et al.*, 2001), breaking internal waves, and breaching flow slides in fine-grained sands. Breaching-generated turbidity currents were unexplored until the publication of *Mastbergen and Van Den Berg* (2003), which revealed that breaching is an important triggering mechanism of turbidity currents. This fact was supported later by the work of *Eke et al.* (2011). The next section presents a detailed explanation of the physical processes of breaching flow slides, among which is the generation of turbidity currents.

2.3. GOVERNING PROCESSES OF BREACHING FLOW SLIDES

Breaching flow slides involve several physical processes, starting from the initiation of the failure up to the final deposition of the sediments. These processes should be well quantified and understood in order to model them accurately. Figure 2.4 shows a conceptual sketch of these processes, and that is followed by a description of each one in subsequent paragraphs.

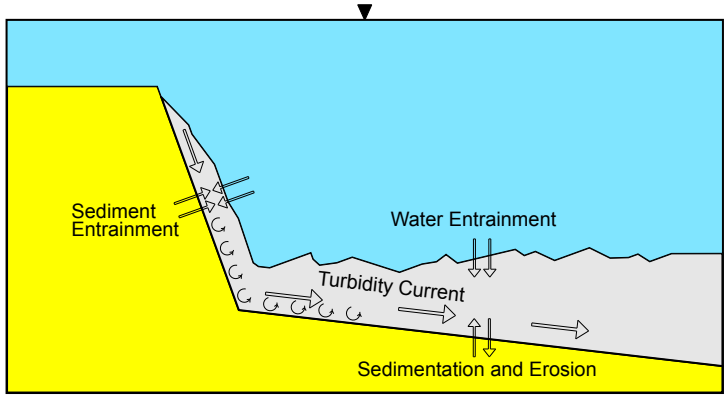

Figure 2.4: Conceptual sketch of the governing physics of a breaching process.

2.3.1. INITIAL BREACHING

When the underwater slope of a densely packed sand deposit becomes steeper than the internal friction angle, due to a certain triggering process, the slope becomes unstable. This is because the downslope component of gravity is greater than sand's shear resistance. In

this case, due to the dilative behavior of sand, the sand grains located at the sand–water interface drop grain by grain. This erosion process, breaching, stops once the slope reaches an angle milder than or near the internal friction angle.

Many different triggering mechanisms for flow slides in general are reported in the literature, such as earthquakes, excavations, slope erosion, rapid accumulation of deposits, gas charging, tides, and waves (*Locat and Lee*, 2002). Fluid motion in particular, plays a very important role in triggering flow slides, either by changing the geometry of the slope or the soil stresses or by destabilising the existing forces. According to *Jonkman and Schweckendiek* (2015), flow slides usually occur because the submerged slopes become gradually steeper by erosion processes due to river currents or tidal currents in estuaries. Figure 2.1a shows the 213 m long section of a dike that slid into the Mississippi River in 1983 at Darrow, in Louisiana. The flow slide took place shortly after a high water level had dropped, suggesting that rapid draw-down probably contributed to the failure (*Rogers*, 2012).

The current understanding of the triggering mechanisms of breaching flow slides remains very limited, showing the need for further investigations and research on this topic. It is possible that many breaching flow slides are triggered by scour at the toe of a submerged slope, which would lead to over-steepening of the submerged slope at the toe, resulting in a local instability. When the slope at the toe becomes steeper than the angle of repose, a retrogressive flow slide will take place starting from the toe (*Chu et al.*, 2004). A well-documented case of such a retrogressive flow slide in a relatively dense sand is the Mississippi riverbank (presented and described by *Torrey III* (1988); *Hadala and Torrey* (1989).

2.3.2. GENERATION OF A TURBIDITY CURRENT

The sand particles falling from the slope disperse as a sand-water mixture with a density greater than that of the ambient water, which provides the driving force for a turbidity current flowing downslope over the sand surface. This current generates turbulence, which keeps the sand particles in suspension while it also increases sand–water interfacial stresses. The frequent surficial slides significantly increase sand erosion and thus augment the turbidity current. Interestingly, the influence of the turbidity current determines whether the breaching process is stable or unstable, as it is related to the deposition of sediment at the slope toe, which can stabilize the slope. A complete theoretical description of this influence is not yet available, but an empirical relationship can be found in *Van Rhee* (2015) to predict whether the breaching process is stable or unstable.

The wall-normal velocity structure of turbidity currents shows two distinct regions: (1) an inner, near-bed region, and (2) an outer region (Figure 2.5). The former shows a positive velocity gradient, comparable to the typical turbulent boundary layer, while the latter shows a negative velocity gradient related to the entrainment of ambient water (*Simpson*, 1999). An experimental investigation conducted by *Kneller et al.* (1999) showed that the maximum velocity of the velocity profile occurs at about 0.2 times the entire height of the turbidity current. Turbulence kinetic energy reaches its maximum in the mixing shear layer and is close to zero at the location of the velocity maximum (*Kneller et al.*, 1999; *Gray et al.*, 2005). The sediment concentration decays in the wall-normal direction away from the bed, and seems to follow a power law distribution (*Middleton and Southard*, 1984).

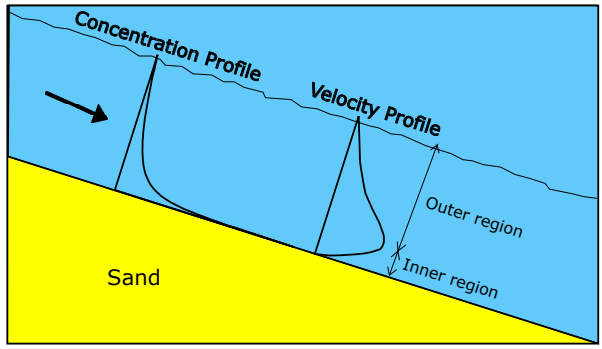

Figure 2.5: Typical velocity and concentration profiles of turbidity currents.

2.3.3. SEDIMENT ENTRAINMENT INTO TURBIDITY CURRENT

Turbidity currents have the potential to transport sediments in suspension over long distances and to erode additional sediments from the bed. They pick up sediment from the bed mainly through the shear stress they exert on the mobile bed (*Pratson et al.*, 2000). Sediment entrainment and the fate of the transported sediment are largely governed by turbulence. In the case that more sediments are picked up from bed into the turbidity current, the gravitational force boosts, which expedites the flow and enhances more sediment entrainment through a process termed ignition or self-acceleration (*Parker et al.*, 1986; *Sequeiros et al.*, 2009).

Breaching-generated turbidity currents exert additional shear stress on the breach face, leading to an increased erosion rate of the sand (*Mastbergen and Van Den Berg*, 2003). Steep slopes formed of fine-grained sediments are distinctive features in the breaching failure. *Yi and Imran* (2006) found out that steeper slopes composed of finer sediments have lower critical values of the velocity and sediment concentration causing ignition. This suggests that breaching-generated turbidity currents begin picking up sediments from the bed at earlier evolution stages than turbidity currents induced by other triggering mechanisms.

Very few studies have focused on the entrainment of sediments from the bed by turbidity currents (e.g., *Garcia and Parker* (1993)). The lower boundary layer of the turbidity current, the so-called near-bed region, has a relatively high concentration of sediment particles where the particle-fluid and particle-particle interactions promote the momentum and mass exchanges between the mixture flow and the sediment bed (*Zordan et al.*, 2017). The dynamics of this lower boundary layer are still poorly understood. This implies that the estimate of the sediment entrainment by breaching-generated turbidity currents is challenging, and the use of an empirical function is required, as discussed later in this chapter.

2.3.4. WATER ENTRAINMENT INTO TURBIDITY CURRENT

While the sand entrains into the turbidity current from the lower boundary, water entrains from the upper boundary of the current. Water entrainment is caused by the development of Kelvin–Helmholtz instabilities at the interface between the turbidity current and ambient water (*Ottolenghi and Adduce*, 2016). The dynamics of the current are affected by the amount of the entrained ambient water. This entrainment contributes to the dilution of the current. Additionally, it increases the overall thickness of the current and generates a shear stress along its upper surface, thereby reducing the net driving force and flow velocity (*Mulder*

et al., 1998).

Based on laboratory experimental studies on steady gravity currents, water entrainment was parametrised in terms of the densimetric Froude number (e.g., *Turner* (1986); *Parker et al.* (1987)) and in terms of both the Froude and Reynolds numbers (*Cenedese and Adduce*, 2010). The water entrainment coefficient e_w—defined as the entrainment velocity normalised by the mean downstream velocity—proposed by *Parker et al.* (1987), reads

$$e_w = \frac{0.00153}{0.0204 + \mathrm{Ri}}, \tag{2.1}$$

where Ri (-) is the bulk Richardson number defined as

$$\mathrm{Ri} \overset{\text{definition}}{=} \frac{\Delta g h C}{U^2}, \tag{2.2}$$

in which $\Delta = (\rho_s - \rho_w)/\rho_w$ (-) is the relative submerged density of the sediment, g (m/s^2) is the gravitational acceleration, h (m) is the current height, C (-) is the layer-averaged, volumetric suspended sediment concentration, and U (m/s) is the depth-averaged streamwise velocity.

Stagnaro and Pittaluga (2014) validated the empirical relation suggested by *Parker et al.* (1987) using their experimental values of the entrainment coefficient and found that it provides a good estimate.

2.3.5. SEDIMENTATION AND EROSION ON DOWNSTREAM SOIL BED

Once the turbidity current reaches the lowest point of the slope and begins flowing over the downstream bed, sediment exchange with the bed may take place through deposition and erosion processes. This means that the amount of suspended particles in the current changes with time. Whether erosion or deposition processes dominate the region at the bottom boundary is dependent on the magnitude of the shear stress at the lower boundary layer (*Cossu and Wells*, 2012). The balance of sediment exchange with the erodible bed determines whether the current is self-accelerating or decelerating, implying that any mechanism affecting the sediment exchange would affect the dynamics of the current (*Dutta et al.*, 2012). Complex topography may result when sediments are eroded, which may hinder or promote further sediment erosion. The dynamics of the sediment exchange are usually complicated and the underlying mechanisms responsible for the interaction between the bed surface and the turbidity current are not yet sufficiently understood (*Kyrousi et al.*, 2018). Therefore, empirical models for sediment entrainment and deposition are commonly used in numerical computations.

2.3.6. DEPOSITION OF SUSPENDED MATERIAL

When the breaching process ceases, the sediment supply driving the turbidity current diminishes. Accordingly, the turbidity current loses momentum and the suspended particles start settling down at the bed. When the current releases sand grains, it becomes more diluted and moves slower, which further diminishes the processes of sediment deposition and deceleration. The heaviest (coarsest) grains settle first and the lightest (finest) grains settle last, leading to deposits with an upward-fining character (*Pratson et al.*, 2000). The final post-failure angle of the breach face is usually near the maximum angle of repose.

2.3.7. CONCLUSION

In conclusion, the estimate of sediment erosion during breaching flow slides is not trivial, as many interacting parameters govern the erosion process, such as breach height, slope angle, soil characteristics, and the accompanied turbidity current. Yet, prediction of the erosion rate along the slope during breaching is required to assess the evolution of the sediment morphology and the turbidity current, which, owing to the previously described feed back mechanism, are coupled phenomena. This will determine whether or not the erosion or the associated turbidity current could potentially threaten the stability of nearby hydraulic structures. Furthermore, this can be used to estimate dredging production when a breaching failure is triggered deliberately as a means of sand mining. To this end, the next section addresses and discusses existing modelling approaches for breaching.

2.4. MODELLING SLOPE EROSION DURING BREACHING

2.4.1. SLOPE EROSION IN STAGNANT WATER

Breusers (1977) introduced the term "active wall velocity", which is defined as the horizontal travelling speed of a vertical submerged slope due to the breaching process. The expression of wall velocity can readily be derived by balancing the forces acting on a sand particle present on a slope (for a detailed derivation, the reader is referred to *Van der Schrieck* (2012)). For the sake of consistency, we present the resulting expression for the sand erosion velocity perpendicular to the breach face, v_w (m/s), which reads

$$v_w = -\frac{\sin(\phi-\alpha)}{\sin\phi}\,\frac{(1-n_0)}{\delta n}\,k_l\,\frac{\rho_s-\rho_w}{\rho_w}, \tag{2.3}$$

where ϕ is the internal friction angle, α is the slope angle, n_0 (-) is the *in situ* porosity of the sand, k_l (m/s) is the sand hydraulic conductivity at the loose state, ρ_s (kg/m^3) is the density of the particles, ρ_w (kg/m^3) is the density of water, and $\delta n = (n_l - n_0)/(1-n_l)$ is the relative change in porosity, in which n_l (-) is the maximum porosity of the sand. Equation 2.3 is valid when $\alpha > \phi$.

The erosion rate calculated using Equation (2.3) only takes into account the gravity-induced particle-by-particle failure resulting from the over-steepening of the slope. *Van Rhee and Bezuijen* (1998) found that this expression was invalid for the large-scale experiment they conducted, arguing that the reasons behind the mismatch are the sediment entrainment by the turbidity current and the frequent surficial slides. Results of small-scale experiments even indicate that the expression of wall velocity could not be suited for small breach heights, where weak turbidity current would be expected. Therefore, direct application of Equation (2.3) in practical cases is somewhat limited.

Figure 2.6 depicts the failure evolution in two small-scale breaching experiments, clearly showing that the erosion rate is non-uniform along the breach face, in contrast to the notion of a uniform wall velocity. The erosion rate increases in the downstream direction due to the acceleration of the turbidity current. Additionally, periodic surficial slides considerably boost sediment erosion, and thus provide the associated turbidity current with an additional capacity to erode the sand (*Beinssen and Mastbergen*, 2017).

In conclusion, breaching erosion closure models should incorporate sediment entrainment by the turbidity current and surficial slides to better predict the total sediment erosion rate along the breach face, and improve predictions of the failure evolution. The next section discusses some sediment entrainment functions relevant to breaching flow slides.

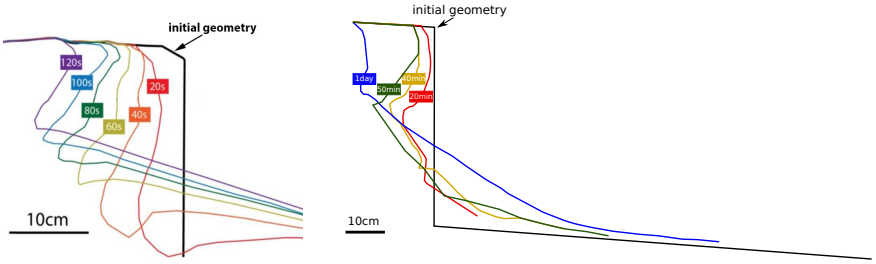

(**a**) (**b**)

Figure 2.6: Development of the breach face showing nonuniform erosion along the sand–water interface: (**a**) breach height = 30 cm, d_{50} =140 µm (adapted from *You* (2013)); (**b**) breach height = 70 cm, d_{50} =70 µm (adapted from *Eke* (2008)).

2.4.2. SEDIMENT ENTRAINMENT

A complete theoretical description of sediment entrainment by fluid motion is not yet available, due to the complexity of the erosion phenomena, and erosion by turbidity current is not an exception. As a consequence, sediment pick-up functions are usually developed by conducting experimental studies under special conditions in order to estimate the sediment fluxes (e.g., *Van Rijn* (1984); *Winterwerp et al.* (1992)). Most of the proposed pick-up functions in the literature consider a horizontal mobile bed over which a steady uniform flow propagates. The conditions of a breaching-generated turbidity current are different from these typical conditions. It is an unsteady, non-uniform, sediment-laden current, which travels over a sloping, dilative bed, which retards the erosion rate.

Generally speaking, the rate of sediment transport is dependent on the flow-induced bed shear stress, flow turbulence, the characteristics of the sediment particles, and in some conditions, on the bulk properties of sediments. Initiation of motion of non-cohesive sediment grains occurs once the Shields parameter θ exceeds a critical value θ_{cr} defined by

$$\theta_{cr} \overset{\text{definition}}{=} \frac{\tau_{cr}}{(\rho_s - \rho_w) g d_{50}}, \tag{2.4}$$

where τ_{cr} (Pa) is the critical bed shear stress and d_{50} (m) is the median grain size. Sediment grains begin to move along the bed by saltation, rolling, or shearing, but are not at that point entrained into the main flow. The pick-up process initiates once the sediment grains are entrained into the body of the flow, which is generally characterised by an empirical non-dimensional pickup rate ϕ_P defined as (*Einstein*, 1950),

$$\phi_p \overset{\text{definition}}{=} \frac{E}{\rho_s \sqrt{\Delta g d_{50}}}, \tag{2.5}$$

where $E = \rho_s v_e (1 - n_0)$ (kg/(s m^2)) is the sediment pick-up rate, in which v_e is the net erosion velocity perpendicular to the bed surface. Empirical relations are needed to express this non-dimensional pick-up rate in terms of the sediment and fluid properties, and the bed shear stress.

Several of these so-called "pick-up functions" can be found in the literature on the erosion of granular sediment. Most studies on sediment pick-up were conducted for horizontal and

mild stream-wise bed slopes in a steady uniform flow. Accordingly, the available erosion closure models for granular material at high flow velocities, where dilatancy is important, were only validated for a horizontal bed (e.g., *Van Rhee* (2010); *Bisschop* (2018)).

The focus of this chapter is on the most common pick-up functions and on those accounting for the dilatancy effect, which, for steady and uniform conditions, are attended to in the following subsection. The sediment entrainment in gravity currents is typically an unsteady phenomenon, which means that the inner density distribution and current kinematics are time varying, motivating a treatment in a separate subsection.

STEADY AND UNIFORM FLOWS

One of the most widely used sediment pick-up functions is that of *Van Rijn* (1984). Based on experiments with a very low sediment concentration, sand particles ranging from 0.13 to 1.5 mm and mean flow velocities ranging from 0.5 to 1 m/s, matching bed shear stress ranging between 0.5 and 2 Pa, *Van Rijn* (1984) derived the following pick-up function

$$\phi_p = 0.00033\, D_*^{0.3} \left(\frac{\theta - \theta_{cr}}{\theta_{cr}} \right)^{1.5}, \tag{2.6}$$

where D_* (-) is a dimensionless particle diameter defined by $D_* = d_{50} \sqrt[3]{\Delta g / \nu}$, in which ν (m^2/s) is the kinematic viscosity of water.

Winterwerp et al. (1992) conducted erosion experiments at a higher bed shear stress than *Van Rijn* (1984) ranging between 5 and 130 Pa. The investigation and analysis of their experimental data yielded an empirical pick-up function suited to this erosion regime where the erosion rate is reduced by the dilative behavior of the sand. The pick-up function reads

$$\phi_p = 0.012\, D_*^{0.3} \left(\theta^{0.5} - 1.3 \right). \tag{2.7}$$

It is worth mentioning that this function does not account explicitly for the effect of inflow of water into the pores. However, the effect is implicitly accounted for through the fitting procedure with the experimental data.

The experimental data of *Van Rijn* (1984) and *Winterwerp et al.* (1992) was used in *Mastbergen and Van Den Berg* (2003) to develop an empirical pick-up function including the effect of the dilative behavior of sand to describe the breaching process in fine-grained sands. The dilative behavior was taken into account by including the bulk properties of sand, such as permeability and porosity in their pick-up function

$$\phi_p = \frac{(1 - n_0)}{(g \Delta d_{50})^{0.25}} \sqrt{\frac{0.018 (\theta - \theta_{cr})^{1.5} D_*^{0.3} k_l \Delta (1 - n_l)}{n_l - n_0}}. \tag{2.8}$$

The experimental data presented in *Mastbergen and Van Den Berg* (2003) are partly in line with this pick-up rate.

The work of *Van Rhee and Talmon* (2010) showed that the pick-up function of *Van Rijn* (1984) overestimates the erosion in the case of high concentrations. They presented an empirical pick-up function based on experiments of highly concentrated flows with subcritical flow velocity. This function includes the effect of the near-bed volume concentration c_b (-) based on the argument that sediments are entrained by the turbulent eddies. If an eddy transports a certain volume of both sediment and water from the bed, the same volume of water should flow back to the bed due to continuity. If the sediment concentration is low,

this backflow will contain few particles, but if it is high, the backflow will transport more particles. Following this argument, a reduction factor $(1-n_0-c_b)/(1-n_0)$ was introduced to include the effect of the near-bed concentration. The resulting pick-up function presented by *Van Rhee and Talmon* (2010) reads

$$\phi_p = 0.0025\,(D_* - 2.4)^{0.3}\,\frac{1-n_0-c_b}{1-n_0}\,\theta. \tag{2.9}$$

However, no reference level above the bed was defined for the near-bed concentration, nor was a formula provided to estimate it. This empirical pick-up function can also be formulated in terms of the critical Shields parameter, as presented in *Van Rhee* (2015)

$$\phi_p = 0.000616\,\frac{\theta}{\theta_{cr}}\,\frac{1-n_0-c_b}{1-n_0}. \tag{2.10}$$

The work of *Van Rhee* (2010) and *Bisschop et al.* (2010) showed that using the pick-up function of *Van Rijn* (1984) results in overestimation of the erosion in the presence of dilatancy effect. The inward flow of water resulting from dilatancy amplifies the magnitude of the critical Shields parameter. *Van Rhee* (2010) adapted the conventional critical Shields parameter to include the influence of dilatancy considering the hydraulic gradient as an additional stabilising force acting on sand grains:

$$\theta'_{cr} = \theta_{cr}\left(\frac{\sin(\phi-\alpha)}{\sin\phi} + \frac{n_l-n_0}{1-n_l}\,\frac{1}{(1-n_0)\Delta}\,\frac{v_e}{k_l}\right), \tag{2.11}$$

where θ'_{cr} is the modified critical Shields parameter, and v_e is the erosion velocity perpendicular to the slope surface. Equation 2.11 also includes the effect of a sloping bed. For a horizontal bed, this expression reduces to

$$\theta'_{cr} = \theta_{cr}\left(1 + \frac{n_l-n_0}{1-n_l}\,\frac{1}{(1-n_0)\Delta}\,\frac{v_e}{k_l}\right). \tag{2.12}$$

Bisschop (2018) performed erosion experiments and validated the pick-up function developed by *Van Rhee* (2010) (Equation (2.12)). It was concluded that this pick-up function provides a good estimate of the pick-up flux for the finest sand types used in the experiments (d_{50} = 51 µm, 125 µm), while it overestimates the pick-up flux for the coarsest sand types used in the experiments (d_{50} = 262 µm, 561 µm).

TURBIDITY CURRENTS

Several relationships are proposed in the literature for the estimation of the associated entrainment rate of sediment by turbidity currents. In the field of turbidity currents, it is common to use a non-dimensional sediment entrainment coefficient E_s (-), see for instance *Garcia and Parker* (1991),

$$E_s \overset{\text{definition}}{=} \frac{E}{\rho_s w_s} \tag{2.13}$$

where w_s (m/s) is the particle settling velocity. In equilibrium suspensions, E_s equals the volumetric near-bed sediment concentration.

Akiyama and Fukushima (1985) utilised measurements for open-channel suspensions in rivers and flumes to develop the following relation for the sediment entrainment coefficient.

$$E_s = \begin{cases} 0.3, & Z > Z_m \\ 3 \cdot 10^{-12} Z^{10} (1 - Z_c/Z), & Z_c < Z < Z_m \\ 0 & Z < Z_c, \end{cases} \tag{2.14}$$

where $Z = (u_*/w_s) R_p^{0.5}$, in which $u_* = \sqrt{\tau_b/\rho_w}$ is the shear velocity, $R_p = \sqrt{\Delta g D^3}/\nu$ is the particle Reynolds number, and D is the particle diameter. The parameter $Z_c \approx 5.0$ (-) is a critical value for the onset of significant entrainment, and $Z_m \approx 13.2$ (-) represents a maximum value of Z beyond which E_s becomes constant with a value of approximately 0.3 (-).

Garcia and Parker (1991) also developed a sediment entrainment function for suspensions of uniform material in an open-channel flow. This function was compared in the work of *Garcia and Parker* (1993) with experimental results for turbidity currents. The estimated values by the empirical function followed the trend of the experimental data, but the scatter was large. Therefore, *Garcia and Parker* (1993) modified the function to take the form

$$E_s = \frac{A Z_*^5}{1 + A Z_*^5 / 0.3}, \tag{2.15}$$

where $A = 1.38 \cdot 10^{-7}$ (-) and $Z_* = (u_*/w_s) f(R_p)$, in which

$$f(R_p) = \begin{cases} R_p^{0.6}, & R_p > 3.5 \\ 0.586 R_p^{1.23} & 1 < R_p < 3. \end{cases} \tag{2.16}$$

Yi and Imran (2006) implemented different sediment entrainment relations in the four-equation model of *Parker et al.* (1986) (see *Garcia and Parker* (1993); *Akiyama and Fukushima* (1985); *Smith and McLean* (1977)). For the same input conditions, the computed results showed a different behavior of the turbidity current depending on the particular relation used for the sediment entrainment. In other words, a turbidity current predicted to be depositing when using a certain entrainment function could be ignited when using another one. This result explains the need for a better insight into the sediment transport mechanism by turbidity currents, as to derive advanced erosion closure models.

2.4.3. DISCUSSION

Based on the overview above, the following discussion points were raised:

- *Van Rhee* (2010) stated that the adapted critical Shields parameter can be used in any existing pick-up function as long as it includes the critical Shields parameter. Nevertheless, the existing pick-up functions are empirical and the effect of dilatancy could be already included (maybe to a certain extent) in the function. Having this effect in the empirical pick-up function and also in the critical Shields parameter may result in underestimation of the erosion rate.

- All the pick-up functions presented above require an estimate of the flow-induced shear stress. As a result, estimating sediment erosion is highly sensitive to the method by which the bed shear stress is computed.

- The existing relationships proposed to estimate the sediment entrainment by turbidity currents are mainly expressed in terms of the local shear stress. Nonetheless, boundary shear stress is just one of several impelling forces that result in sediment erosion (*Zordan et al.*, 2017). Other hydrodynamic quantities, such as turbulent stresses, and turbulent and mean velocities, also govern the mechanisms of sediment entrainment and transport (*Zordan et al.*, 2018).

- The existing sediment entrainment relations of turbidity currents (e.g., Eq. 2.14 and Eq. 2.15) were developed for a current propagating over a bed covered with loose sediment. Very little is known about the interaction of turbidity currents with densely-packed particles. In this case, dilatancy plays a major role in retarding the erosion process. Therefore, a sediment entrainment function for turbidity currents accounting for dilatancy effects is required to describe the breaching process properly.

In conclusion, the conventional sediment entertainment relations of turbidity currents (e.g., *Akiyama and Fukushima* (1985); *Garcia and Parker* (1993)) are inappropriate for breaching flow slides, as they do not account for the dilatation effect. Therefore, they will not be considered further in this chapter.

The next section outlines the existing numerical models coupling the breaching failure with the generated turbidity current, with an emphasis on the incorporated breaching erosion closure models and to what extent they deviate from each other.

2.5. NUMERICAL ASSESSMENT OF BREACHING-GENERATED TURBIDITY CURRENT

To study the implications of using different breaching erosion closure models for the hydrodynamics of the generated turbidity current, the existing erosion closure models are presented here, and followed by a comparison between the obtained numerical results. The existing breaching erosion closure models are the wall-velocity model of *Breusers* (1977), the model of *Mastbergen and Van Den Berg* (2003), and the model of *Van Rhee* (2015): Equations (2.3), (2.23), and (2.24) respectively. These were employed in combination with the three-equation model of *Parker et al.* (1986) and applied to a typical case of a breaching subaqueous slope. The three-equation model is a layer-averaged model based on the conservation of momentum, water mass, and suspended sediment in the turbidity current. More sophisticated numerical models can be used for computations of turbidity currents; however, a simple model was used here, as the purpose was to check to what extent the results of the model may deviate once different erosion closure models are adopted, rather than to obtain precise results.

2.5.1. THREE-EQUATION MODEL

The approximate, layer-averaged, three-equation model of *Parker et al.* (1986) is obtained by integrating the conservation equations for momentum, fluid mass, and sediment mass over height of the turbidity current, including the bed shear stress, water entrainment, and sediment erosion, respectively, as source terms. Using the layer thickness h (m), the layer-averaged velocity in the stream-wise direction U (m/s), and the layer-averaged volume suspended sediment concentration C (-) as independent variables, and assuming a steady

state, these equations read as follows,

$$\frac{\mathrm{d}(U^2 h)}{\mathrm{d}s} = -\frac{1}{2}\Delta g \frac{\mathrm{d}(Ch^2)}{\mathrm{d}s} + \Delta g Ch \sin\alpha - u_*^2, \tag{2.17}$$

$$\frac{\mathrm{d}(Uh)}{\mathrm{d}s} = e_w U, \tag{2.18}$$

$$\frac{\mathrm{d}(UCh)}{\mathrm{d}s} = v_e(1-n_0), \tag{2.19}$$

where s [m] is the stream-wise coordinate along the slope, Δ (-) is the relative submerged density of sediment, g (m/s^2) is the gravitational acceleration, α (-) is the bed slope angle, e_w (-) is the water entrainment coefficient, and v_e is the net erosion velocity perpendicular to the breach face resulting from the combined effects of erosion and sedimentation. The bed shear velocity u_* (m/s) is calculated by the relation $u_*^2 = C_f U^2$, where C_f (-) is a dimensionless bed friction coefficient.

After rearrangement, Equations (2.17)–(2.19) are conveniently formulated as "backwater" flow equations taking the form

$$\frac{\mathrm{d}h}{\mathrm{d}s} = \frac{-\mathrm{Ri}\sin\alpha + (2-\frac{1}{2}\mathrm{Ri})e_w + C_f + \frac{1}{2}\mathrm{Ri}\, v_e(1-n_0)/UC}{1-\mathrm{Ri}} \tag{2.20}$$

$$\frac{\mathrm{d}U}{\mathrm{d}s} = \frac{U}{h}\frac{\mathrm{Ri}\sin\alpha - (1+\frac{1}{2}\mathrm{Ri})e_w - C_f - \frac{1}{2}\mathrm{Ri}\, v_e(1-n_0)/UC}{1-\mathrm{Ri}} \tag{2.21}$$

$$\frac{\mathrm{d}(UCh)}{\mathrm{d}s} = v_e(1-n_0), \tag{2.22}$$

where Ri is the Richardson number, as defined in Equation (2.2).

After providing closure relations for e_w and v_e, the set of backwater equations is solved using a forward space marching procedure where the layer thickness, flow velocity, and sediment concentration at the top of the slope need to be specified as initial conditions; see also Section 2.5.3.

2.5.2. WATER ENTRAINMENT AND SEDIMENT EXCHANGE

For the dimensionless water entrainment coefficient e_w, the relation from *Parker et al.* (1987) is adopted; see Equation (2.1). For the erosion velocity v_e, existing breaching erosion closure models can be considered: the wall-velocity model of *Breusers* (1977), the model of *Mastbergen and Van Den Berg* (2003), and the model of *Van Rhee* (2015). These models are introduced below with a brief evaluation of their suitability to breaching flow slides.

BREUSERS (1977)

Following *Breusers* (1977), the erosion velocity v_e is taken as equal to the wall velocity v_w in Equation (2.3). Since the wall velocity only describes the initial stage of the breaching process, where sediment erosion is purely induced due to the oversteepening of the breach face, this erosion closure model does not account for the influence of the turbidity current. The wall velocity equation was incorporated into the numerical model of *Eke et al.* (2011) to estimate the erosion rate at the breach face.

Based on the work of *Parker et al.* (1986) and *Fukushima et al.* (1985), *Eke et al.* (2011) developed a three-equation, layer-averaged numerical model for breaching-generated turbidity currents. The governing equations of this model are the conservation of momentum and mass of the turbidity current. The results of this numerical model confirmed that breaching can be an important trigger of turbidity currents in submerged canyons. However, the model is subject to some limitations. The predicted slope profiles were not in line with the experimental data, as the model predicted much steeper slopes at the breach face than those observed in the experiments. The model also over-predicted the sediment deposition rates at the toe of the breach face (*Eke*, 2008). This could be due to the assumption that the erosion rate along the breach face is uniform and equal to the wall velocity.

MASTBERGEN AND VAN DEN BERG (2003)

Mastbergen and Van Den Berg (2003) developed a numerical model for breaching-generated turbidity currents based on one-dimensional, steady state, depth-averaged equations: momentum, water continuity, and sediment continuity. This model incorporated a formula modified from the work of *Winterwerp et al.* (1992) to estimate breaching erosion, Eq. (2.8). This formula can also be expressed in terms of the erosion rate v_e as follows:

$$v_e = \begin{cases} \dfrac{0.018(\theta-\theta_{cr})^{1.5} D_*^{0.3} k_l \sqrt{\Delta g d_{50}}}{(1-n_0)\frac{\sin(\phi-\alpha)}{\sin\phi}}, & v_e/v_w << 1 \\ \sqrt{\dfrac{0.018(\theta-\theta_{cr})^{1.5} D_*^{0.3} k_l \sqrt{\Delta^3 g d_{50}}}{\delta n}} & v_e/v_w >> 1, \end{cases} \tag{2.23}$$

where it has been assumed that the sediment deposition is negligible compared to the erosion.

The data presented by *Mastbergen and Van Den Berg* (2003) were too limited for proper validation by these authors. In addition, the formula does not account for the surficial slides. The authors also reported that there was insufficient data for an accurate calibration of all needed parameters for field conditions. However, the model revealed that the breaching mechanism can generate a strong turbidity current, which is capable of excavating a submarine canyon (*Mastbergen and Van Den Berg*, 2003).

VAN RHEE (2015)

Van Rhee (2015) developed a computational fluid dynamics, two-dimensional, drift-flux model based on the Reynolds averaged Navier–Stokes equations (RANS) to investigate the stability of the breaching process. This model is non-hydrostatic and incorporates a formula modified from the work of *Van Rhee* (2010) and *Van Rhee and Talmon* (2010) to estimate the erosion rate as

$$v_e = \frac{0.000616\sqrt{g\Delta d_{50}}\,(\theta/\theta'_{cr})\,(1-n_0-c_b)/(1-n_0) - w_s c_b \cos\alpha}{1-n_0-c_b}. \tag{2.24}$$

This relation accounts for the added effect of sedimentation, but does not account for the frequent surficial slides. *Van Rhee* (2019) validated the results of this numerical model against the temporal evolution of the breach face of two breaching experiments conducted by *Weij* (2020). However, validation of this model against measurements of breaching-generated turbidity currents is still missing.

2.5.3. COMPARISON OF RESULTS

To explore the deviations between the breaching erosion closure models, the breaching erosion rate was calculated for a typical situation, a 60-degree slope of fine sand, ignoring slope deformation and considering two different median grain diameters. The various parameters characterising the sand are listed in Table 2.1. The settling velocity of a single grain $w_{s,0}$ was computed using the formula of Budryck (*Miedema*, 2016), and the effect of the hindered settling was taken into account according to *Richardson and Zaki* (1954) to calculate the settling velocity w_s. The hydraulic conductivity k_l has been computed using the Kozeny–Carman equation (a semi-empirical expression).

Table 2.1: Sand parameters used in the calculations of the erosion rate.

d_{50}	n_0	n_l	ϕ	Δ	$w_{s,0}$	k_l
0.100 mm	0.39	0.48	30	1.65	6.7×10^{-3} m/s	3.6×10^{-4} m/s
0.135 mm	0.40	0.52	36	1.65	11.7×10^{-3} m/s	1.0×10^{-3} m/s

Two different situations are considered here: a uniform flow and a developing turbidity current, respectively. As the near-bed volume concentration c_b is not clearly defined in *Van Rhee and Talmon* (2010), a value of 0.2 was assumed in the calculations. Regarding the bed friction coefficient, studies have revealed that for turbidity currents, C_f varies between 0.002 and 0.05, with the lower values corresponding to observations in reservoirs and the higher values to laboratory experiments (*Parker et al.*, 1987). The estimates suggest that C_f is inversely proportional to the case scale. Therefore, for the uniform flow case, the calculations were performed using a value for C_f of 0.008, while for the case with a developing turbidity current it was chosen to be in the range of 0.015–0.025; see Table 2.2.

UNIFORM FLOW

Erosion rates resulting from the different erosion closure models are presented here, assuming a uniform flow, where the coupling between the sediment pick-up and the dynamics of the flow is ignored. A median grain diameter of 0.135 mm is used. Figure 2.7 shows the calculated erosion velocity v_e as a function of the flow velocity in the sediment layer.

As expected, the wall-velocity model renders the same erosion rate irrespective of the magnitude of flow velocities, since it is independent of the flow dynamics. The model of *Mastbergen and Van Den Berg* (2003) results in higher erosion rates than the model of *Van Rhee* (2015), and the difference is amplified at high flow velocities. This difference in the estimate of erosion rate may have critical implications for the numerical modelling of breaching-generated turbidity currents, since there is a direct feedback between the morphological changes of the breach face and the hydrodynamics of the turbidity current. These implications are investigated and described in the next section.

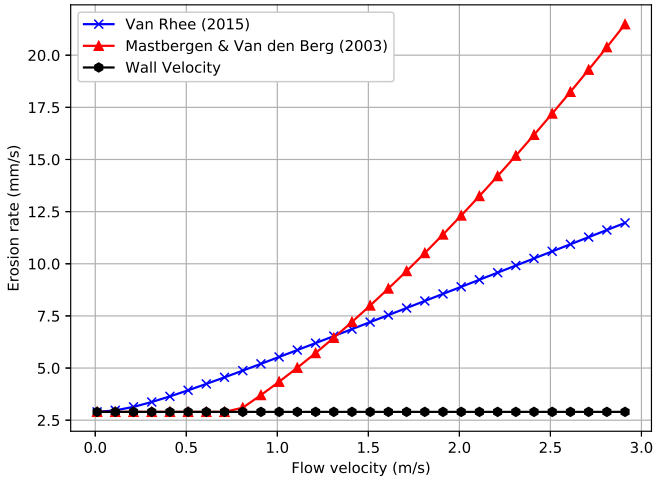

Figure 2.7: Comparison between breaching erosion formulations based on a uniform flow velocity; $d_{50} = 0.135$ mm (see Table 2.1).

Table 2.2: Values of v_e, U, C, h, and UCh computed 10 m downstream from the origin, using the three different erosion formulas.

Input Parameter \ Erosion Formula						(a) Wall Velocity, Equation (2.3)					(b) Mastbergen & Van Den Berg (2003), Equation (2.23)					(c) Van Rhee (2015), Equation (2.24)					Percentage of Difference between (b) & (c)				
Run	d_{50} (μm)	α	ϕ	C_f	n_l	h (m)	U (m/s)	C	v_e (mm/s)	UCh (m²/s)	h (m)	U (m/s)	C	v_e (mm/s)	UCh (m²/s)	h (m)	U (m/s)	C	v_e (mm/s)	UCh (m²/s)	Δh%	ΔU%	ΔC%	Δv_e%	ΔUCh%
1	135	60	36	0.015	0.52	0.21	1.66	0.05	2.9	0.017	0.24	2.83	0.17	33	0.114	0.24	2.37	0.11	13	0.061	2.9	17.4	46.9	86.4	60.3
2	135	60	36	0.02	0.52	0.20	1.63	0.05	2.9	0.017	0.24	3.07	0.22	46	0.159	0.23	2.43	0.12	15	0.070	0.8	23.1	56.1	100.8	77.4
3	135	60	36	0.025	0.52	0.18	1.61	0.06	2.9	0.017	0.23	3.26	0.27	60	0.203	0.22	2.47	0.14	17	0.078	4.1	27.4	62.5	111.7	89.6
4	100	60	30	0.02	0.48	0.19	1.65	0.06	3.2	0.019	0.25	3.30	0.25	60	0.205	0.23	2.42	0.12	15	0.068	5.9	30.9	69.7	120.6	100.0
5	100	60	30	0.02	0.48	0.20	1.83	0.07	4.6	0.028	0.25	3.31	0.25	61	0.208	0.24	2.48	0.13	16	0.075	4.3	28.6	66.1	116.3	93.8
6	100	50	30	0.02	0.48	0.17	1.60	0.07	3.1	0.019	0.22	3.17	0.27	57	0.194	0.21	2.348	0.13	15	0.067	5.3	29.9	67.7	118.4	97.0

DEVELOPING TURBIDITY CURRENT

The development of a turbidity current over a steep subaqueous slope of fine sand was considered, as depicted in Figure 2.8. Experience shows that a flow slide can occur spontaneously in fine sands if the slope steepness is at least 1:3 over a breach height of at least 5 m (*Mastbergen et al.*, 2015). Thus, a breach face of 10 m was considered in all the executed model runs, satisfying breach heights of more than 5 m. For the sake of simplicity, the deformation of the slope due to erosion was ignored by assuming that the slope angle remains 60 degrees along the entire breach face. Additionally, the turbidity current was considered to be purely erosive, since the slope simulated was very steep and eroded irrespective of the sediment transport capacity of the generated turbidity current.

The ordinary differential Equations (2.20)–(2.22) are discretised using first-order backward differences. The resulting system of discrete equations is solved using a simple forward space marching procedure using the layer thickness, flow velocity, and suspended sediment concentration at the crest of the breach face as initial conditions. The initial conditions have a local effect only—hardly affecting the overall steady state solution—as the turbidity current adjusts rapidly to the local conditions. The stream-wise coordinate is denoted as s, and the origin of this coordinate is the crest of the breach face. The different breaching erosion closure models were explored and compared for various input parameters as illustrated in Table 2.2. Besides, the values of U, C, h, v_e, and UCh (the volumetric suspended sediment transport rate per unit width) just before the toe of the slope are documented. The evolution of the turbidity current along the entire slope for Run 4 is shown in Figure 2.9. Unfortunately, there is no data in the literature for breaching-generated turbidity currents to compare with the results of our numerical simulations.

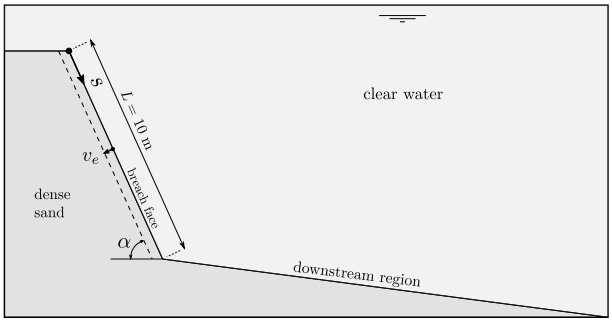

Figure 2.8: Sketch for the case considered in the numerical runs. v_e is the erosion velocity; α is the slope angle.

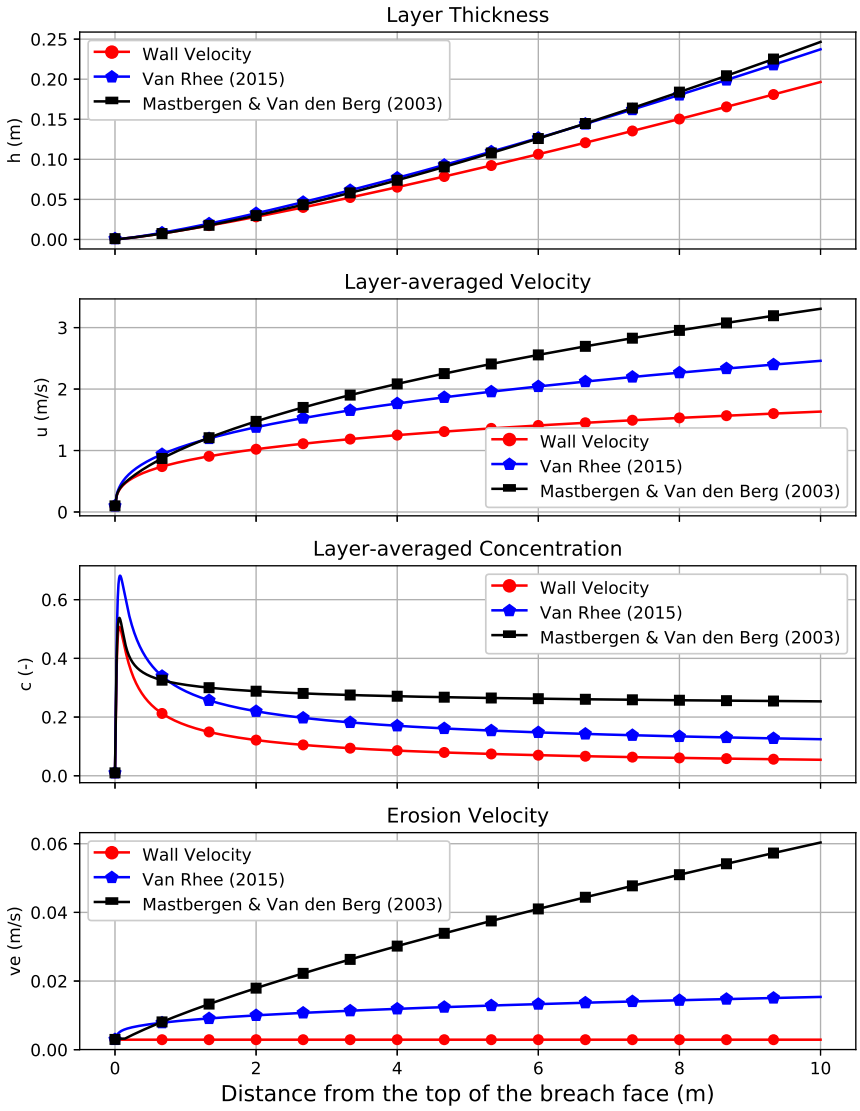

Figure 2.9: Comparison of the numerical steady-state results using different erosion formulas; $d_{50} = 0.100$ mm, $\alpha = 60^\circ$, $\phi = 30^\circ$, $C_f = 0.02$ (Run 4 from Table 2.2).

Figure 2.9 shows that the overall behavior of the turbidity current does not depend on the chosen erosion closure model; the layer thickness increases downstream, the layer-averaged concentration decreases downstream, and the turbidity current accelerates downstream. This acceleration is due to the sediment entrainment, which makes the current denser, and thus faster. This in turn increases the sediment erosion rate downstream the breach face. It is also obvious that using different erosion formulas renders very different erosion rates, and thus, different estimates of the hydrodynamic characteristics of the generated turbidity current. Using the expression of the wall velocity renders the weakest turbidity current with substantial deviation from the other two models. This makes sense, as this expression does not include the entrainment of sediment by the turbidity current, resulting in low uniform sediment supply along the slope, in contrast to the other two models. Accordingly, the focus was set on the deviation between *Mastbergen and Van Den Berg* (2003), Model(b), and *Van Rhee* (2015), Model(c). To have a better insight into the variation of results for these two models, the percentages of the differences between the results were computed. Considering Run 4 (see Table 2.2), for example, it is clear that the value of the sediment transport flux (UCh) yielded by Model(b) is more than two times of that yielded by Model(c) with deviations of 31% and 70% in the velocity and concentration respectively.

2.5.4. DISCUSSION

Comparison of numerical results shows that the sediment entrainment relation has important implications for the modelling of turbidity currents, since the model can give different predictions based on which relation is utilised.

In particular, model results at the toe of the slope are important, since they are the main information for determining the upstream boundary conditions for the turbidity current propagating over the bed of the downstream region. This could result in a different behavior of the turbidity current over the downstream bed concerning erosion and sedimentation. Another crucial implication is that different predictions of the hydrodynamics of the turbidity current may lead to different predictions of the stability of the breaching process, as the turbidity current is the main parameter influencing breaching stability.

The results also reveal that numerical results are more sensitive to the value of C_f when the erosion formula of *Mastbergen and Van Den Berg* (2003) is used.

2.6. CONCLUSIONS AND OUTLOOK

In the course of this methodical review and analysis of the state-of-the-art knowledge and current modelling approaches, the most relevant physical processes and models to breaching flow slides have been discussed. This resulted in the identification of some knowledge gaps and weaknesses of the current models.

It is important to further investigate the breaching failure mechanism, as recent studies have revealed that breaching, rather than liquefaction, is the main driver of the observed flow slides in nature. It is quite difficult to conduct controlled in situ experiments on breaching and the associated turbidity currents. This emphasises the importance of laboratory studies and numerical modelling for gaining a better understanding of the nature of breaching flow slides and their associated sediment transport.

Turbidity currents at laboratory scale are usually depositional, but breaching-generated turbidity currents are primarily erosive as they propagate over the failing slope, due to the over-steepening of the slope. It was shown that using the same input parameters and

computational grid in a numerical model while employing different sediment entrainment relationships yields very different sediment erosion rates and hydrodynamics of turbidity currents. This would result in different evolution of the breach face. Therefore, the development of advanced erosion closure models accounting for sediment entrainment by the turbidity current and frequent surficial slides will be instrumental to improving the accuracy of numerical computations. To that end, it is helpful to conduct breaching experiments, which include detailed measurements of flow and turbulence, particularly measurements of sediment concentration, as it is the critical parameter controlling turbidity currents. Such measurements are quite scarce in the literature. Therefore, laboratory breaching experiments have been conducted in the water lab of Delft University of Technology (see Chapter 3).

On the modelling part, there are also significant challenges which should be addressed. A deeper understanding of the triggering mechanisms by which a breaching flow slide takes place is required to develop convenient initial and boundary conditions. Given that soil is rarely homogeneous in reality, it would be beneficial to couple the simulation of the turbidity current to an advanced soil model that accounts for the spatial variation in soil characteristics, such as packing density, permeability, particle size, and porosity. Pursuing the above goals requires the incorporation of complementary research methodologies from the fields of soil and fluid mechanics.

3

LARGE-SCALE EXPERIMENTS

Breaching flow slides are accompanied by the generation of turbidity currents. Measurements of these currents are critical for understanding the interaction between the turbidity current and the slope surface, as well as for the validation of numerical models. However, there are insufficient data available detailing the velocity distribution or sediment concentration in these currents. This chapter presents experimental results of unique large-scale physical model experiments on breaching flow slides conducted at the water lab of Delft University of Technology, The Netherlands. The model tests were carried out in a tank with a subaqueous sandy slope steeper than the internal friction angle for that sand. We performed a series of novel experiments in which various non-vertical initial slope angles were tested, providing the first quantitative data for such initial conditions. Measurements of flow thickness, velocities, and sediment concentrations are obtained, providing the spatial and temporal evolution of the turbidity currents and the resulting underwater slope morphology. The experimental results reveal that the breaching-generated turbidity currents are self-accelerating, and that they dominate the problem of breaching flow slides. We evaluated the theoretical expression for the erosion velocity in the case of pure breaching - where the turbidity current has no influence on the erosion - and it overestimated the observed erosion. The analysis of the failure evolution showed that the sand erosion rate increases due to the acceleration of the turbidity currents downslope, until a certain threshold, leading to the steepening of the breach face and thus the occurrence of surficial slides.

This chapter has been published as Alhaddad, S., Labeur, R. J., and Uijttewaal, W. (2020). Large-scale Experiments on Breaching Flow Slides and the Associated Turbidity Current. Journal of Geophysical Research: Earth Surface. https://doi.org/10.1029/2020JF005582

3.1. INTRODUCTION

A flow slide occurs when a large, subaqueous soil mass is destabilized and accelerates down a slope, then eventually redeposits, creating a milder slope. This failure mechanism poses severe risk for subaqueous structures and is able to undermine an entire hydraulic structure, resulting in significant damage. Breaching is a specific type of flow slide, which is accompanied by the generation of turbidity currents. This type of current, from an engineering point of view, is very dangerous for the stability of structures placed at the seabed, such as oil pipelines, well heads and cables. A breaching flow slide can thus pose dangers, directly and indirectly, to nearby or remote underwater infrastructure.

Many flow slide events, occurring in different places around the world, are reported in the literature (e.g., *Koppejan et al.*, 1948; *Kramer*, 1988; *Silvis and Groot*, 1995; *Mastbergen et al.*, 2019). The Netherlands, in particular, has a long history of such events, where post-event observations were made. The absence of observations of the temporal development of the failure is due to the fact that flow slides usually remain entirely underwater and their timing is unpredictable. Sometimes, if the flow slide does not terminate underwater, it propagates to shorelines and riverbanks, where it may cause severe damages. A flow slide is inherently a complex failure mechanism, as it involves geotechnical aspects within the soil body, and also hydraulic aspects within the fluid transporting the failing soil. Nevertheless, a thorough understanding of flow slides is important for enhancing the safety of flood defences and designing well-suited mitigation measures.

The term 'breaching' specifically refers to the gradual, retrogressive failure of a steep subaqueous slope, greater than the internal friction angle. This type of failure often occurs in densely-packed sand, due to its dilative behavior under shear forces. Dilatancy results in a negative pore pressure, which temporarily stabilizes the sand. Due to the pressure difference, the ambient water is forced to flow into the pores, dissipating the negative pressure, and thus, destabilizing the grains located at the sand-water interface. These grains peel off one by one and get suspended in water. This failure mechanism has been used since the 1970s as a means of sand mining by the Dutch dredging industry. To estimate the dredging production, *Breusers* (1977) introduced the term 'wall velocity', which refers to the horizontal propagation speed of a vertical submerged slope due to the breaching process. For the sake of consistency in this dissertation, we provide the resulting expression for the sand erosion velocity perpendicular to the breach face (see Chapter 2), v_w [m/s], which reads

$$v_w = -\frac{\sin(\phi-\alpha)}{\sin\phi}\,\frac{(1-n_0)}{\delta n}\,k_l\,\frac{\rho_s-\rho_w}{\rho_w}, \tag{3.1}$$

where ϕ is the internal friction angle, α is the slope angle, n_0 [-] is the *in situ* porosity of the sand, k_l [m/s] is the sand hydraulic conductivity at the loose state, ρ_s [kg/m^3] is the density of the particles, ρ_w [kg/m^3] is the density of water, and $\delta n = (n_l - n_0)/(1-n_l)$ is the relative change in porosity, in which n_l [-] is the maximum porosity of the sand.

The suspension of sediments increases the fluid density, which in turn generates a turbulent flow referred to as a breaching-generated turbidity current. This current flows over and interacts with the slope surface. Consequently, it may increase the erosion of the sand surface, picking up more sediment into suspension, thereby increasing speed and erosion potential (*Alhaddad et al.*, 2019). Quantitative data of the erosion caused by this current is still missing, leaving the question open whether it could play a considerable role in the problem of breaching flow slides. In this respect, it is worth mentioning that Equation

3.1 does not account for the sediment entrainment by turbidity currents; therefore, a few attempts were made to develop it into an erosion closure model accounting for sediment entrainment by turbidity currents (*Mastbergen and Van Den Berg*, 2003; *Van Rhee*, 2015). However, as shown in Chapter 2, these erosion closure models show considerable differences in outcome for typical breaching conditions (*Alhaddad et al.*, 2020a), demonstrating the need for validation data.

It is quite difficult to carry out controlled in-situ measurements of breaching and the associated turbidity currents, as the occurrence of these events is unpredictable in field situations and the turbidity currents may destroy the measuring instruments. This highlights the importance of laboratory studies for gaining better insights into the nature of breaching flow slides and their associated sediment transport. Very few laboratory experiments on breaching are reported in the literature (e.g., *Van Rhee and Bezuijen*, 1998; *Eke et al.*, 2009; *You et al.*, 2012). Moreover, these experiments have not sought to investigate the flow development along the breach face, instead focusing on investigating the failure evolution or turbidity currents traveling down the slope toe. Although breaching is theoretically a grain-by-grain failure, a periodic collapse of coherent sand wedges, referred to as surficial slide, was observed in some of these experiments. A complete theoretical description of these surficial slides is not yet available.

The current knowledge about the structure of sediment concentration or fluid velocity of breaching-generated turbidity currents is very limited. The complications associated with measuring such currents, even in lab experiments, have resulted in there being very limited direct measurements of fluid velocity and concentration. There are several reasons why it is difficult to obtain such measurements. The development of breaching-generated turbidity currents is typically a non-uniform unsteady phenomenon, meaning that current kinematics and inner density distribution are space and time varying. Investigating the development of the current along the breach face demands a sufficient traveling distance and hence sufficient experimental scale. Besides, the generated turbidity currents are very thin (few centimeters), requiring high-resolution measurements to visualize their structure. Another complication is that the sediment bed (or 'breach face') moves continuously backward as a result of sediment erosion. Crucially, the high sediment concentration within the current increases the difficulty level and limits the choices of possible measuring techniques.

This chapter presents results of breaching experiments having sufficiently large scale to warrant the occurrence of a self-accelerating turbidity current during the breaching process. The experiments are carried out in a 2 m high breaching tank in which the initial slope angle of the sand can be varied. Ultrasonic velocity profilers supplied high-resolution, one-dimensional visualisation of flow fields, thereby yielding the first quantitative visualisation of velocity profiles of a breaching-generated turbidity current. In addition, wall-normal concentration profiles are provided. Furthermore, an analysis of the surficial slides is carried out, attempting to understand the reason behind their occurrence.

3.2. EXPERIMENTS

The experiments were set up specifically to investigate breaching flow slides and the associated turbidity currents. This section describes the design considerations and construction of the experimental tank, the instrumentation, the experimental procedures, and the processing of the results.

3.2.1. EXPERIMENTAL SETUP

The experimental setup consists of several components: a breaching tank, removable confining wall, false floor, damping tank, and sedimentation tank. As triggering mechanisms of breaching flow slides are still poorly understood (*Alhaddad et al.*, 2020a), the experiments were performed for over-steepened, unstable slopes that initially fail due to the gravitational force. To this end, the slope of the confining wall can be adjusted in order to investigate a range of initial slope angles between 50° and 80°. The dimensions of the sand deposit were chosen such that the length of the breach face is similar in each of these experiments, ranging between 150 ± 10 cm. Fig. 3.1 shows a schematic overview of the experimental setup; a description of each of its components is provided in the subsequent paragraphs.

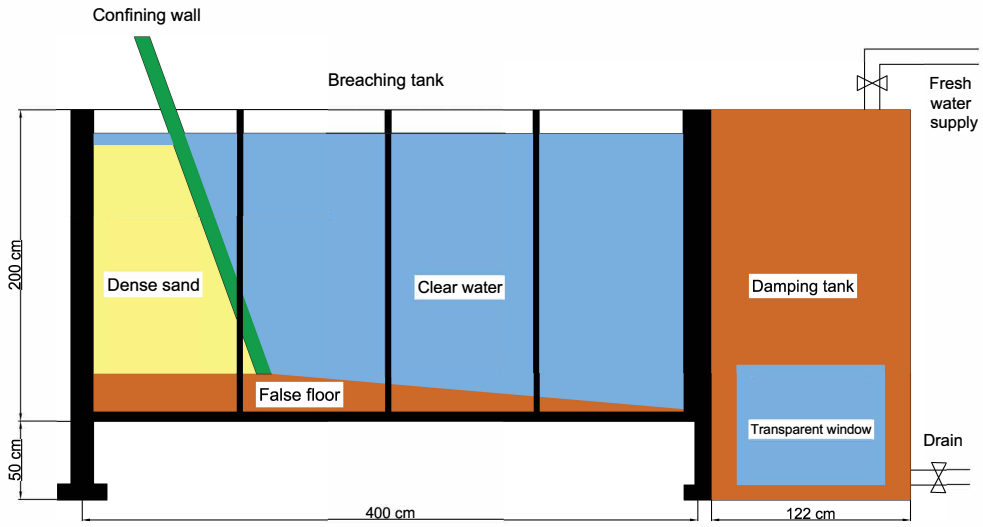

Figure 3.1: Side view of the experimental setup illustrating the components; the sedimentation tank is not shown in this figure.

BREACHING TANK

The breaching process takes place inside this tank. Multiple factors were taken into account to determine the dimensions of this tank. One of these factors was to have a considerable contribution of the turbidity current to the erosion process along the soil-water interface. This contribution will be clearer once higher velocities of the turbidity current develop along the slope, causing high flow-induced shear stresses. For a given breach height, the layer-averaged downslope velocity of the turbidity current and the associated erosion rates can be estimated using the approximate layer-averaged 3-equation model of *Parker et al.* (1986) presented in Chapter 2 (see also *Alhaddad et al.* (2020a)). This was used to determine the required initial breach height, and thus the breaching tank height.

The resulting breaching tank is 4 m long, 0.22 m wide and 2 m high. It was made sufficiently long to allow for observation of the evolution of the breaching failure, both upstream as the breach face progressively erodes and downstream as the ensuing downstream turbidity current develops. The tank width was chosen to be similar to that of the flume at Utrecht

University, The Netherlands, where geotechnical aspects of breaching flow slides were simultaneously being investigated (see *Silva* (2020)). This would result in having comparable and complementary experiments. The back and front sides of our tank are made of different materials. The front side is made of glass to facilitate failure tracking and flow visualization. The back side is made of a removable steel plate making the tank accessible for maintenance purposes and to replace the false floor when required.

The false floor consists of two parts: a horizontal part on which the sand deposit is placed and a sloping part covering the distance from the toe of the sand deposit to the downstream end of the breaching tank. The false floor can be set to a specified slope, as to increase the sediment transport capacity of the turbidity current versus the existing flat bottom. Consequently, a smaller amount of sand will accumulate at the toe of the initial sand deposit, maintaining adequate breach heights during the experiments.

CONFINING WALL

A confining wall was needed to prevent the failure of sand during the construction process of the sand deposit and to shape the targeted slope angle. The used confining wall is a sliding mesh gate covered with geotextile (tissue opening size 0.04 mm), which allows water to pass through it while holding sediments in place. This enables water to escape from the pores through the wall to the ambient water during the compaction process of sand, creating a fully-saturated densely-packed deposit. A distinctive feature of this wall is that its inclination is adjustable, thereby allowing various initial slope angles.

The confining wall (230 cm long) is surrounded by a flexible rubber hose to prevent the soil particles from passing along the sides of the confining wall to the ambient water. The rubber hose was inflated with air before constructing the sand deposit to close all the gaps between the confining wall and the back and front sides of the breaching tank. The air was quickly released just before pulling out the confining wall to facilitate the pulling mechanism.

The confining wall is manually operated by a hand crank (Fig. 3.2a). A special support system was used to hold the confining wall in place during the construction of the sand deposit and during the pulling procedure. It also allows for horizontal adjustment of the wall along the breaching tank, making it possible to change the initial width of the sand deposit. A protractor fixed on the support system is used to adjust the inclination of the wall to the targeted slope angle. A different custom-built wall end, which can be attached to the bottom end of the confining wall, was used for each experiment, as to avoid the escape of sediment particles at the slope toe (Fig. 3.2b).

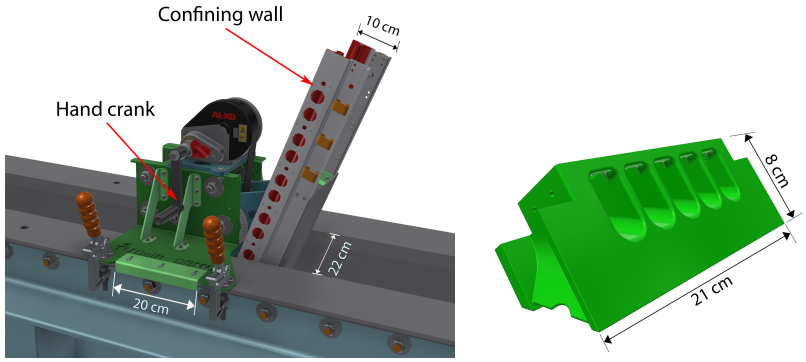

(a) Wall support system

(b) Bottom wall end

Figure 3.2: The confining wall: (**a**) sketch of the support system placed at the top of the breaching tank; (**b**) the bottom wall end.

DAMPING AND SEDIMENTATION TANKS

The downstream end of the breaching tank is left open and connected to a deeper damping tank (122 cm long, 114 cm wide and 250 cm high) to allow the turbidity current to flow freely from the breaching tank into the damping tank. The level of the soil-water mixture in the damping tank should be kept below the bottom of the breaching tank to avoid reflection of the turbidity current from the damping tank back upstream. For this purpose, the turbidity current is drained from the bottom of the damping tank at the downstream end, while a flow of clear water is supplied at the top of the damping tank to maintain a constant ambient water depth throughout the experiment. The discharge of the inflowing water and outflowing turbidity current are monitored by electromagnetic flowmeters. Additionally, two overflow pipes are located at the top of the damping tank and used to make sure there is no water overspill.

The sedimentation tank (250 cm × 125 cm × 125 cm, adjacent to the damping tank, not shown in Fig. 3.1) is used for collecting the sand-water mixture pumped out from the damping tank. It also allows the sand particles to settle down so the sand can be reused for the next experiments.

3.2.2. CHARACTERIZATION OF SAND DEPOSIT

As the problem of breaching is associated with fine sediments, a fine sand (Sibelco BR37) of d_{50} equal to 0.135 mm was used in the experiments. The analysis of the grain size distribution conducted within the Dutch–Flemish Western Scheldt monitoring program (*Mastbergen and Schrijvershof*, 2016) suggests that breaching mainly occurs in uniformly-graded sediment, motivating our choice of a uniformly-graded sand. Fig. 3.3 shows the cumulative grain size distribution of the sand used. The coefficients of uniformity, $C_u = d_{60}/d_{10}$ and curvature $C_c = d_{30}^2/(d_{60}\, d_{10})$, are 1.31 and 1, respectively, indicating that the sand is uniformly graded. In these relations, d_{10}, d_{30} and d_{60} are particle sizes for which 10%, 30% and 60% of the weight of the grains, respectively, is finer. As the range of the grain size distribution is narrow (Fig. 3.3), the impact of segregation of coarser and finer grains, when pouring the sand into the breaching tank, is minimized.

The breaching process is largely determined by the permeability, the internal friction angle, and the initial and loose-bed porosity of the sand (see Eq. 3.1). In order to define the hydraulic conductivity at maximum porosity, k_l, the hydraulic conductivity was measured for different porosities (Fig. 3.4) through a series of constant-head permeability tests (ASTM-method D2434). The internal friction angle ϕ was determined by the direct shear test (*Silva*, 2020). The initial porosity, $n_0 = 0.4$, and loose bed porosity, $n_l = 0.51$, were determined from sand compaction tests. The properties of the used sand are summarized in Table 3.1.

Table 3.1: The properties of the sand used in the experiments.

d_{10}	d_{30}	d_{50}	d_{60}	n_0	n_l	ϕ	k_l
0.107 mm	0.123 mm	0.135 mm	0.140 mm	0.40	0.51	36°	0.0307 cm/s

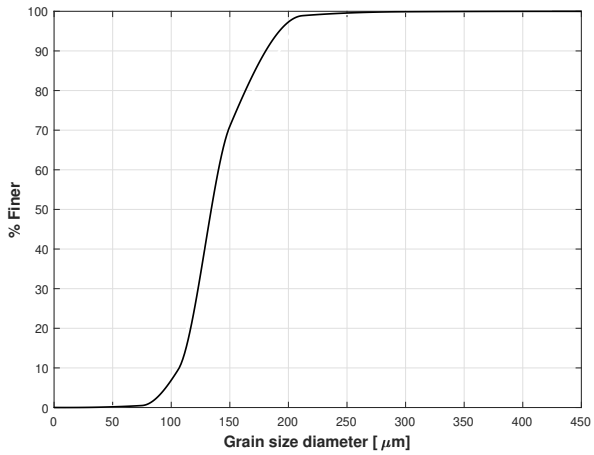

Figure 3.3: Cumulative grain size distribution of the sand used in the experiments, as provided by Sibelco, France.

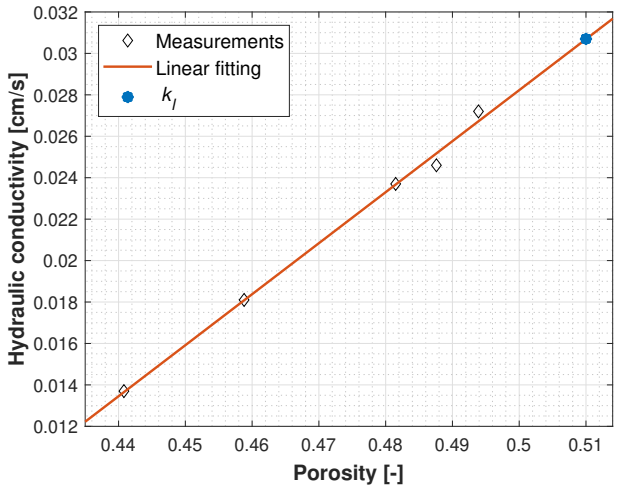

Figure 3.4: Sand hydraulic conductivity as a function of sand porosity; the hydraulic conductivity at maximum porosity k_l is determined from the linear fitting.

3.2.3. TEST PROCEDURE

Each breaching experiment was prepared following the next sequence of steps:

- The false floor is placed at the bottom of the breaching tank.
- The wall end corresponding to the selected slope is connected to the confining wall, in order to adjust the angle of the latter, after which the wall rubber is inflated with air.
- The tanks are half filled with clean water.
- A layer of sand (approximately 20 cm thick) is placed into the breaching tank and compacted by a vibrator needle until it cannot be further compacted (this ensures that the sand will be homogeneous and have the maximum relative density - minimum porosity).
- The previous step is repeated until the level of the top of sand deposit is few centimetres below the water level.
- Additional clean water is supplied into the tanks.
- The previous two steps are repeated until reaching the targeted breach height.
- The crest of the sand deposit is tapped by a wooden piece to make it horizontal.

After deploying the measurement instruments and testing their signals (see Sec. 3.3), the experiment proceeds as follows:

- The wall rubber is deflated and the confining wall is quickly pulled out by rotating the hand crank, which takes about 6 seconds when operating the manual system at maximum rate; the experiment starts as soon as the confining wall is completely released.

- The turbidity current is drained from the bottom of the damping tank at the downstream end by a sand-water mixture pump while, simultaneously, a flow of clear water is returned at the top of the damping tank to guarantee a constant level of water in the tanks.
- The experiment stops if all the sediments from the sand deposit have run out, leaving a fresh deposit on the entire bottom of the tank.

Right after the removal of the confining wall, the underwater sand deposit starts to fail as particles peel off one by one, creating a shower of sand which drags the ambient water along to generate a downward turbidity current. Velocity and concentration profiles are measured at various transects normal to the breach face, for different stages of the breaching failure, following the development of the breach face and the associated turbidity current in time.

Table 3.2 summarises the initial conditions of the experiments conducted within this study.

Table 3.2: A summary of the initial conditions of the experiments.

Test	Slope angle [°]	Breach face length [cm]	False floor angle [°]	Downstream distance* [cm]
1	80	144	6	284
2	70	156	6	284
3	65	140	9	245
4	60	156	9	245
5	50	160	13	214

*The downstream distance is the length of the slope down the toe of the breach face.

3.3. DATA ACQUISITION AND PROCESSING

3.3.1. INSTRUMENTATION

The underwater instruments are placed on a measuring post that can move over the breaching tank in the same direction as the breach face. The inclination of the lever (Fig. 3.5) can be adjusted - using a rope connected to a friction cleat at the top part of the measuring post - in order to keep the instruments aligned with the breach slope as it evolves during the experiment. The measuring post was equipped with various instruments described in the following subsections.

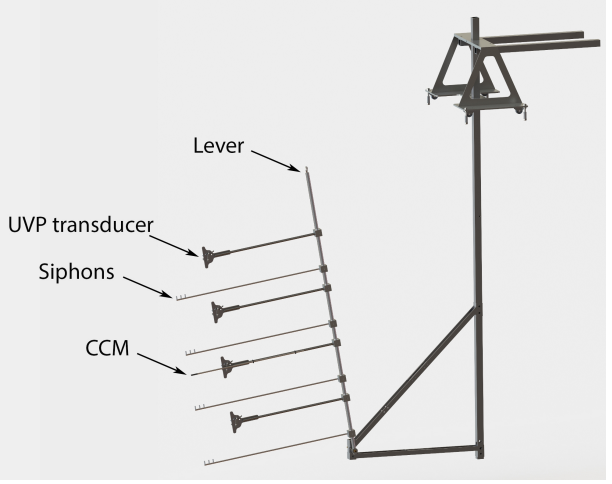

Figure 3.5: The measuring post with the instruments connected to the lever: four rakes of siphons, four ultrasonic velocity profiler (UVP) transducers, and one conductivity concentration meter (CCM).

RAKES OF SIPHONS

Four rakes of three siphons each were used to obtain suspended sediment samples at different heights from the breach face in order to obtain the wall-normal density distributions. The sampling process was controlled manually for all siphons in all sets. All siphons were activated before the start of the experiments, and were kept flowing constantly. The siphons were fabricated from tubes of 8 mm external diameter and 5 mm internal diameter, sufficiently large to allow for the flow of high-concentration samples. The distance between the center of the first siphon and the breach face was not constant and the center-to-center distance between siphons was fitted to 2 cm.

ULTRASONIC VELOCITY PROFILERS (UVP)

Simultaneous measurements of downslope flow velocity and acoustic backscatter were obtained using two units of Met-Flow ultrasonic velocity profilers (UVP-Duo). The UVP is a monostatic system, where the acoustic transducer works both as emitter and as receiver of the sound waves, to measure the velocity of particles and backscatter along an axis perpendicular to the transducer face. The reader is referred to *Lemmin and Rolland* (1997) for further details on the capabilities and limitations of UVP.

Each UVP-Duo unit was equipped with two transducers, held in position by a custom-built holding house (Fig. 3.6), where one transducer emits bursts of ultrasonic signals at a frequency of either 1, 2 or 4 MHz. Initial experiments (70° and 80° initial slopes) revealed that high-resolution 4 MHz signals could not capture any velocities in the near-bed region, due to the high particle concentration, which attenuates the acoustic signal. It was, therefore, decided to use 1 and 2 MHz transducers in the rest of experiments, compromising spatial resolution. Two 2 MHz transducers were used at the upper part and two 1 MHz transducers at the lower part of the breach face. This gives a total of four transducers. The system is not able to obtain velocity profiles from every transducer simultaneously, but can only obtain in sequence from each transducer. Consequently, two transducers in total were simultaneously recording. The ultrasonic signals involve 128 channels, directed along the transducer axis.

The corresponding signals are reflected at the sand particles present in each channel. The transducer then records the frequency of the reflected signals. Following Doppler theory, the shift in emitted or received frequency determines the fluid velocity for every channel, which together produce a velocity profile.

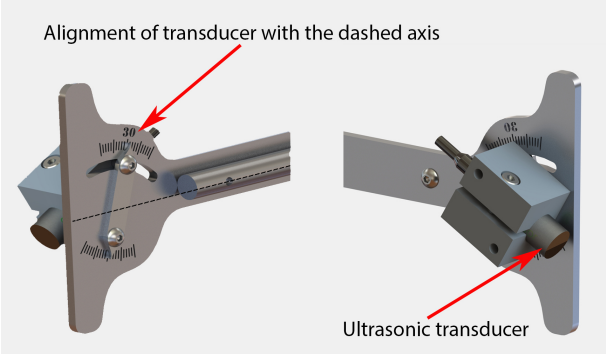

Figure 3.6: 3D computer model of the holding house of the UVP transducers; in all experiments the transducer angle was set to 30° with the dashed axis, the latter corresponding to the normal of the breach face.

CONDUCTIVITY-TYPE CONCENTRATION METER (CCM)

The conductivity-type concentration meter (CCM) system is an instrument used to measure the concentration of sand-water suspensions at a single point. The measuring concept is based on the conductivity change of a sand-water mixture due to the change of the amount of suspended sediment present in the measuring volume. The conductivity of the sand-water mixture is proportional to the density of the mixture. Conductivity-based instruments have been found most reliable for high sediment concentrations. The CCM can measure sediment concentrations up to 50% by volume (*Deltares*, 2016). The volumetric sediment concentration C_v [-] can be measured using the following relation:

$$C_v = F_{\text{cal}} \left(1 - \frac{V_0}{V_m}\right) \tag{3.2}$$

where V_0 is the reference voltage for clear water, V_m is the measured voltage and F_{cal} is the calibration factor. The voltages for clear water and for different sand-water mixtures, using the same type of sand as used in the experiments, were used to derive the value of F_{cal}.

VIDEO CAMERAS

Besides the measuring post, two digital video cameras (25 frames per second) were employed to record the entire experimental run. The view of the first camera was set on the sand deposit to measure the erosion rate along the breach face and to define the position of siphons and the angle of the UVP transducers with the vertical. On the other hand, the view of the second camera was set on the entire breaching tank to investigate the overall failure evolution. A checkerboard pattern, and horizontal and vertical rulers were placed on the front side of the tank to be used as a reference frame for correcting the extrinsic distortion of the camera images, see Fig. 3.7.

3.3.2. DATA ACQUISITION

As soon as the confining wall is completely released, the measuring post is moved towards the breach face to collect data, see Fig. 3.7. A plume of sand particles would be generated very near the slope surface by the quick release of the confining wall. The measurements start right after the settlement of the first plume particles, which usually takes a few seconds. Focus was set on the initial stage of the failure, when the slope angle was the same everywhere along the breach face.

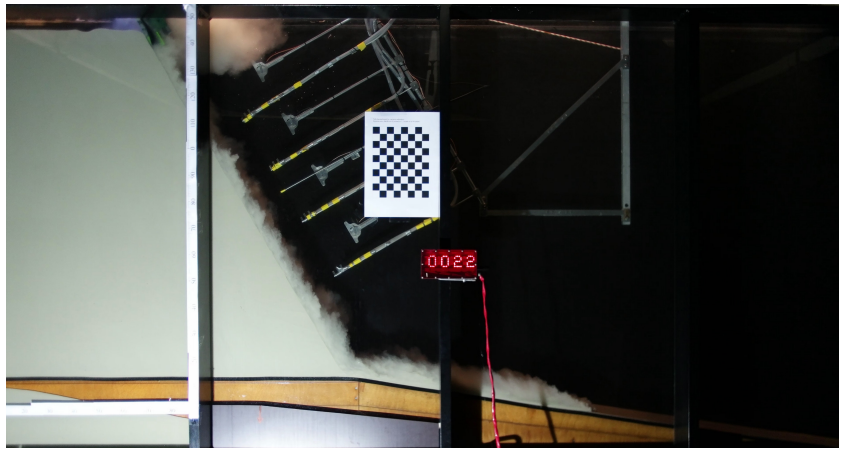

Figure 3.7: Generation of a plume of sand particles upon the removal of the confining wall during the 60° experiment. The digital clock refers to the time of the UVP measurements and the checkerboard was used in combination with the horizontal and vertical rulers for camera calibration.

Care is taken to ensure that the majority of the siphons are located within the current before obtaining the siphon samples. This is done by maneuvering the lever and the measuring post. The samples were taken at four points along the breach face. Each siphon sampled a volume of 0.1 L at three different elevations along the wall normal, sometimes at just one or two elevations due to the thinness of the current or misplacement of siphons. The misplacement could be a result of having the lever not sufficiently parallel to the breach face or having a breach face of a variable slope. The samples were taken 7 times, at different instances, during each experiment as the slope failure evolves (see Fig. 3.8). These samples were analysed afterwards to obtain the sediment concentration by weighing and drying the samples.

Regarding the UVP measurements, attention was paid to the distance between the transducers and the breach face. This is because the transducers have a certain measurement window within which they can measure velocities. The measuring post is kept in place as long as possible to provide sufficient time for the velocity measurements. It is moved horizontally from time to time to keep track of the retrogressive erosion of the breach face. Care was taken to have the lever of the measuring post as parallel as possible to the slope. Towards this end, the inclination of the lever had to be adjusted from time to time due to the steepening of the breach face. The measurements taken during the adjustment of the measuring post are entirely ignored.

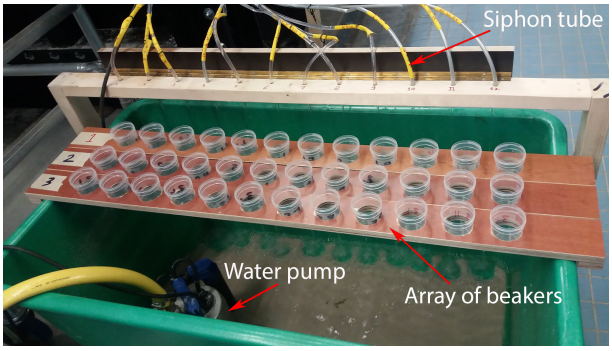

Figure 3.8: The technique of collecting the siphon samples: the array of beakers is pushed forward to simultaneously collect the samples coming through the tubes in the beakers; the water pump is used to avoid the overspill of water.

The tip of the CCM probe is initially placed as close as possible to the breach face to measure the majority of the concentration profile at the selected measuring point. The position of the CCM is kept constant in space while the breach face is progressively moving backward due to the erosion process (Fig. 3.9). In this way, assuming a steady flow, the concentration profile can be obtained.

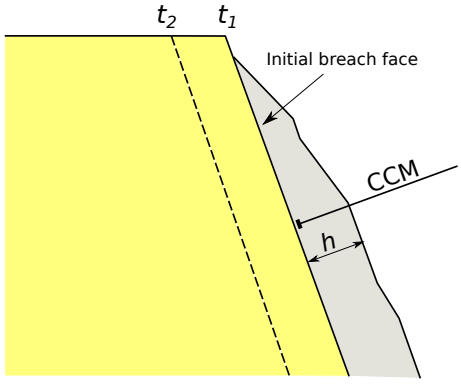

Figure 3.9: Measuring concept by the CCM: t_1 is the initial time and t_2 is the final time for the concentration measurements of a certain concentration profile; the dotted line refers to the breach face at t_2.

Monitoring the breach face changes during each experiment by video measurements allowed the reconstruction of time-varying bed profiles. These proved useful in calculating the erosion rate at different positions along the breach face as well as the rate of deposition of sediment at and beyond the breach toe. Bed elevation changes were easily estimated from the video and still photographs. Turbidity current thicknesses were determined from still photos and from the velocity profiles obtained by the UVP transducers.

3.3.3. DATA PROCESSING

VELOCITY PROFILES

The temporal resolution for each of the four UVP transducers was 74–90 ms (the real measurement time is a function of the selected velocity resolution, which is a function of the frequency of the transducers). The raw velocity data was first filtered for unwanted noise and spikes; a three-point moving average replaced all data outlying two standard deviations (see Fig. 3.10). The time-averaged, bed-normal velocity profiles are a result of averaging 40 successive instantaneous profiles, covering about 3 seconds (Fig. 3.11). Through the video measurements, the angle of the UVP transducers relative to the normal of the breach face was measured in order to adjust the magnitude of the velocities accordingly.

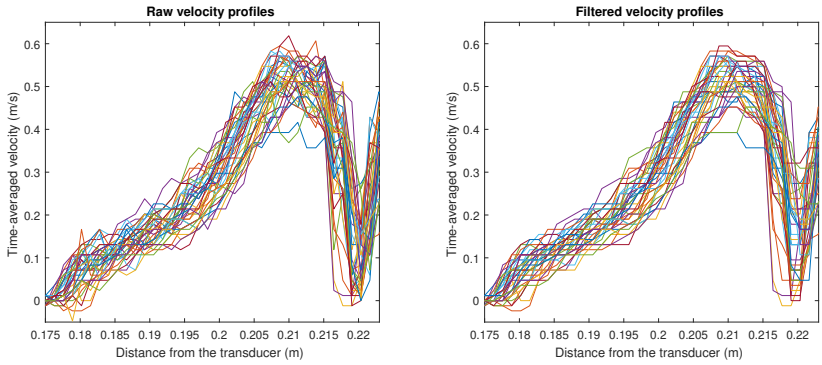

Figure 3.10: UVP data processing: raw velocity profiles 50° experiment (**left**) and filtered velocity profiles (**right**).

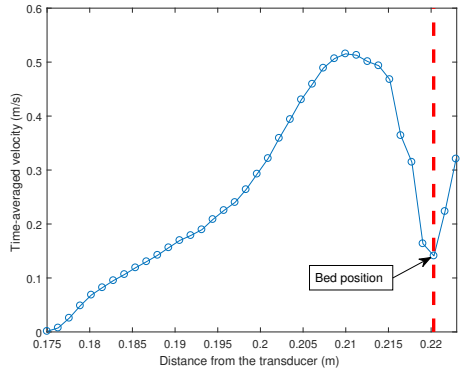

Figure 3.11: Three-second-averaged velocity profile for the 50° experiment showing reconstruction of the bed position; each marker represents a point where velocity data is available.

The UVP transducers were positioned almost in the middle of the tank width. Due to the transverse concavity of the breach face that developed during the experimental runs (see Section 3.4.3), it was not possible to pinpoint the bed position at the transducers directly from the video recordings. Therefore, as to further analyze the data, the bed position was assumed to coincide with the position of the minimum velocity captured in the near-bed region, which was determined from the time-averaged velocity profile. It is to be noted that

this assumption is not necessarily correct and might affect the self-similarity analysis of the velocity profiles (see Subsection 3.4.2). Fig. 3.11 shows some velocity recordings beyond the derived bed position, which is due to reflection of the signal off the bed and therefore ignored in the analysis. Also, in the near-bed region, the velocity of the current should presumably vary from zero (at the bed) to a higher velocity (above the bed), which is clearly not the case in the velocity profiles obtained by the UVP (see Fig. 3.13). This artefact is caused by the high near-bed particle concentration, leading to some noise in the instantaneous velocity profiles, and by the movement of the breach face (at a rate of a few mm per second) during the averaging interval for the mean velocity profiles.

CONCENTRATION PROFILES

Concentration profiles are partially acquired from the measurements conducted on the flow samples obtained by the siphons. The samples, taken at different heights from the breach face, provide time-averaged values of the particle concentration on the time span - about 6 seconds - necessary to fill the sample. The UVP backscatter signal was thus calibrated with siphon samples and utilized for estimating the distribution of suspended sediment concentration within the current. The reader is referred to *Pedocchi and García* (2012) for a detailed description of the inversion of the acoustic backscatter measured with the UVP to acquire suspended sediment concentrations.

The particle concentrations of breaching-generated turbidity currents are high, particularly near the bed, attenuating the acoustic signal. As a consequence, the derived concentration profiles by the UVP backscatter signal do not cover the entire layer thickness. The missing part of the concentration profiles in the near-bed region is therefore estimated by fitting an interpolation function to the concentration profile. The concentration profiles obtained by the CCM (see Fig. 3.15) confirmed that an exponential fit is sufficiently accurate for this purpose. At the bed position, which is obtained from the UVP measurements, a densimetric particle concentration is assumed of 1298.5 kg/m^3, corresponding to the maximum (or loose-state) porosity of 0.51. In this way, an estimate of the entire concentration profile can be obtained that corresponds to the simultaneous velocity profile.

LAYER-AVERAGED QUANTITIES

Using the velocity and concentration profiles, it is possible to determine an associated characterizing height h [m], layer-averaged velocity U [m/s] and layer-averaged volumetric concentration C [-] of the turbidity current based on the following relations (*Parker et al.*, 1986, 1987; *Garcia and Parker*, 1993),

$$Uh = \int_0^{z_\infty} u \, \mathrm{d}z, \tag{3.3}$$

$$U^2 h = \int_0^{z_\infty} u^2 \, \mathrm{d}z, \tag{3.4}$$

$$UhC = \int_0^{z_\infty} cu \, \mathrm{d}z \tag{3.5}$$

where u [m/s] is locally averaged streamwise flow velocity, c [-] is the local concentration of suspended sediment, z [m] is upward-normal coordinate and z_∞ is the height at which the local velocity u is zero. The quantities h, U, and C are obtained by solving the system of equations 3.3-3.5.

3.4. EXPERIMENTAL RESULTS

3.4.1. GENERAL FAILURE DESCRIPTION

Upon removal of the confining wall, the underwater sand deposit started to fail as particles peel off one by one, creating a shower of sand which drags the ambient water along to generate a downward turbidity current (see Fig. 3.12). This current makes a turn at the slope toe and propagates as a net-depositional current over the downstream region, where it exchanges sediments with the bed through erosion and deposition processes. In contrast to the current along the downstream region, no distinct current head was formed for the current along the breach face (Fig. 3.7), as the sand particles fail everywhere along the breach face. The sediment started depositing at the breach toe, where the current made a turn. The current downstream of the breach toe emplaced a wedge-shaped deposit with a much milder slope than the breach face. The final slope of the deposit accumulated at the downstream region (see Fig. 3.12) ranges from 13° to 21° with lower values corresponding to steeper initial breach faces.

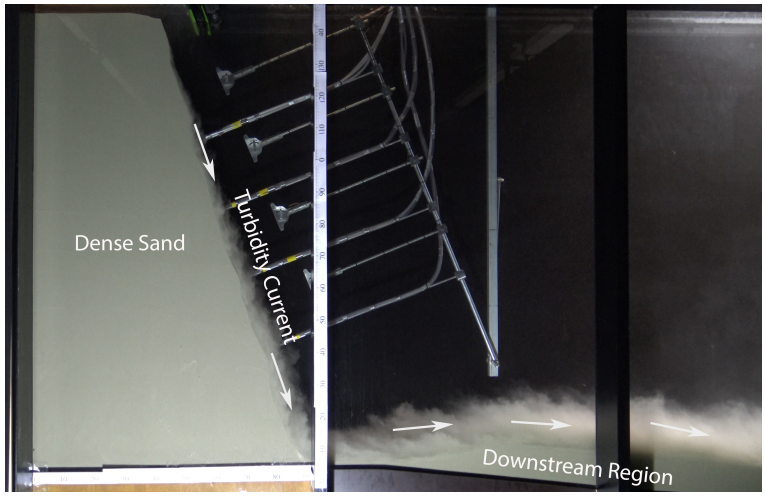

Figure 3.12: The experiment in progress: the turbidity current and the deposition of sediments in the downstream region.

At the breach face, an overhang develops from time to time, leading to the slide of an internally coherent sand wedge (surficial slide) and then the uppermost part of the breach face would relax toward a milder slope (see Fig. 3.23). The retreat of the breach face and the ensuing sand deposition at and beyond the breach toe resulted in a breach face that migrated upstream and gradually decreased in height. The retrogressive erosion lasts until a slope smaller than the internal friction angle is formed.

In the following, we will first analyse the turbidity current by considering velocity and concentration profiles and the overall development of the suspension layer along the breach slope, respectively. To focus the analysis on the spatial variability of the flow, results will be documented for situations when the slope angle was almost constant along the breach face, which reduces the number of variables. Spatially varying breach slopes will be considered when analysing the sand erosion along the slope resulting from the turbidity current. Finally,

we will consider the influence of the turbidity current relative to the gravity.

3.4.2. ANALYSIS OF THE TURBIDITY CURRENT

VELOCITY PROFILES

Fig. 3.13 shows measured profiles of the mean streamwise flow velocity together with the corresponding *in-situ* positions of the UVP transducers, for momentary slope angles of 70°, 64° and 50°, with initial slopes of 65°, 60° and 50°, respectively. For the 70° slope, the velocity profile of Transducer 4 is not reported in Fig. 3.13b, due to the local interference of the turbidity current with the bed downstream of the breach face, see also Fig. 3.13a.

The observations clearly demonstrate the characteristic velocity profiles associated with breaching-generated turbidity currents. Moving up from the breach face, the velocity quickly increases, reaching the maximum located in the near-bed region of the current. Beyond the peak, the velocity gradually decreases to become zero at the interface of the current with the ambient water. Generally, the peak velocity increases with the streamwise distance along the slope and with the steepness of the slope, reaching maximum values up to 0.90 m/s in our experiments. The thickness of the velocity layer (or velocity profile) develops in a similar fashion, increasing from typically one to a few cm near the crest of the slope to 5-9 cm near the toe, with the largest thicknesses occurring for the steeper slopes. The development of the layer-averaged flow velocity along the slope is analysed in Section 3.4.2.

To assess whether or not the observed velocity profiles are self-similar, non-dimensional velocity profiles are shown in Fig. 3.14, in which the flow velocity and distance to the bed have been scaled with, respectively, the layer-averaged velocity U and the layer thickness h as obtained from Eqs. 3.3-3.5. Indeed, the results suggest self-similarity, moreover so for Transects 3 and 4 further down the slope. For Transect 1, especially that of the 50° slope, self-similarity can not be demonstrated convincingly because the uncertainty in the derived bed position is relatively large compared to the associated layer thickness.

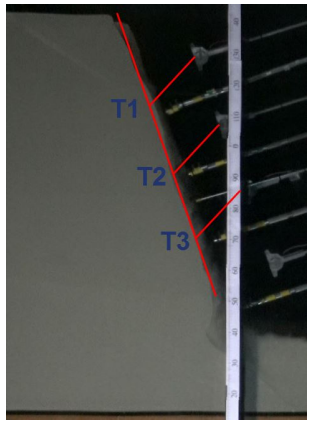

(a)

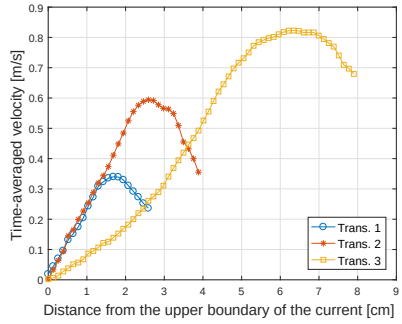

(b)

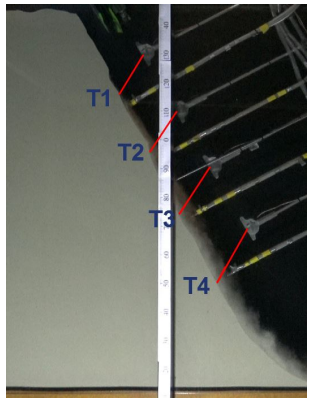

(c)

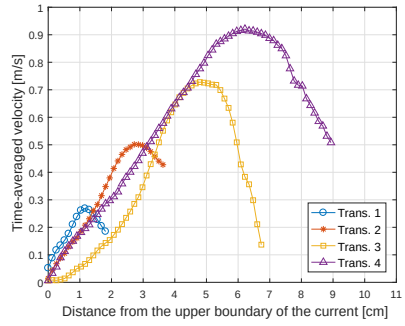

(d)

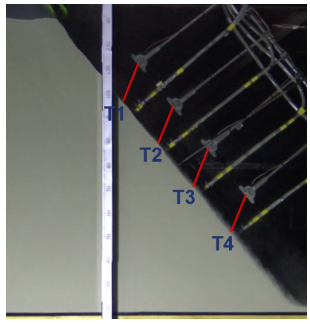

(e)

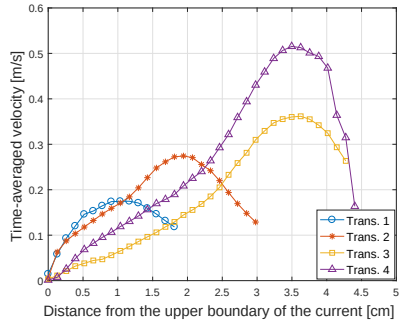

(f)

Figure 3.13: Positions of the UVP transducers (left panels) and corresponding profiles of the mean flow velocity (right panels): 70° slope - initially 65° (**a-b**), 64° slope - initially 60° (**c-d**); 50° slope - initially 50° (**e-f**).

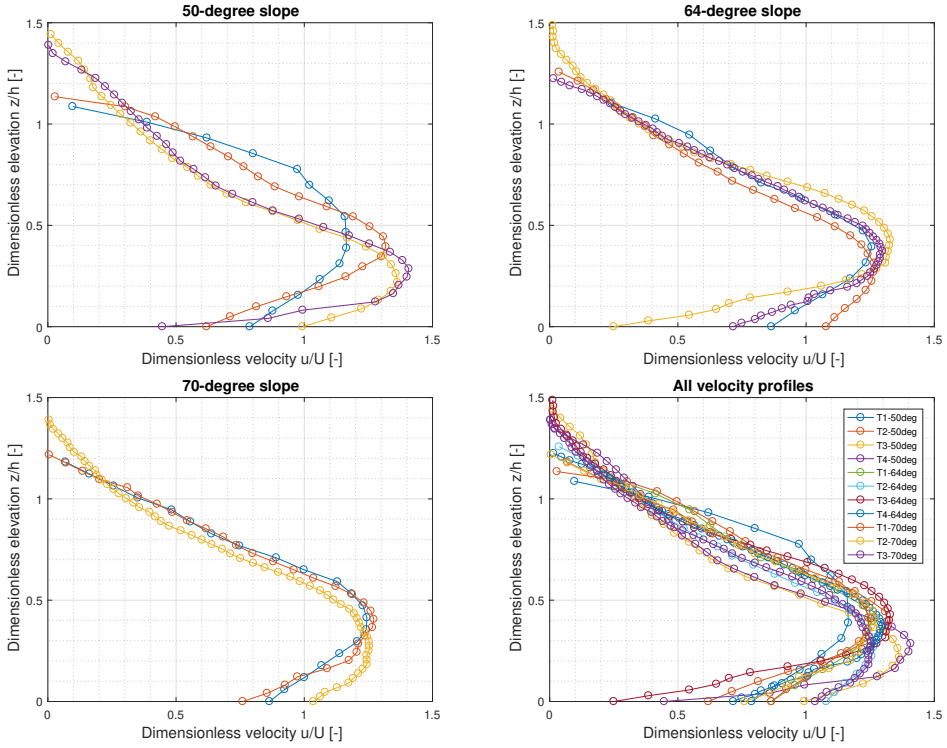

Figure 3.14: Dimensionless velocity profiles: 70° slope - initially 65° (**top left**), 64° slope - initially 60° (**top right**); 50° slope - initially 50° (**bottom left**); all slopes (**bottom right**).

CONCENTRATION PROFILES

Concentration profiles derived from the CCM measurements and the corresponding *in-situ* probe locations are shown in Fig. 3.15, for momentary slope angles of 77°, 67° and 54°, with initial slopes of 70°, 65° and 50°, respectively. The measurements are smoothed over 1 s time intervals, using a moving average filter, to obtain time-averaged concentration profiles. The momentary distance from the tip of the fixed probe to the moving bed, needed to calibrate each profile, was determined from the observed erosion rate at the respective CCM position.

At the start of the measurements, the tip of the CCM was positioned almost at the bed capturing volumetric concentrations of about 0.5, for every experiment, which nearly matches the assumed maximum concentration of 0.49 at the bed. Away from the breach face, normal to the bed, the concentration swiftly decreases over a small distance and then slightly decreases to reach zero at the upper boundary of the current (right panels of Fig. 3.15). The region near the bed, where the concentration decreases rapidly, has a thickness of about 5 mm for the 77° and 67° slopes, while for the 50° slope the thickness of only 2 mm is comparatively small. It should be noted that a direct comparison of the profiles is not possible as they relate to different positions along the slope. However, the measurements confirm that the concentration decays exponentially away from the bed.

The acoustic backscatter measurements provide simultaneous data of concentrations and velocities for the same transect, which requires calibration with the siphon samples. A sufficient number of adequate samples could be obtained for relatively thick layers only, specifically, for Transects T3 and T4 of the 64° slope (initially 60°), and for Transect T4 of the 70° slope (initially 65°). At all other transects, the layer was too thin to collect more than one siphon sample. All the obtained concentration profiles do not cover the near-bed region, and are therefore interpolated from the observed data points using an exponential fit, as confirmed by the CCM measurements. At the bed position, which is inferred from the velocity data, a volumetric sediment concentration of 0.49 is imposed. The resulting concentration profiles are shown in Figs. 3.16 and 3.17, and will be used further on to assess the spatial development of the layer-averaged concentration.

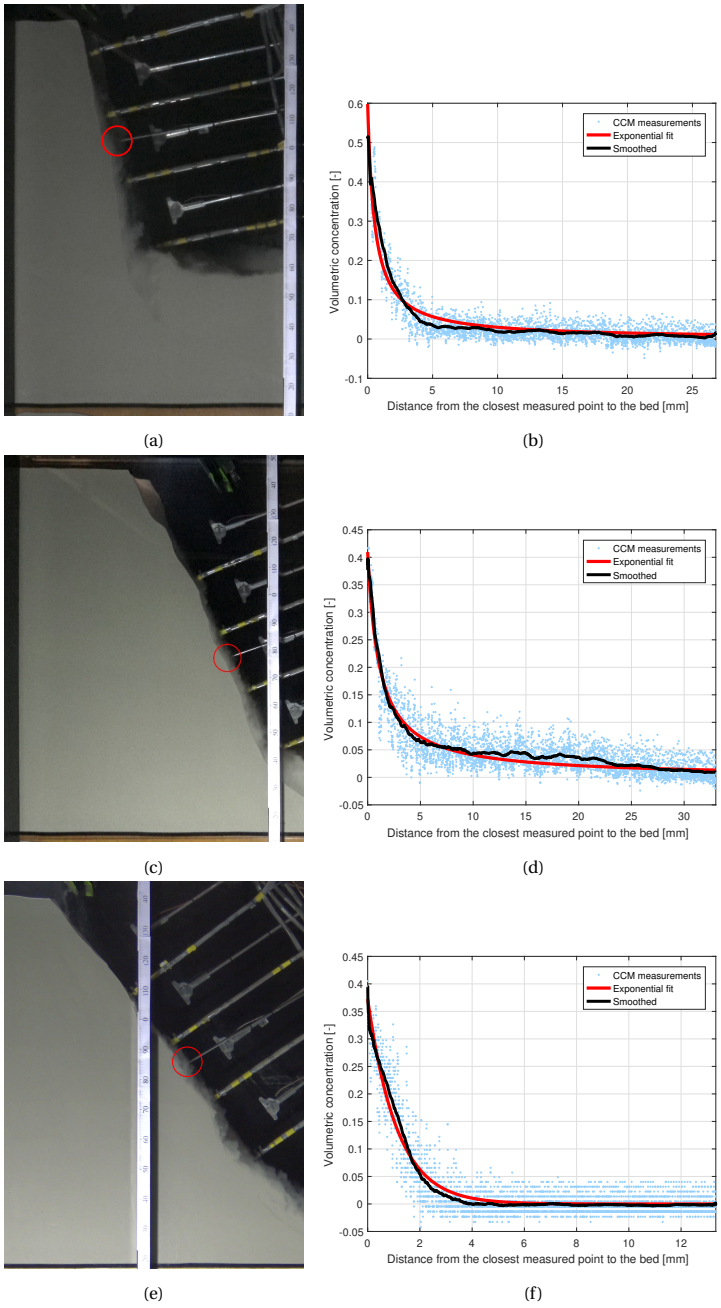

Figure 3.15: Location of the CCM probe (left panels) and corresponding sediment concentration profiles (right panels): 77° slope - initially 65° (**a-b**), 67° slope - initially 65° (**c-d**), 54° slope - initially 50° (**e-f**); the black lines indicate concentration profiles averaged over a 1 s sampling interval, while red lines indicate an exponential fit.

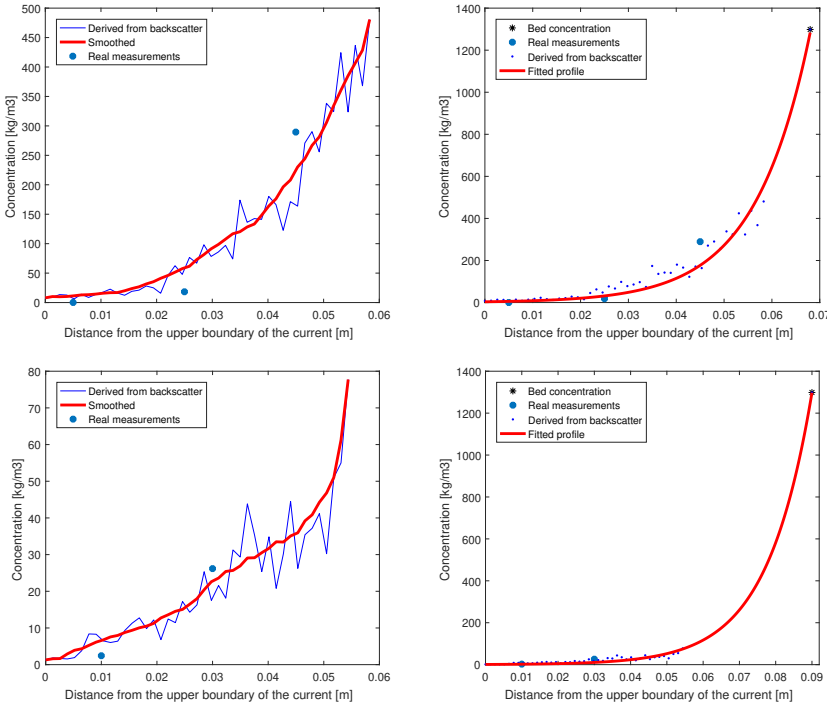

Figure 3.16: Concentration profiles for a slope of 64° (initially 60°): Transducer T3 at 81 cm from the crest (**top**), Transducer T4 at 106 cm from the crest (**bottom**); left panels show incomplete concentration profiles derived from acoustic backscatter measurements (blue line), concentrations from the siphon samples (blue dots), and smoothed (red line) concentration profiles; right panels show concentrations from the siphon samples (large blue dots), calibrated concentrations (small blue dots), inferred bed position and concentration (asterisks), fitted exponential concentration profile (red line).

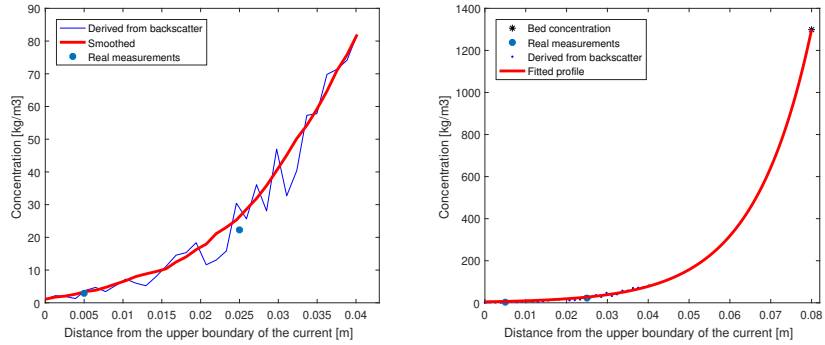

Figure 3.17: Concentration profiles for a slope of 70° (initially 65°) at Transducer T3, 76 cm from the crest: left panels show incomplete concentration profiles derived from acoustic backscatter measurements (blue line), concentrations from the siphon samples (blue dots), and smoothed (red line) concentration profiles; right panels show concentrations from the siphon samples (large blue dots), calibrated concentrations (small blue dots), inferred bed position and concentration (asterisks), fitted exponential concentration profile (red line).

LAYER-AVERAGED PROPERTIES

Layer-averaged quantities are obtained from the UVP velocity transects and the corresponding calibrated and interpolated concentrations, using Eqs. 3.3-3.5.

Fig. 3.18 shows a comparison of the spatial development of the turbidity currents based on the slope angle. The results show that the layer-averaged velocity of the turbidity current increases in the downstream direction (Fig. 3.18) as a result of the increased suspended sediment concentration (see Table 3.3) due to sand entrainment from the breach face. In other words, the turbidity current strengthens itself in the downstream direction. This implies that the breaching-generated turbidity currents are self-accelerating (*Sequeiros et al.*, 2018). Unsurprisingly, the steeper the slope, the higher the flow velocities and the larger the flow thicknesses. Turbidity currents over a steeper bed tend to have higher downward velocities and simultaneously a larger volume of entrained water from the upper boundary, which increases the layer thickness in the downstream direction.

Table 3.3 summarizes the main flow and sediment transport characteristics at four locations separated by a distance of 24 cm for the 64° slope (initially 60°). It can be noticed that the flow at these locations is supercritical (Froude number Fr_d >1), which is likely a necessary condition for the occurrence of self-accelerating turbidity currents (*Sequeiros et al.*, 2018). Furthermore, the sediment transport increases significantly in downslope direction, which is attributed to the increased total discharge in the current rather than the layer-averaged concentration - which hardly varies between these locations. This observation confirms the important role played by the water entrainment at the upper boundary of the layer. As such, this entrainment will largely determine the gradient of the downslope sediment flux leading to steepening and collapsing of the slope morphology.

The water entrainment coefficient e_w, which is a function of the bulk Richardson number $Ri = 1/{Fr_d}^2$, can be calculated using the relation proposed by *Parker et al.* (1987). The values of Fr_d and thus the corresponding values of Ri and e_w are consistent with the range of values reported in the literature (e.g., *Sequeiros* (2012)). The rate of water entrainment $v_{\text{ent}} = Ue_w$ is also presented in Table 3.3. The results show that e_w and v_{ent} tend to increase in the streamwise direction, meaning that larger volumes of water entrain into the turbidity current, thereby increasing the flow thickness while slowing down the flow.

To show the self-accelerating behavior of the current even more clearly, we present the amount of suspended sediment S_s [kg/m^2] within the current at each cross section, which is defined here as the area under the concentration profile. The results show an increase of S_s in the downstream direction similar to the increase of U and U_{max}, evidencing that the increase of the flow velocity is caused by the increase of the particle concentrations.

Table 3.3: Main characteristics of the flow and sediment transport at four locations along the 64° slope (initially 60°).

Transducer	X [m]	U [m/s]	h [m]	Uh [m^2/s]	C [-]	UhC [m^2/s]	S_s [kg/m^2]	Fr_d [-]	Ri [-]	e_w [-]	v_{ent} [mm/s]	Re $\times 10^3$ [-]
T1	0.33	0.21	0.016	0.003	n.a.	n.a.	n.a.	n.a.	n.a.	n.a.	n.a.	3.17
T2	0.57	0.40	0.029	0.012	0.08	0.0010	5.3	2.04	0.241	0.0059	2.35	10.94
T3	0.81	0.55	0.045	0.025	0.10	0.0025	14.7	2.04	0.241	0.0059	3.22	23.35
T4	1.06	0.71	0.073	0.052	0.08	0.0041	15.8	2.31	0.188	0.0074	5.22	48.90

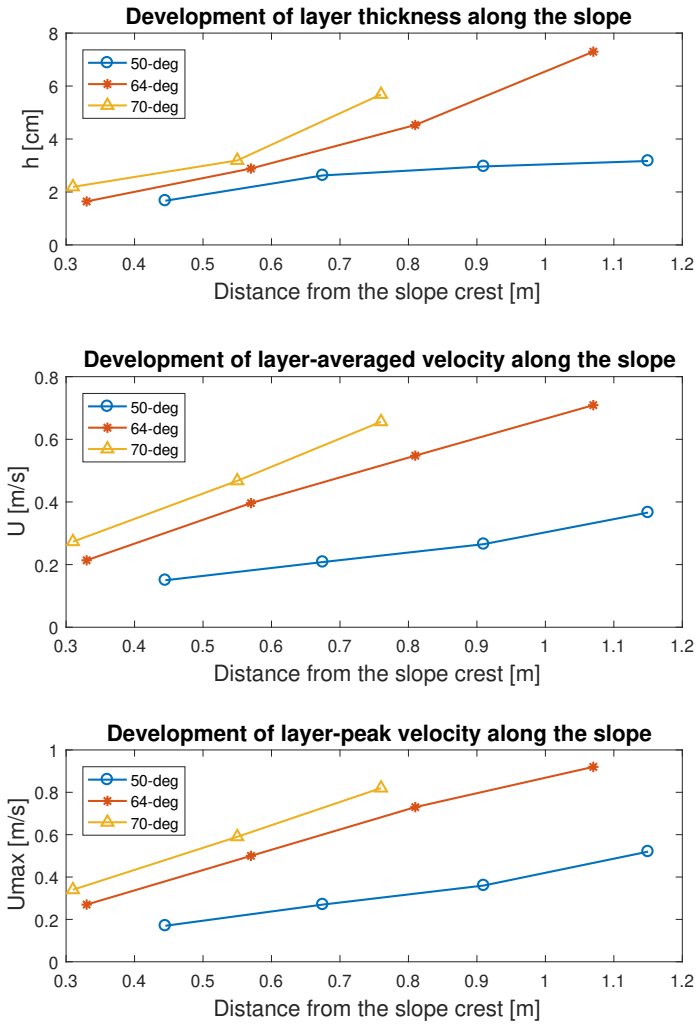

Figure 3.18: Comparison of spatial evolution of turbidity currents propagating over 50°, 64°, and 70° slopes: layer thickness development (**top**), layer-averaged velocity (**middle**), and layer-peak velocity $U_{\max}$ (**bottom**).

3.4.3. ANALYSIS OF SLOPE FAILURE

EROSION RATE

The erosion rate is defined here as the sand erosion velocity perpendicular to the breach face. Understanding how the erosion rate varies along the breach face is not only necessary to reasonably predict the total erosion rate by breaching, it is also crucial to understand the evolution of the slope failure. The erosion rates at different points along the breach face, as measured from the video recordings, are shown in Fig. 3.19. Generally, the erosion rate of the breach face increases in the downstream direction of the slope. This increase is due to the acceleration of the associated turbidity current in the downstream direction as a result of the increasing concentration of suspended sediments. In this way, the sediment entrainment and acceleration of the turbidity current are coupled in a positive feedback loop.

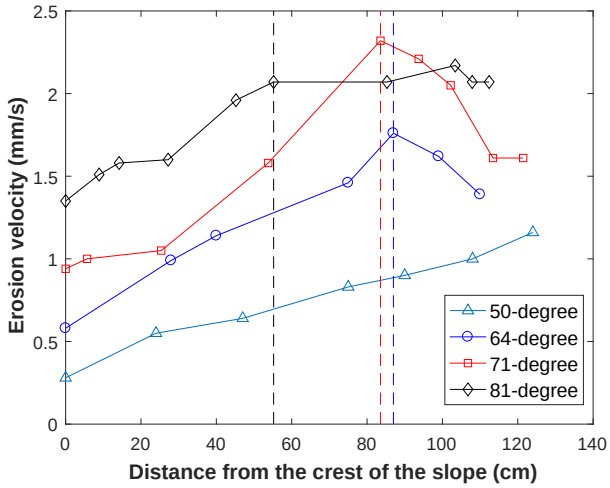

Figure 3.19: Erosion rate perpendicular to the breach face along slopes of different angles, calculated over a time interval of 15 seconds; the vertical, dashed lines refer to the transitions in erosion behavior.

However, for slope angles steeper than 50°, there is a transition where the erosion rate starts to decrease, or becomes constant, further down the slope (Fig. 3.19). The steeper the slope, the closer to the crest this transition occurs. The reason for this transition was not investigated in this work, but we speculate that it is related to turbulence damping. The turbidity current, driven by the suspended sediments, involves a turbulence shear stress which causes the resuspension of sediment. However, the resulting density stratification will also dampen the turbulence. The self-enhancing process can therefore only continue until turbulence production and damping are in equilibrium (*Cantero et al.*, 2012). Based on this argument, it is expected that the erosion rate for the 50° slope would also transition, if only further downstream than what was possible to document in the performed experiment. *Sequeiros et al.* (2009) have reported self-accelerating turbidity currents to become depositional with increasing sediments size, suggesting such a transition.

All this does not yet mean that the gravity-induced, grain-by-grain failure (absence of flow-induced erosion) is only of minor importance. Rather, this mechanism of 'pure breaching' initiates the slope failure and determines the erosion at the crest of the slope, thus

providing the initial and boundary conditions for any mathematical model of slope erosion. We therefore compare the physics-based equation for the wall velocity (Eq. 3.1) with the observed erosion rates. To this end, the erosion rates at the crest and some neighbouring points - where the velocities of the turbidity current are almost zero - are derived from the video measurements and averaged. The obtained value is considered the erosion rate for pure breaching. The comparison with Eq. 3.1 is shown in Fig. 3.20 for four slope angles corresponding to the range of the experiments. This comparison shows that the overall agreement between the theoretical expression and the experimental results is quite good, although the theoretically derived wall velocity tends to overestimate the erosion rate of pure breaching. In particular, the trend with respect to the slope angle, α, is reproduced well indicating that Eq. 3.1 captures the relevant physics consistently.

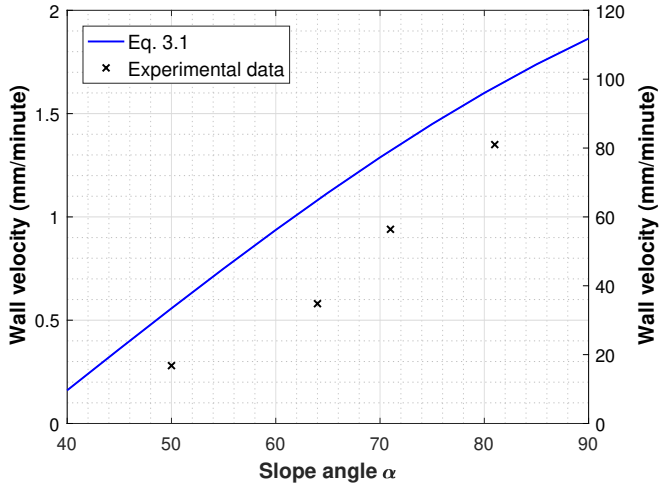

Figure 3.20: Comparison between computed wall velocity (using Eq. 3.1), and measured wall velocity (15 sec. mean).

BREACH FACE MORPHOLOGY

The temporal bed morphology evolution (Fig. 3.21) distinctly demonstrates that the lower part of the breach face erodes more quickly than the upper part, resulting in the steepening of the breach face over time. The process underlying this steepening is the self-enhancing turbidity current causing an increasing sediment erosion in downslope direction. This steepening also leads to the occurrence of so-called surficial slides, intermittent failures due to confined slope overhangs, which will be discussed in the next subsection. Note while inspecting the failure evolution that surficial slides might have taken place between two consecutive bed profiles. The slope evolution is, therefore, not entirely governed by the entrainment of sediment from the breach face.

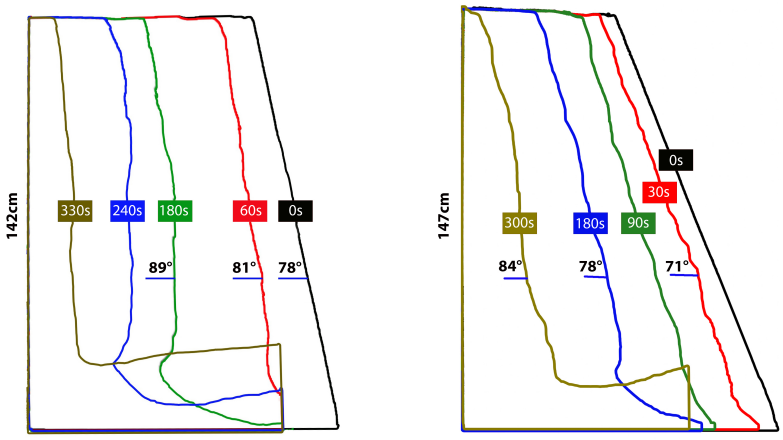

Figure 3.21: Slope steepening during breaching: 80° experiment (**left**) and 70° experiment (**right**).

It has also been clearly observed that the breach face is not uniform across the tank width. The erosion is highest almost in the middle between the tanks walls, and declining towards the walls. In other words, the breach face assumes an inward curve, looking into the direction of the erosion (Fig. 3.22). This is consistent with the final morphology of breaching events reported in the literature which also take a concave shape (e.g., *Beinssen and Mastbergen*, 2017). The combination of video recordings and UVP measurements shows that the location of the breach face at the tank walls may differ from its location in the middle of the tank width by a distance of 2 to 3 cm. This shape remains fairly stable during the progression of the breach face. This equilibrium shape implies a laterally uniform backward erosion velocity, while the erosion velocity normal to the breach face decreases towards the tank wall. It is conjectured that the latter is not only a result of deviating soil properties near the wall (e.g., permeability, shear strength), but is also related to the lateral structure of the turbidity current. This implies that the three-dimensionality of the current and of the soil structure, respectively, plays an important role in the breaching problem.

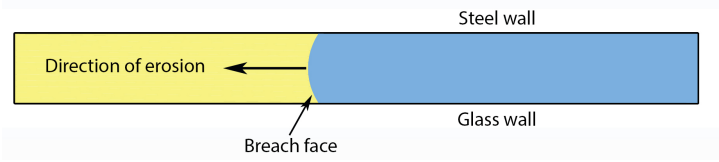

Figure 3.22: Sketch of the top view of the sand deposit showing the non-uniformity of the erosion across the breach face.

SURFICIAL SLIDES

As the lower part of the breach face erodes faster than the upper part, the breach face steepens over time. This steepening leads to overhanging and ultimately the collapse of a coherent mass of sediment, referred to as a 'surficial slide' (Fig. 3.23). These slides are always found to take place at the uppermost part of the breach face.

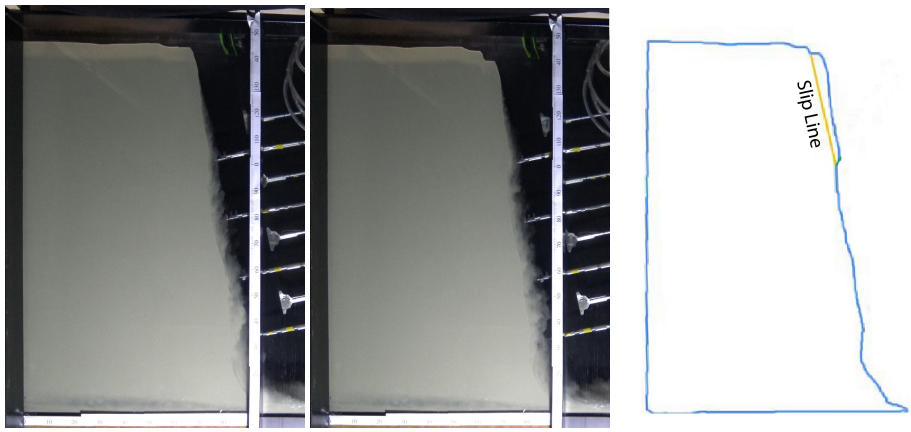

(a) Just before the surficial slide (b) Ongoing surficial slide (c) Slip line

Figure 3.23: An example of surficial slides, experiment of 80° initial slope.

The surficial slides were tracked through the video recordings to find out more about their physics. The frequency, average area and average sliding velocity of the surficial slides were determined for three different experiments (Table 3.4). It was found that all of these characteristics correlate with the angle of the breach face; steeper slopes lead to more frequent slides, larger slides and higher sliding velocities. Also, the shear stress acting on the slip plane due to the overhang submerged weight, just before the occurrence of the slides, was calculated from the slid areas and masses (not included in Table 3.4). Interestingly, for more than 75% of the surficial slides, the shear stress prior to sliding was between 130 and 140 N/m^2. This implies that the overhang slides downslope under the influence of gravity when the shear stress on the slip plane exceeds the shear strength of the sand.

Table 3.4: Statistical analysis of surficial slides observed through the glass for three different experiments.

Initial slope angle [°]	60	70	80
Number of slides [-]	8	10	20
Sliding frequency [Hz]	0.019	0.033	0.056
Average slid area [cm^2]	27.81	32.56	3.66
Average sliding velocity [cm/s]	2.92	3.66	5.28

Surficial slides temporarily enhance sediment erosion and the suspended sediment concentration, rendering the flow even denser and thus faster. Figure 3.24 shows a local, sudden increase in the concentration profile measured by the CCM due to a small surficial slide. It remains to be investigated how important the intermittent surficial slides are for the bulk behavior of the turbidity current and the associated overall evolution of the slope.

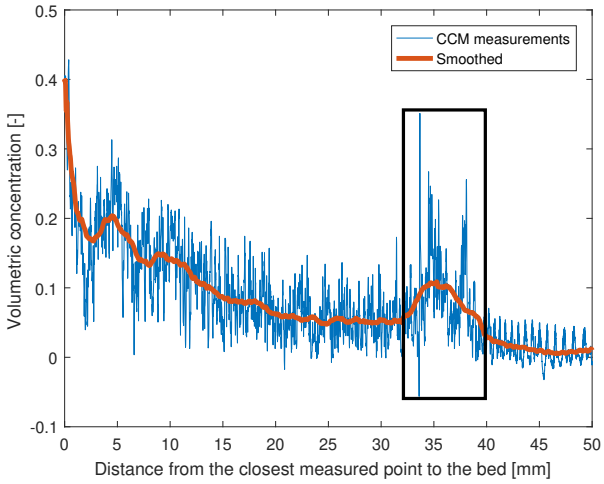

Figure 3.24: Abrupt increase of sediment concentration due to an observed small surficial slide, experiment of 65° initial slope.

RELATIVE INFLUENCE OF GRAVITY AND TURBIDITY CURRENT

Even though breaching in the first place is a gravity-induced failure, the generated turbidity current seems to start dominating the failure just after its onset until the final deposition of the sediments. This argument is based on several reasons. The turbidity current accelerates rapidly and could become capable of entraining sediments from the breach face more than the sediments falling due to the gravitational force (see Fig. 3.19). Besides, it was shown that the turbidity current could be the primary reason why the surficial slides take place. Furthermore, the run-out distance and hence the fate of the sediments are governed by the hydrodynamics of the turbidity current. Crucially, the influence of the turbidity current determines whether the breaching process is stable (the height of the breach face decreases over time) or unstable (the height of the breach face increases over time). A complete physics-based theory for this influence is not yet available, but *Van Rhee* (2015) presents an empirical relationship to predict whether the breaching process is stable or unstable.

3.5. CONCLUSION

The results from a series of physical experiments on breaching flow slides reveal that breaching-generated turbidity currents are self-accelerating; sediment entrainment and flow velocity enhance each other. Consequently, the erosion rate of the breach face increases in the downstream direction of the slope until a certain threshold, possibly due to turbulence damping. Although breaching is essentially a gravity-induced failure, the accompanying turbidity current dominates the failure evolution. This implies that successful numerical simulations of breaching flow slides must be capable of reproducing the hydrodynamics and sediment transport of turbidity currents. The expression of wall velocity generally coincides with measured erosion rate of pure breaching, but tends to overestimate it. This fact should be accounted for when attempts are made to extend the expression of wall velocity to an erosion closure model including sediment entertainment by turbidity currents. Finally, the

variation of the erosion rate along the breach face leads to the oversteepening of the lower part of slope. As a result, a sediment overhang develops and eventually slides downslope under the pull of gravity, when the shear stress on the slip plane exceeds the shear strength of the sand. These slides considerably enhance local sediment erosion, implying that they should be incorporated in breaching erosion closure models.

The measurements collected during the experiments allowed for a fundamental understanding of the coupled interaction between the breach face and turbidity currents. Yet, these measurements are not sufficient to obtain turbulence quantities and subsequently to estimate the shear stress exerted by the flow on the breach face. This forms an impediment towards proper validation of existing breaching erosion closure models or the development of a new one. However, an advanced flow numerical model would offer a complementary tool to obtain detailed results of the flow and hence to develop a better insight into the anatomy and behavior of breaching-generated turbidity currents. This will be the topic of Chapter 4.

4

LARGE EDDY SIMULATIONS OF BREACHING-GENERATED TURBIDITY CURRENTS

Breaching flow slides result in a turbidity current running over and directly interacting with the eroding, submarine slope surface, thereby promoting further sediment erosion. The investigation and understanding of this current are crucial, as it is the main parameter influencing the failure evolution and fate of sediment during the breaching phenomenon. In contrast to previous numerical studies dealing with this specific type of turbidity currents, we present a 3D numerical model that simulates the flow structure and hydrodynamics of breaching-generated turbidity currents. The turbulent behaviour in the model is captured by large eddy simulation (LES). We present a set of numerical simulations that reproduce the experimental results presented in Chapter 3. Through these simulations, we show the validity, applicability, and advantage of the proposed numerical model for the investigation of the flow characteristics. The principal characteristics of the turbidity current are reproduced well, apart from the layer thickness. We also propose a breaching erosion closure model and validate it using the same series of experimental data. Quite good agreement is observed between the experimental data and the computed erosion rates. The numerical results confirm that breaching-generated turbidity currents are self-accelerating and indicate that they evolve in a self-similar manner.

This chapter has been published as Alhaddad, S., de Wit, L., Labeur, R. J., and Uijttewaal, W. (2020). Modelling of Breaching-Generated Turbidity Currents Using Large Eddy Simulation. Journal of Marine Science and Engineering, 8(9), 728. https://doi.org/10.3390/jmse8090728

4.1. INTRODUCTION

Turbidity currents are underwater flows driven by buoyancy and formed by the influence of gravity on the density difference between a fluid-sediment mixture and the ambient fluid (*Meiburg and Kneller*, 2010). The excess hydrostatic pressure within the turbidity current drives the current downstream while complicated interactions with the surrounding environment take place; it interacts with the ambient fluid at the upper boundary and with the bed at the lower boundary, producing turbulence at both boundaries (*Salinas et al.*, 2019). Turbidity currents are vital agents of sediment transport that deliver sediment from the river mouths to deeper waters (*Hage et al.*, 2019). Moreover, they pose a serious threat to flood defence structures, such as dikes and embankments (*Alhaddad et al.*, 2020a), and submarine structures placed at the seafloor, such as oil pipelines, and communication cables (*Paull et al.*, 2018).

Turbidity currents can be triggered through several mechanisms, such as hypopycnal river plumes (*Parsons et al.*, 2001), internal waves or tides (*Normandeau et al.*, 2014), and submarine slope failures (*Hizzett et al.*, 2018). One of the complex failure mechanisms of submarine slopes is the flow slide (*Mastbergen et al.*, 2019), which takes place when a large amount of sediments in an underwater slope is destabilized and consequently runs down the slope as a dense fluid. Two categories are distinguished: liquefaction flow slides, which occur in loosely-packed sand, and breaching flow slides, which mostly occur in densely-packed sand (*Van Den Berg et al.*, 2002; *Alhaddad et al.*, 2019). The former results in slurry-like or hyper-concentrated density flows, while the latter results in turbidity currents (*Eke et al.*, 2011). Here, the focus is on the turbidity current accompanying breaching flow slides, referred to as a breaching-generated turbidity current. These currents have proved very difficult to measure in the field, as their occurrence is unpredictable while they can also destroy the measuring instruments (*Inman et al.*, 1976; *Talling et al.*, 2013). Alternatively, laboratory experiments are widely used (e.g., *Garcia and Parker* (1993); *Kneller et al.* (1999); *Stagnaro and Pittaluga* (2014); *Ottolenghi et al.* (2017)) and can be scaled and conducted under more controlled conditions to develop a better understanding of the behaviour of turbidity currents, and to provide measurements for the validation of numerical models.

To this end, *Alhaddad et al.* (2020b) have recently conducted large-scale experiments obtaining direct measurements of breaching-generated turbidity currents and the associated sediment transport. Their analysis showed that breaching-generated turbidity currents are self-accelerating; the current strengthens itself by the accumulated erosion of sediment from the breach face. The results also suggested that the velocity profiles of these currents are self-similar. Analysis of particle concentration profiles showed that the concentration decays exponentially from the breach face until the upper boundary of the current. Near-bed concentrations were found to be high, reaching 0.4 by volume or even higher in some cases. Moreover, investigation of the slope failure indicated that its evolution is largely three-dimensional. Sand erosion rates in the middle of the tank width, where turbidity currents were measured, were found to be higher than at the tank glass wall, where the erosion rates were measured. A key finding was that the turbidity current is the main parameter controlling the evolution of the breaching failure and the fate of eroded sediment. This implies that a thorough understanding of the behaviour of this current is needed to enhance the knowledge about breaching. Owing to the several difficulties associated with breaching experiments, measurements of turbulence quantities of the flow were not possible. The absence of such measurements hinders the estimate of the flow-induced bed shear stress

and hence the predication of erosion during breaching. This highlights the need for using advanced numerical models as a complementary tool to the experimental work, to gain new insights into the behaviour and structure of breaching-generated turbidity currents.

Many numerical models for density or gravity currents have been proposed in literature (e.g., *Ottolenghi et al.* (2016); *Nourazar and Safavi* (2017); *Pelmard et al.* (2018); *Kyrousi et al.* (2018); *Lucchese et al.* (2019)). To date, however, there are very few numerical investigations dealing with breaching-generated turbidity currents (*Mastbergen and Van Den Berg*, 2003; *Eke et al.*, 2011; *Alhaddad et al.*, 2020a). Moreover, these numerical efforts were mostly restricted to layer-averaged, one-dimensional models. The model of *Mastbergen and Van Den Berg* (2003) was applied to simulate a flushing event in Scripps Submarine Canyon, and showed that breaching-generated turbidity currents are capable of excavating a submarine canyon. Similarly, the model of *Eke et al.* (2011) was applied to a flushing event in Monterey submarine canyon. These layer-averaged models require several empirical closure relations (e.g., the near-bed concentration, bed shear stress, and water entrainment at the upper boundary), which reduces the accuracy of the simulation results (*Yeh et al.*, 2013). *Alhaddad et al.* (2020a) applied the one-dimensional model of (*Parker et al.*, 1986) to a typical case of a breaching slope, demonstrating that the results are highly sensitive to the type of breaching closure relation used.

To reduce these uncertainties, this study presents large eddy simulations of breaching-generated turbidity currents. Large eddy simulations have the advantage that the larger turbulent scales - containing the bulk of the turbulent kinetic energy - are resolved. In this manner, the influence of density gradients on turbulence production is captured adequately, while including the non-isotropic character of turbulence. Therefore, large eddy simulations can provide a wealth of insights into the structure and physical behaviour of turbidity currents, in particular into the turbulence structure. The numerical model that we use has been applied earlier to gain insights into the complicated dredge plume behavior close to a dredging vessel where density differences, turbulent mixing and sediment settling play an important role (*de Wit et al.*, 2014a,b, 2015). The model has been validated for a wide range of flow cases relevant to the present study, such as the front speed of density currents radially spreading and density currents running over both flat and sloping beds, the deposition from high-concentration suspended sediment flow at a flat bed (*de Wit*, 2015), and high sediment concentration conditions encountered in hopper sedimentation (*de Wit*, 2019). In this chapter, the implementation is designed to capture the turbidity current running down the slope surface (or 'breach face'), considering various steep slope inclinations, which were tested in the laboratory experiments. The triggering mechanism of turbidity currents in this work is different from the standard lock-exchange configuration mostly used in numerical models of turbidity currents; sediment particles are released from the bed surface generating the flow. An adequate prediction of this process has always been difficult, as it involves both geotechnical and hydraulic phenomena (*Alhaddad et al.*, 2020a). To date, furthermore, no validation of existing breaching erosion closure models has been presented.

This chapter proceeds as follows. We first provide some background of the numerical model in Section 2, and propose a breaching erosion closure model in Section 3. Section 4 revisits the experimental measurements of *Alhaddad et al.* (2020b), and validates the performance and limitations of the currently proposed numerical model in characterizing the breaching-generated turbidity currents based on the experimental findings. Following that, Section 5 discusses the flow and turbulence structure and analyses the sensitivity of the

numerical results to some initial conditions.

4.2. NUMERICAL MODEL DESCRIPTION

4.2.1. GOVERNING EQUATIONS

The flow of water-sediment mixtures—as in breaching-generated turbidity currents—is mathematically described by the incompressible, variable density Navier–Stokes equations. Using the mixture approach, the concentrations of the individual sediment fractions are solved separately while one set of momentum equations is solved for the water-sediment mixture (*Manninen et al.*, 1996). Each sediment fraction has its own drift velocity $\boldsymbol{u}_d$, defined as the velocity of the sediment relative to the water-sediment mixture, which involves a correction of the mixture velocity with the settling velocity of the sediment including the influence of hindered settling. Furthermore, the sediment concentration influences the mixture density. The mixture approach combined with the concept of drift velocity is thus two-way coupling and has proved valid to simulate high-concentration suspended sediment flows (e.g., *Van Rhee* (2002); *Saremi* (2014); *Goeree* (2018); *de Wit* (2019)).

To this end, the corresponding balance equations for the total mass and momentum of the mixture are stated as, respectively,

$$\frac{\partial \rho}{\partial t} + \nabla \cdot (\rho \boldsymbol{u}) = 0, \tag{4.1}$$

$$\frac{\partial \rho \boldsymbol{u}}{\partial t} + \nabla \cdot (\rho \boldsymbol{u} \otimes \boldsymbol{u}) = -\nabla P + \nabla \cdot \boldsymbol{\tau} + (\rho - \rho_w)\boldsymbol{g}, \tag{4.2}$$

where t denotes time, ρ is the mixture density, ρ_w is the water density, $\boldsymbol{u}$ is the mixture velocity vector, P is the excess pressure over the hydrostatic pressure, $\boldsymbol{\tau}$ is the shear stress tensor, $\boldsymbol{g}$ is the gravity vector, and ∇ denotes the spatial gradient operator. The mixtures that we consider are primarily Newtonian in rheology (*Shanmugam*, 2018) for which the shear stress tensor is proportional to the deviatoric strain rate of the mixture velocity, as follows,

$$\boldsymbol{\tau} = 2\mu \left(\nabla^s \boldsymbol{u} - \frac{1}{3} \nabla \cdot \boldsymbol{u} \right), \tag{4.3}$$

where μ is the dynamic viscosity of the mixture and $\nabla^s(\cdot) = \frac{1}{2}\nabla(\cdot) + \frac{1}{2}\nabla(\cdot)^T$ is the symmetric gradient operator. It is to be noted that Equation (4.3) is valid only if the layer-averaged volumetric sediment concentration is below the Bagnold limit of ca. 9% beyond which the particle-particle interactions will render the mixture non-Newtonian (*Bagnold*, 1962). In our case, observed layer-averaged concentrations are generally below 9% (see Subsection 4.6.1), while in the center and outer region of the turbidity current, concentrations are even smaller due to the entrainment of ambient fluid and the subsequent turbulence mixing (*Mulder and Alexander*, 2001). This motivates the use of Equation (4.3), although in the inner region near the bed the relatively high concentration may require the reconsideration of additional effects on the rheology of the fluid in the boundary layer, leaving room for improvement of our model (see also the discussion in Subsection 4.5.3).

Although the mixture model admits multiple sediment fractions (*de Wit*, 2015), a single sediment fraction suffices here, as uniform sediment will be considered. In this case the mixture density is given by,

$$\rho = \rho_w + (\rho_s - \rho_w)\, c, \tag{4.4}$$

where ρ_w and ρ_s are the densities of water and sediment, and c is the volumetric sediment concentration. The latter satisfies the following transport equation,

$$\frac{\partial c}{\partial t} + \nabla \cdot (\boldsymbol{u}_s c) = \nabla \cdot (\Gamma \nabla c), \tag{4.5}$$

in which $\boldsymbol{u}_s = \boldsymbol{u} + \boldsymbol{u}_d$ is the velocity of the sediment fraction, and Γ is the diffusivity which is related to the viscosity μ by,

$$\Gamma = \frac{\mu}{\rho_w Sc}, \tag{4.6}$$

where Sc is the Schmidt number. Following *Van Rhee* (2002) and *de Wit* (2015), $Sc = 0.7$ is adopted in this study and, based on sensitivity analysis, LES results are insensitive to the value of Schmidt number when Sc is close to 1. The drift velocity $\boldsymbol{u}_d$ accounts for the effects of hindered settling (*Richardson and Zaki*, 1954) and the return flow created by the settling particles *de Wit* (2015).

For a well-posed problem, Eqs. (4.1), (4.2) and (4.5) must be supplemented with boundary conditions, while for time dependent problems also initial conditions for the sediment concentration and mixture velocity must be prescribed. Importantly, the interaction of the mixture flow with a sediment bed involves the bed shear stress $\boldsymbol{\tau}_b$, and the densimetric sedimentation flux S and erosion flux E given by,

$$S = \rho_s c_b w_s \cos\alpha, \tag{4.7}$$

$$E = \phi_{p,t} \rho_s \sqrt{\Delta g d_{50}}, \tag{4.8}$$

where c_b is a representative near-bed sediment concentration, w_s is the particle settling velocity, α is the bed slope, $\Delta = (\rho_s - \rho_w)/\rho_w$ is the relative submerged sediment density, d_{50} is the median sediment grain size, and $\phi_{p,t}$ is a non-dimensional, so-called, pick-up function involving an empirical closure relation (see Subsection 2.4.2). Given the strong feedback between bed erosion and the hydrodynamics of the turbidity current, the formulation of the pick-up function requires special care in order to accurately predict the temporal evolution of the slope failure. Section 4.3.3 will further elaborate on the available theoretical background of sediment erosion during breaching, resulting in the proposed erosion closure model.

4.2.2. TURBULENCE MODELLING

In our implementation, Eqs. (4.1), (4.2) and (4.5) are discretized using a regular rectangular grid with, possibly non-uniform, grid sizes (Δx, Δy, Δz in the respective Cartesian directions). Depending on the grid size, the finite resolution of the computed flow field can only partly include the relevant turbulence length scales. To account for the effect of the unresolved scales on the resolved flow field a turbulence closure model must be used.

In this study, Large Eddy Simulation (LES) is adopted to capture the influence of turbulence. LES applies a spatial filter in which turbulence length scales larger than the grid size are resolved, and the smaller isotropic turbulence scales are accounted for by the sub-grid-scale model. In other words, the unresolved turbulence quantities are expressed in terms of the resolved flow filed. By choosing the grid size sufficiently small, the major part of the turbulent kinetic energy is resolved on the grid and only a small part is modelled by the sub-grid-scale model. An advantage of LES over Reynolds-averaged Navier–Stokes modelling (RANS) is

that turbulence damping or destruction functions at sharp density gradients are not needed when sufficient grid resolution is used. This is because the influence of density gradients on the resolved turbulent eddies is automatically taken into account in LES. Furthermore, the non-isotropic behaviour of the larger turbulence length scales is resolved in LES. Noteworthy to mention in this respect is that the behaviour of the inner region of the turbidity currents, as observed in the experiments, is highly affected by both damping and anisotropy of the turbulence motion in this region.

Following the LES approach, the eddy viscosity is modified to account for the influence of turbulence. To this end, the molecular viscosity μ_{mol} is enhanced with an extra sub-grid-scale viscosity μ_{sgs}, as follows,

$$\mu = \mu_{\text{mol}} + \mu_{\text{sgs}}, \tag{4.9}$$

where μ_{sgs} is a function of the strain rate tensor and the grid size,

$$\mu_{\text{sgs}} = \rho \left(C_S \left(\Delta x \Delta y \Delta z \right)^{1/3} \right)^2 \|S\|, \tag{4.10}$$

in which C_S is the dimensionless Smagorinsky constant, and $\|S\|$ is the norm of the (filtered) velocity gradient tensor. For the latter, the WALE (wall adapting eddy viscosity) sub-grid-scale turbulence model is adopted together with a constant C_S of 0.325. For details of this implementation see *Nicoud and Ducros* (1999).

Turbulence is partly generated at the sediment bed, requiring a formulation of the corresponding boundary conditions consistent with the LES approach. First of all, the bed shear stress is formulated as a partial slip boundary condition by calculating the local shear velocity u_*. This is accomplished by assuming a standard logarithmic velocity profile over the grid cell adjacent to the bed, which gives,

$$u_* = \frac{\boldsymbol{u}_t}{\kappa^{-1} \ln\left(\frac{1}{2}\Delta Z / Z_0\right)}, \tag{4.11}$$

where $\boldsymbol{u}_t$ is the (filtered) tangential velocity vector in the grid cell adjacent to the bed, κ is the Von Kármán constant, ΔZ is the cell size normal to the bed, and $Z_0 = 0.11\nu/|u_*| + k_n/30$, in which ν is the kinematic molecular viscosity of water, and k_n is the Nikuradse roughness height which is set to a value of $2\,d_{50}$. Next, the bed shear stress, $\boldsymbol{\tau}_b$, is computed from,

$$\boldsymbol{\tau}_b = \rho\, |u_*|\, u_*. \tag{4.12}$$

The corresponding magnitude of the shear velocity, u_*, is also used in the formulation of the sediment erosion flux E at the bed, which is treated extensively in Section 4.3.

4.2.3. NUMERICAL SOLUTION PROCEDURE

The spatial discretization of the model equations is based on the finite volume method, using a rectangular staggered grid in which the discrete velocity and pressure variables are located at alternating points (*Harlow and Welch*, 1965). The discretization in time conforms to a pressure-correction algorithm, which involves a predictor step in which an intermediate velocity field is computed using the pressure from the previous time step, followed by a corrector step, where the velocity and pressure are updated in a coupled fashion in order to satisfy the continuity constraint, Eq. (4.1).

In the predictor step an explicit third order Adams-Bashfort time integration scheme is employed, adjusted to be able to apply variable time step sizes. Small time steps are to

be used with the Courant–Friedrichs–Lewy number (CFL-number) staying below 0.6. The spatial discretisation of the convection terms in the momentum equations is crucial for LES and is performed by a stable scheme with very low diffusion (*de Wit and van Rhee*, 2014). Likewise, the advection term in the transport equation is discretised with an accurate and robust TVD (Total Variation Diminishing) scheme employing the Van Leer limiter.

In the corrector step, the enforcement of the continuity constraint results in a pressure Poisson equation which is solved by a fast direct solver using the method of *Dodd and Ferrante* (2014). While for incompressible single-phase flows the continuity constraint implies zero divergence of the velocity field (by setting $D\rho/Dt = 0$ in Eq. 4.1), this is generally not so for the flow of incompressible mixtures (*Prosperetti and Tryggvason*, 2007). This owes to the definition of the mixture velocity $\boldsymbol{u}$ in a densimetric manner, while zero divergence only holds for the *volumetric* mixture velocity. The latter is obtained by correcting the densimetric mixture velocity $\boldsymbol{u}$ with the respective equilibrium settling velocities from all sediment fractions - a necessary step preceding the enforcement of the zero divergence constraint.

Overall, the numerical method is second-order accurate in time and space. For more details on the numerics, the reader is referred to *de Wit* (2015).

4.3. BREACHING EROSION MODELING

Breaching can be defined as a gradual, slow, retrogressive erosion of a steep immersed slope, which is steeper than the internal friction angle of the granular material forming that slope. As noted earlier, breaching is largely encountered in densely-packed sand, as it exhibits a dilative behavior, when it is subjected to shear forces (*Van Den Berg et al.*, 2002; *Van Rhee*, 2015). Dilatancy refers to the expansion of pore volume of sand under shear deformation, which results in the build-up of a negative pore pressure, with reference to the hydrostatic pressure. This negative pressure holds sand particles together and increases the effective stress (*Van den Berg et al.*, 2017). The pressure difference involves an inward hydraulic gradient, compelling the neighboring water to flow into the sand pores, and thus releasing the negative pressure. Consequently, sand particles located at the top of the slope surface (breach face) are exclusively undermined and slowly (~mm/s) peel off, predominantly one by one (*Alhaddad et al.*, 2020a).

The falling sand particles mix with the ambient water, producing a turbidity current running along and interacting with the breach face, and then flowing down the slope toe. This causes an additional shear stress along the breach face, and hence higher erosion. In the conventional sediment pick-up functions, it is assumed that it is impossible for a grain-by-grain sediment erosion to take place in a submerged slope steeper than the internal friction angle. Rather, the erosion may occur as a sudden collapse of the sand body. Nevertheless, breaching refutes this hypothesis (*Van Rhee and Bezuijen*, 1998; *Alhaddad et al.*, 2020b), showing the need for an erosion closure model compatible with breaching conditions.

It is to be noted that beside the grain-by-grain erosion, an intermittent collapse of coherent sand wedges, termed a surficial slide, was observed in breaching experiments (e.g., *Van Rhee and Bezuijen* (1998); *Alhaddad et al.* (2020b)). The current understanding of these slides remains very limited. In this chapter, therefore, we will consider measurements where surficial slides did not take place. This implies that the total erosion will be a combination of particle-by-particle erosion induced by gravity (pure breaching) and sediment erosion induced by the flow motion. In the following, breaching erosion is decomposed into these

two main components.

4.3.1. PURE BREACHING

The Dutch industry was the first to explore breaching in the 1970s, and utilized it as an efficient production mechanism for stationary suction dredgers. In that period, breaching was not known as a failure mechanism of underwater slopes outside the dredging field. To estimate the dredging production, *Breusers* (1977) developed a formula for the erosion rate of pure breaching: particle-by-particle erosion induced by gravity. The original formula was derived for a vertical breach face, however, it can be adapted to a general form representing the erosion velocity perpendicular to the breach face for variable inclinations (*Alhaddad et al.*, 2020a):

$$v_{e,g} = -\frac{\sin(\phi-\alpha)}{\sin\phi}\,\frac{(1-n_0)}{\delta n}\,k_l\,\frac{\rho_s-\rho_w}{\rho_w}, \tag{4.13}$$

where $v_{e,g}$ [m/s] is the erosion rate of pure breaching (note that this was termed wall velocity v_w in previous chapters), ϕ [°] is the internal friction angle, n_0 [-] is the *in situ* porosity of the sand, k_l [m/s] is the sand hydraulic conductivity at the loose state, ρ_w [kg/m^3] is the density of water, and $\delta n = (n_l - n_0)/(1-n_l)$ is the relative change in porosity, in which n_l [-] is the maximum porosity of the sand.

The erosion rate of pure breaching is particularly sensitive to the magnitude of sand hydraulic conductivity k_l in a linearly-proportional fashion. This implies that the existence of finer particles within the sand considerably decreases the erosion rate of pure breaching, since they fill pore spaces and reduce permeability. Furthermore, the permeability plays a role in the fluid-induced erosion, as it will be shown in the next subsection. Fortunately, the value of the hydraulic conductivity reported in *Alhaddad et al.* (2020b) was measured in the lab, allowing for a proper validation of the current erosion closure model.

Alhaddad et al. (2020b) showed that Equation 4.13 somewhat overestimates the erosion rate of pure breaching. Therefore, we propose here an empirical correction factor of $\sin(\alpha-\phi)^{0.55}$, which leads to the expression of the corrected pure breaching $v_{e,g,c}$:

$$v_{e,g,c} = -\frac{\sin(\phi-\alpha)\sin(\alpha-\phi)^{0.55}}{\sin\phi}\,\frac{(1-n_0)}{\delta n}\,k_l\,\frac{\rho_s-\rho_w}{\rho_w}. \tag{4.14}$$

Direct measurements of different grain sizes are needed to test the general applicability of this correction factor. Fig. 4.1 depicts the performance of the original and corrected expression of the erosion rate of pure breaching. Equation 4.14 will be used in numerical runs for which no measured erosion rate of pure breaching is available.

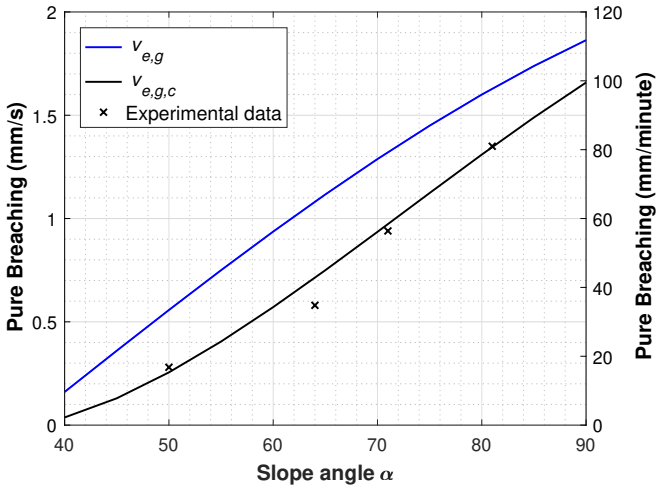

Figure 4.1: Comparison between the predictive ability of the original (Equation 4.13) *Alhaddad et al.* (2020b) and empirically-corrected (Equation 4.14) relations of the erosion rate of pure breaching: d_{50} = 0.135 mm, n_0 = 0.40, n_l = 0.51, ϕ = 36° and k_l = 0.0307 cm/s.

4.3.2. FLOW-INDUCED EROSION

Many parameters play a role in sand erosion induced by turbidity currents such as near-bed velocity gradient, flow turbulent energy, the properties of sand grains and the bulk properties of sand. In breaching, this part of erosion is more complicated than pure breaching, owing to the special conditions of the breaching process including dilatancy-retarded erosion and a very steep bed (*Alhaddad et al.*, 2020a). On the one hand, some pick-up functions are proposed in the literature to account for the dilative behavior (e.g., *Bisschop* (2018)). However, these functions do not account for a sloping bed. On the other hand, some pick-up functions account for the sloping bed (e.g., *Dey and Debnath* (2001)), but not for a slope steeper than the internal friction angle.

The literature shows, to the best of our knowledge, that only two erosion closure models were suggested to suit the conditions of the breaching problem (*Mastbergen and Van Den Berg*, 2003; *Van Rhee*, 2015). These two erosion closure models are an extension of the formula of *Breusers* (1977), meaning that they combine both the pure breaching and sediment erosion by the turbidity current. However, (*Alhaddad et al.*, 2020a) showed that the erosion rate predicted under the same conditions varies considerably between these erosion closure models.

4.3.3. TOTAL EROSION

Alhaddad et al. (2021) presented preliminary evaluation of the existing breaching erosion closure models and showed that erosion closure model put forward by *Mastbergen and Van Den Berg* (2003) performs better than the one proposed by *Van Rhee* (2015). In this work, therefore, we adopt the erosion closure model of *Mastbergen and Van Den Berg* (2003) as a basal point and develop it further to improve its predictive ability of breaching erosion. Their

erosion closure model reads

$$\frac{v_{e,t}}{u_{ss}}\left(1-\frac{v_{e,t}}{v_{e,g}}\right)=\frac{\phi_{p,f}}{\frac{\sin(\phi-\alpha)}{\sin\phi}(1-n_0)}, \tag{4.15}$$

where $v_{e,t}$ is the total erosion velocity including pure breaching and flow-induced erosion, $u_{ss}=\sqrt{\Delta g d_{50}}$ is Shields velocity for sand grains, and $\phi_{p,f}$ is an empirical non-dimensional pick-up function, which does not account for the bed dilative behavior nor the sloping bed:

$$\phi_{p,f}=\frac{E}{\rho_s u_{ss}}, \tag{4.16}$$

where $E=\rho_s v_{e,f}(1-n_0)$ [kg/(sm^2)] is the sediment pick-up rate perpendicular to the bed surface in which $v_{e,f}$ is the velocity of fluid-induced erosion. The general solution of Equation 4.15 was not reported in *Mastbergen and Van Den Berg* (2003). Instead, two solutions for the two extreme cases $v_{e,t}/v_{e,g}<<1$ and $v_{e,t}/v_{e,g}>>1$ were provided, Eq. (2.23). The first extreme case is never encountered in breaching, while the second extreme case does not hold under lab conditions. Alternatively, Equation 4.15 can be rearranged into a quadratic equation, and after substituting Equation 4.13 into the resulting quadratic equation, the general solution will read:

$$v_{e,t}=u_{ss}\left(\frac{v_{e,g}}{2u_{ss}}+\sqrt{\left(\frac{v_{e,g}}{2u_{ss}}\right)^2+\frac{\phi_{p,f}\Delta k_l f}{u_{ss}\delta n}}\right), \tag{4.17}$$

where f=1 if Eq. 4.13 is used for calculating the erosion rate of pure breaching, whereas $f=v_{e,g,used}/v_{e,g}$ when another value of $v_{e,g,used}$ is used for the erosion rate of pure breaching.

An important feature of breaching-generated turbidity currents is their high particle concentration, the effect of which should be accounted for in the breaching erosion closure model. High near-bed concentrations reduce the flow-induced sediment erosion (*Van Rhee and Talmon*, 2010; *Bisschop*, 2018). The effect of near-bed concentration can be explained by the continuity principle. The sediments are entrained into the flow by the turbulent eddies, and when a turbulent eddy picks up a volume of sediment-water mixture from the bed, the same volume of near-bed mixture has to be conveyed back to the bed. If the near-bed concentration is low, the backflow will carry few sediment particles back to the bed. However, if the near-bed concentration is high, the backflow will carry more sediment particles back to the bed. When the near-bed concentration is almost equal to the bed concentration, nearly no net sediment erosion will take place. Following this argument, *Van Rhee and Talmon* (2010) proposed the reduction factor R:

$$R=(1-n_0-c_b)/(1-n_0) \tag{4.18}$$

to account for the effect of the near-bed concentration c_b. Nevertheless, there is no clear definition of the reference line for the near-bed concentration. Here, we assume that the near-bed concentration is the average value of the particle concentrations within the inner region, where the velocity gradient is positive. The reason behind this choice is to reduce the dependency of the value of the near-bed concentration on the mesh resolution, as higher resolution results in higher concentration of the first cell above the bed. We also show the influence of using the concentration of the first cell above the bed as c_b (instead of the average of the inner region) on the erosional characteristics of the flow (see Subsection 4.5.2).

To close Equation 4.17, we propose a new pick-up function $\phi_{p,f}$, which is modified from the existing function of *Van Rijn* (1984):

$$\phi_{p,f} = 0.00052\, R\, D_*^{0.3} \left(\frac{\theta - f_{cr}\,\theta_{cr}}{f_{cr}\,\theta_{cr}} \right)^{1.5}, \tag{4.19}$$

where D_* is a dimensionless particle diameter defined by $D_* = d_{50} \sqrt[3]{\Delta g/\nu}$, in which ν (m^2/s) is the kinematic viscosity of water, θ is the the Shields parameter, θ_{cr} is the critical Shields parameter for sediment motion and $f_{cr} = 1 + \sin(\alpha - \phi)^2$ is an amplification factor for the critical Shields parameter, which can be used when $\alpha > \phi$. *Lamb et al.* (2008) demonstrated that there is a clear dependency between the critical Shields stress for sediment motion and the bed slope; the critical Shields stress increases with bed slope. Therefore, we account for this increase by the empirical factor f_{cr}.

In the current numerical tool, the computations are done using a non-dimensional pick-up function rather than an erosion velocity. Therefore, Equation 4.17 is recast into the total non-dimensional pick-up function, which reads

$$\phi_{p,t} = \frac{v_{e,t}(1 - n_0)}{u_{ss}}. \tag{4.20}$$

It is worth noting that *Mastbergen and Van Den Berg* (2003) did not account for sediment deposition in their formula, as it was assumed that sedimentation is negligible compared to erosion. However, this assumption may be valid for low near-bed concentrations. In breaching, the near-bed concentrations can be very large. In the model, therefore, we include the sedimentation flux (Equation 4.7), leading to a reduction of the erosion velocity equal to the sedimentation velocity $v_s = (c_b w_s \cos\alpha)/(1 - n_0)$. This means that the erosion velocities resulting from the simulations are the net magnitudes.

4.4. MODEL APPLICATION

To evaluate the applicability and reliability of the present numerical model, the laboratory experiments carried out by *Alhaddad et al.* (2020b) are reproduced numerically and the results are compared. A recapitulation of the experimental set-up of *Alhaddad et al.* (2020b) is provided as follows. The series of laboratory experiments were conducted in a breaching tank: 4 m long, 0.22 m wide and 2 m high. The front wall of the tank was made of glass, whereas the back wall was made of steel. A sand deposit of a steep slope (50-80°) was constructed under water. Owing to the over-steepening of the subaqueous slope, it was essentially unstable and, therefore, it was supported by a confining wall, which should be removed to kick-start the breaching failure and subsequently the turbidity current. The length of the breach face in all experiments did not exceed 1.6 m.

In the breaching tank, a false floor of a mild slope, compared to the breach face, was placed next to the slope toe, where the turbidity current made a turn (see Fig. 4.2). To avoid the reflection of the turbidity current at the end of the downstream region, sand-water mixture was drained constantly during the experiment, while clear water of the same rate was supplied into the tank, so as to guarantee a constant water level.

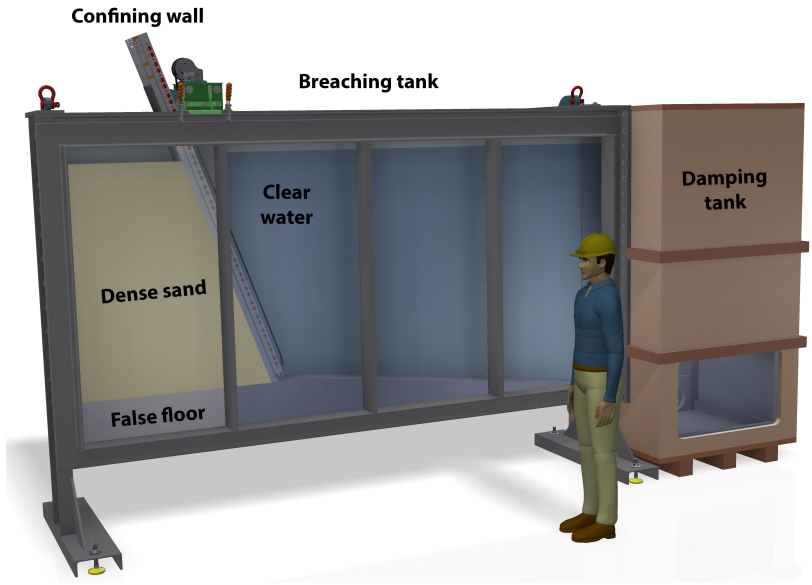

Figure 4.2: 3D sketch of the experimental setup illustrating all components excluding the sedimentation tank.

The work of *Alhaddad et al.* (2020b) did not include measurements for the turbidity current flowing down the toe of the breach face. Therefore, the present simulations consider the breach face and the current running over it, and do not include a slope transition (see Fig. 4.3). The sand used in the experiments (d_{50} = 0.135 mm) was uniformly graded. Therefore, the simulations were run using a uniform particle size fraction of 0.135 mm. Table 4.1 summarizes the sand properties needed for the numerical computations.

Table 4.1: The properties of the sand used in the experiments (*Alhaddad et al.*, 2020b).

d_{50}	n_0	n_l	ϕ	k_l
0.135 mm	0.40	0.51	36°	0.0307 cm/s

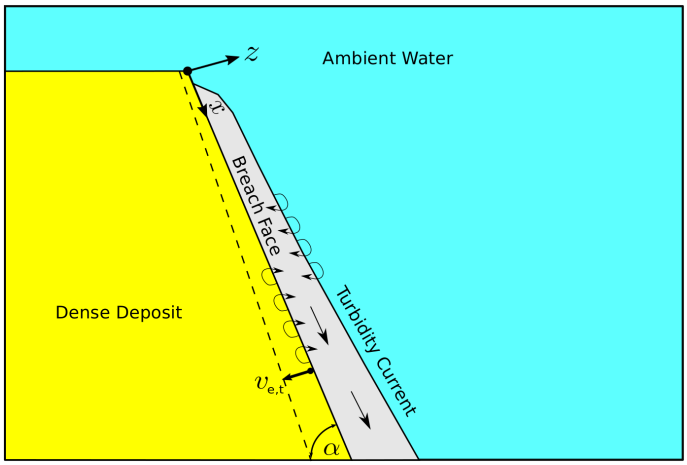

Figure 4.3: Sketch for the case considered in the numerical simulations; $v_{e,t}$ is the total erosion velocity and α is the slope angle.

A rectangular numerical flow domain is used, which follows the sloping bed. See Subsection 4.4.2 for details on the computational domain and grid. The gravity vector is rotated to account for a correct gravity pull on the density current, and sediment settling takes place along the rotated gravity vector. In the lab experiments, the bed erodes and moves backward with a rate equal to the erosion velocity. In the numerical simulations, there is no bed update and the bed does not move backward, but the erosion velocity (~mm/s) is prescribed as an inflowing boundary condition at the bed. At the free surface, a rigid lid free slip condition is prescribed.

The flow is internally generated in the computational domain and no inflow or outflow is prescribed at the lateral, left or right end. This would result in a flow reflection at the right wall after some time, but a sufficiently large domain is chosen, and the simulations are stopped before that happens. The width of the domain is equal to the experimental width and closed lateral boundary conditions are applied with a partial slip boundary condition employing a wall roughness $k_n = 0.2$ mm to account for wall resistance of the current.

4.4.1. MODEL INPUTS

Some inputs are needed to run the simulations such as slope angle, slope length and sand properties. The initial conditions of the numerical runs are summarized in Table 4.2. Upon the start of the numerical simulations, a flow of sediment-water mixture equivalent to the corresponding erosion rate of pure breaching is imposed at the first computational grid cell above the bed. Thereupon, the turbidity current starts developing along the breach face.

Table 4.2: Initial conditions of the numerical runs; f_{cr} is the amplification factor for the critical Shields parameter and n_0 is the *in situ* porosity.

Run #	Slope angle (°)	Erosion rate of pure breaching (mm/s)	f_{cr}	n_0
1	50	0.28^a	1.06	0.40
2	54	0.37^b	1.10	0.40
3	64	0.58^a	1.22	0.40
4	67	0.82^b	1.27	0.40
5	70	0.92^b	1.31	0.40
6	77	1.20^b	1.43	0.40
7	81	1.35^a	1.50	0.40
8	67	1.21^b	1.27	0.44

^{a} Experimental data, ^{b} calculated using Equation 4.14 (not available in corresponding experiments).

4.4.2. COMPUTATIONAL GRID

The computational geometry used in the simulations is demonstrated in Fig. 4.4. The domain height is 25 cm, deep enough to avoid effects of the overflow above the turbidity current, while the domain width is 22 cm, equal to the width of the experimental setup. As the purpose of the numerical simulations is to reproduce the current running along the breach face (1.5 m long), it was decided to have a total domain length of 3.5 m. The domain is divided into two zones. The first zone (0 to 1.8 m) corresponds to the breach face over which the turbidity current propagates. The second zone (1.8 m to 3.5 m) functions as a sediment sink, where the sand particles settle out, decelerating the flow and preventing the reflection of the turbidity current upstream. The numerical data after x = 1.5 m are not considered, since they are influenced by the sediment sink.

The computational mesh consists of a total number of about 46 million cells. To reduce the computational time, grid clustering was used in x-direction; a width of 2 mm was used for the cells in the first 1.5 m, while the width of the remaining cells was gradually increased with a growth rate of 1.04 with an upper limit of 5 cm. The cell dimensions in the y and z directions were kept constant with a value of 2 mm and 0.5 mm, respectively (leading to a maximum $\Delta z^+ = 15$ for the first velocity point located at $\frac{1}{2}\Delta z$). The average computational time of the runs presented in this study was about 4 days.

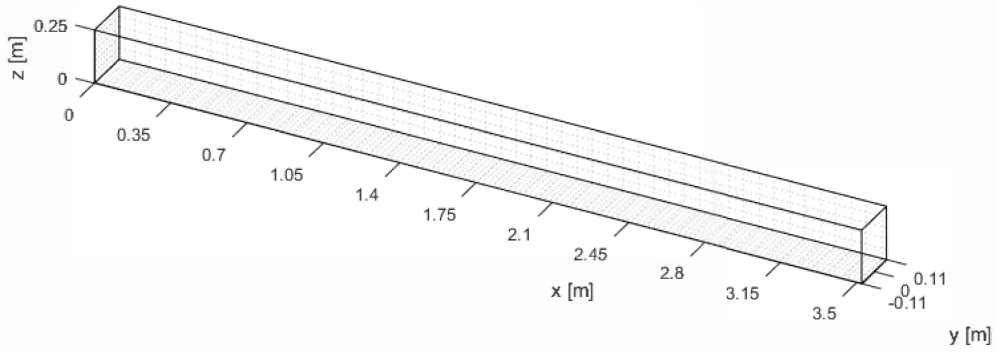

Figure 4.4: Geometry used in all numerical simulations: Δx = 2 mm - 5 cm, Δy = 2 mm and Δz = 0.5 mm; the current travels from left to right and sand particles are removed from x = 1.8 m onward.

4.5. MODEL VALIDATION

As noted earlier, the WALE sub-grid-scale model is used in this study. To ensure that the numerical results are independent of the chosen sub-grid-scale model, an extra simulation has been run using the dynamic Smagorinsky sub-grid-scale model (which is more computationally demanding) and the simulation results were compared with those obtained with the WALE sub-grid-scale model. Indeed, no differences have been observed between the results.

In this section, specific quantitative time averaged numerical results are compared with the corresponding experimental results to test the validity and reliability of the proposed numerical model. However, some instantaneous flow results are first presented to illustrate the type of flow we are dealing with.

4.5.1. INSTANTANEOUS FLOW RESULTS

In general, turbidity currents are known to be highly turbulent and breaching-generated turbidity currents are not an exception. Figure 4.5 clearly shows the transition of the flow from laminar to turbulent at about x = 20 cm for the 64° slope, which is in line with visual observations during the experiment. The top plot demonstrates the 3D highly turbulent behavior of the turbidity current whilst the middle plot illustrates the highly turbulent instantaneous concentration and velocity distribution over the vertical. The latter also shows that the inner region is very thin compared to the total layer thickness and that relatively high velocities can be found in zones with relatively low sediment concentrations between $0.01 < c < 0.1$. In the remainder of this section, time averaged model results are presented to allow for the comparison with the experimental results.

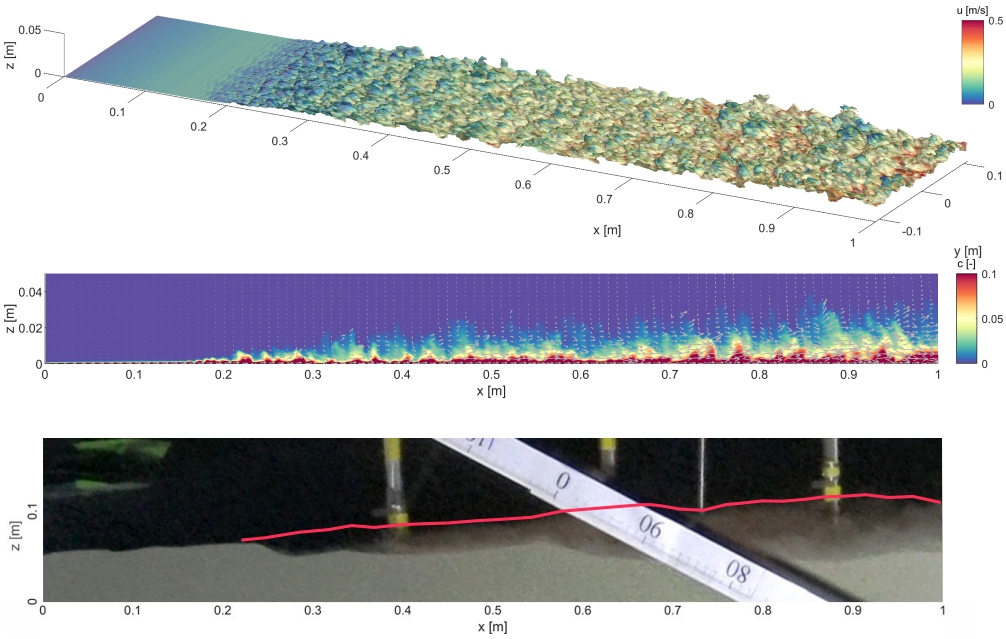

Figure 4.5: An instantaneous 3D view of the isosurface c = 0.01 at time=8 seconds (Run 3); colors indicate the magnitude of the streamwise velocity (**top**). An instantaneous 2D vertical slice at y = 0 at time = 8 seconds (Run 3); colors indicate the magnitude of the sediment concentration c and vectors indicate the magnitude and direction of the streamwise and bed-normal velocities in this plane (**middle**). An instantaneous, experimental side view of the spatial development of the flow over a 64° breach face (*Alhaddad et al.*, 2020b); the flow propagates from left to right and the red line corresponds to the visual upper boundary of the flow (**bottom**).

4.5.2. SEDIMENT EROSION

To evaluate the proposed breaching erosion closure model and the morphodynamic response associated with the turbidity currents, simulation results are compared against the corresponding experimental data (see Fig. 4.6). For each of the numerical runs, the constructed erosion velocities are the average magnitudes over a 3-second time span and a lateral distance of the first 10% of the domain width (2.2 cm). This is because the erosion velocities reported in *Alhaddad et al.* (2020b) were computed from the video recordings filmed through the glass wall.

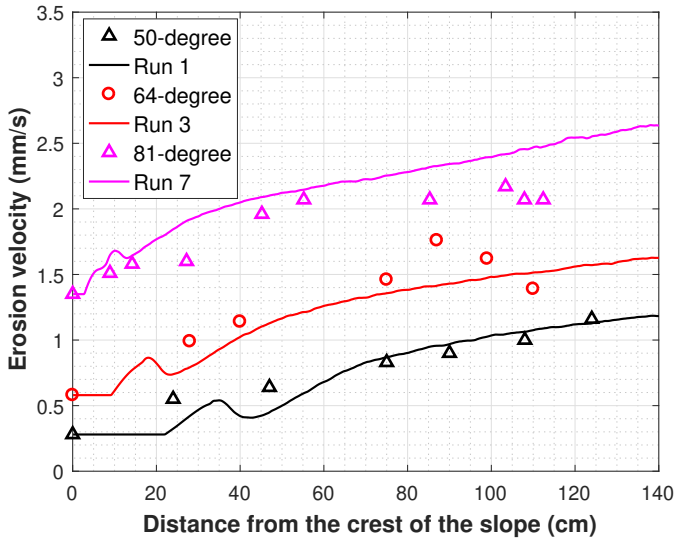

Figure 4.6: Comparison of erosion velocities resulted from numerical simulations (solid lines) and lab experiments.

As it can be seen, the numerically predicted erosion velocities coincide very well with the experimental data. The prediction accuracy of the erosion closure model is considered high (mean absolute error = 11%) compared to what is generally feasible in the field of sediment transport. The erosion lines in Fig. 4.6 begin with a horizontal segment, where the turbidity current is not yet sufficiently energetic to erode sediment from the breach face. Shortly after that, the turbidity current ignites and increasingly erodes sediments from the breach face.

The experimental data suggests a transition in the erosion rate after a certain point. For example, in the case of the 81° breach face, the observed erosion velocity is found to be almost constant in the streamwise distance 55-110 cm. It could be that the *in situ* porosity n_0 was not uniform all over the breach face (see Subsection 4.6.6 for the effect of n_0). Another hypothesis is that the current was in the by-pass mode (the current maintains the sediment load while propagating), but that is not captured in the numerical model. This may be attributed to the reference line of the near-bed concentration, which should be defined based on the dimensions of the turbulent eddies transporting the sand grains from the turbidity current back to the breach face. The size of those eddies was not considered in *Alhaddad et al.* (2020b) as that requires higher resolved experimental data.
To elaborate on this hypothesis, we show in Fig. 4.7 two different definitions of the near-bed concentration c_b and the corresponding reduction factor R (Eq. 4.18); c_{b1} is the computed concentration within the first cell above the bed, while c_{b2} is the average concentration in the inner region. The value of c_{b2} tends to become constant downslope and consequently the reduction factor R_2 also remains constant. In contrast, c_{b1} rapidly increases in the downstream direction and hence the reduction factor R_1 rapidly decreases. This implies that at some point along the breach face, the increase in shear stress will be balanced by the increase of the near-bed concentration, transforming the flow from the self-acceleration mode to the by-pass mode. In conclusion, the definition of the near-bed concentration

influences the computed erosion rates and, consequently, might influence the flow mode.

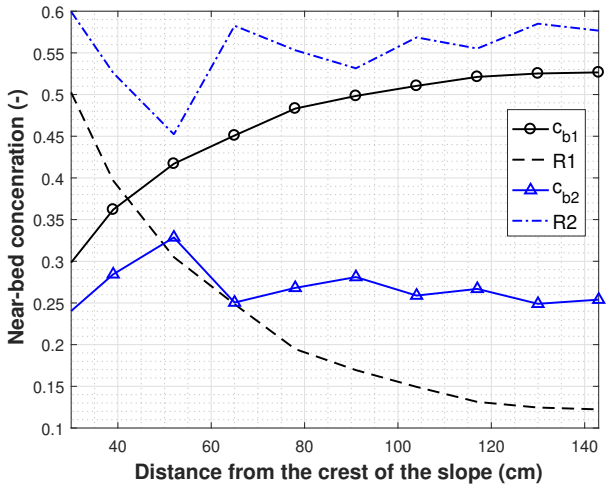

Figure 4.7: Two definitions of near bed concentration c_b and the corresponding reduction factors R; c_{b1} is the concentration of the first cell above the bed, while c_{b2} is the average concentration in the inner region.

4.5.3. FLOW SPATIAL EVOLUTION

The characterizing layer thicknesses h and depth-averaged velocities U for Run 1, Run 3 and Run 5 are computed from the numerical results and compared with corresponding magnitudes derived from the laboratory experiments. These flow characteristics, h and U, are calculated using the following relationships (*Parker et al.*, 1986, 1987; *Garcia and Parker*, 1993):

$$Uh = \int_0^{z_\infty} u\,dz, \tag{4.21}$$

$$U^2 h = \int_0^{z_\infty} u^2\,dz, \tag{4.22}$$

where u is locally averaged streamwise flow velocity, z is upward-normal distance from the bed and z_∞ is the height at which the local velocity u is zero.

In these runs, the densimetric Froude number is greater than one, indicating that the flow is supercritical, which agrees with the experimental results. The densimetric Froude number is calculated using the following relationship (*Komar*, 1971):

$$Fr_d = \frac{U}{\sqrt{\Delta g C h}}, \tag{4.23}$$

where C denotes the layer-averaged, volume concentration of sediment defined as:

$$C = \frac{\int_0^{z_\infty} c\,u\,dz}{\int_0^{z_\infty} u\,dz}, \tag{4.24}$$

in which c is local concentration of suspended sediment.

In addition to the characteristics h and U, the layer-peak velocities u_{max} are also constructed in Fig 4.8. It can be seen that the model predictions of the spatial evolution of the flow agree qualitatively with the experimental data. However, the model fails to accurately predict the layer thickness (mean absolute error = 46%); it is underestimated. We speculate that this underestimation partly relates to the missing feedback from the sand particles to the flow, leading to less momentum exchange and mixing. This underestimation could be one of the reasons for the deviation between the numerically predicted layer-averaged velocities and the experimental ones (mean absolute error = 18%); the predicted flow velocities for the 64° and 70° breach faces are somewhat lower than the measured ones. Another important reason for this difference is that the coupled erosion closure model was calibrated based on the erosion rates measured at the glass wall of the experimental tank. However, *Alhaddad et al.* (2020b) found the erosion to be the highest in the middle of the tank width, where the velocity measurements were obtained, declining towards the side walls. This implies that somewhat more sediment should be entrained from the breach face to the turbidity current to gain higher velocities.

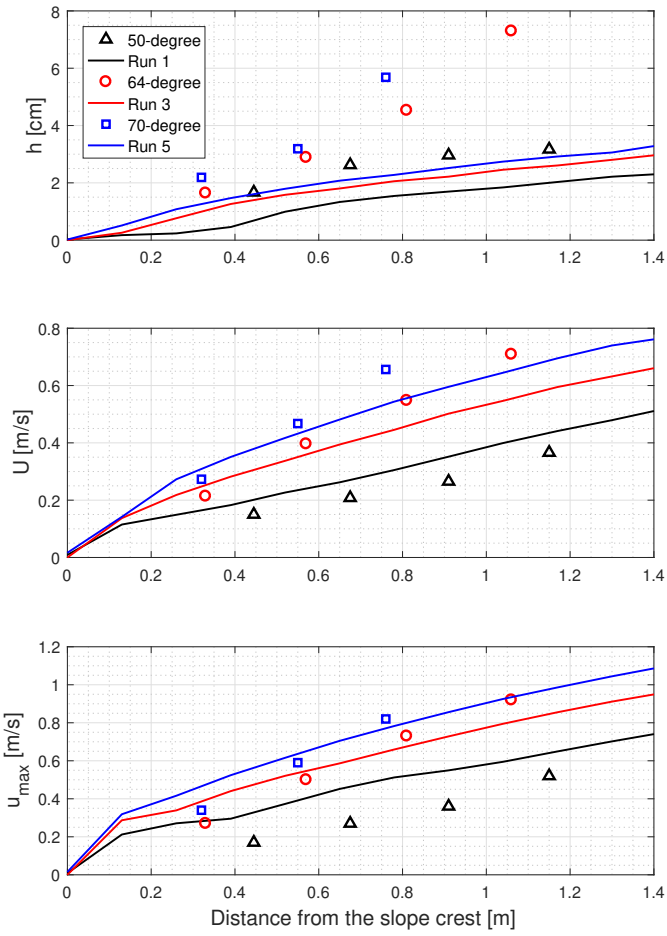

Figure 4.8: Comparison of spatial evolution of turbidity currents propagating over 50°, 64°, and 70° slopes: layer thickness development (**top**), layer-averaged velocity (**middle**), and layer-peak velocity $U_{\max}$ (**bottom**).

4.5.4. VELOCITY PROFILES

The non-dimensional bed-normal profiles of the streamwise velocities for Run 3 and Run 5 are constructed and compared with the corresponding dimensionless profiles derived from the laboratory experiments. In these numerical runs, the profiles are taken at the same distances from the breach crest as in the experiments. The streamwise local velocities are normalized with the depth-averaged velocity U, whilst the local bed-normal distances are normalized with the characterizing layer thickness h.

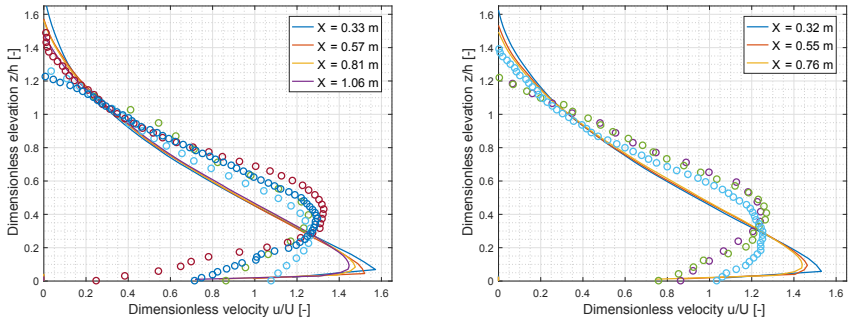

(a) (b)

Figure 4.9: Comparison of numerical dimensionless velocity profiles (solid lines) versus experimental data (circles): (**a**) 64° breach face; (**b**) 70° breach face.

Reasonable overall agreement is found between simulation and experimental results in the bed-normal structure (see Fig. 4.9), but simulation predictions deviate from experiments in the location of the velocity maximum u_{max}. The latter is numerically predicted to be closer to the bed than measured in the experiments. This could be partially attributed to the underestimation of the layer thicknesses by the model. Another possible reason for the differences are the difficulties and uncertainties in pinpointing the bed position in the laboratory experiments, as stated in the work of *Alhaddad et al.* (2020b). The numerical results demonstrate that the velocity profiles are self-similar, as can be inferred from the experimental results (*Alhaddad et al.*, 2020b).

4.5.5. BED-NORMAL DENSITY DISTRIBUTION

We examine here the capability of the model to capture the internal density distribution of the flow through comparing concentration profiles measured with Conductivity-type Concentration Meter (CCM) (single-point device) along different inclinations versus numerical results. It can be seen from Fig. 4.10 that the time-averaged concentration profiles predicted by the model fall within the scatter range of the corresponding profiles resulted from the laboratory experiments. Also the very high near-bed concentrations in the order of c = 0.4-0.52 are captured in the numerical model. This indicates that the numerical model can adequately predict the bed-normal density distribution of the considered turbidity current.

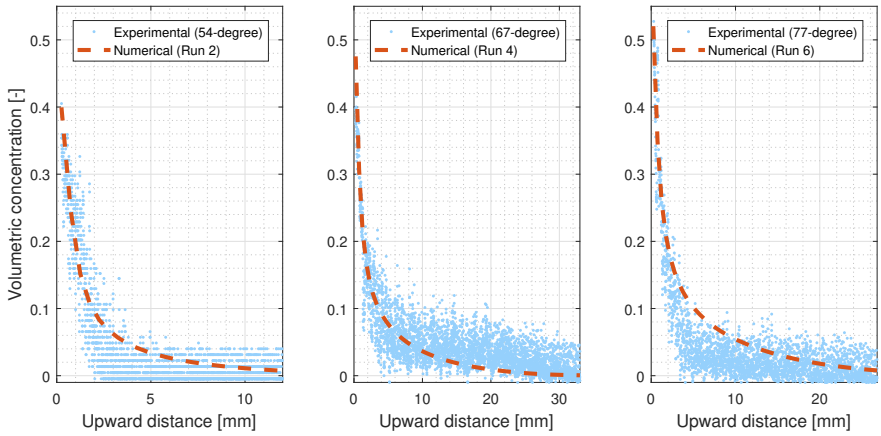

Figure 4.10: Comparison of time-averaged, upward, normal concentration profiles predicted by the present model against the corresponding experimental results; 54° (**left**), 67° (**middle**), and 77° breach face (**right**).

4.5.6. CONCLUSION ON COMPARISON OF NUMERICAL SIMULATIONS AND EXPERIMENTS

In view of the presented systematic comparison between the numerical and experimental results, it can be concluded that the numerical model gives fairly reasonable predictions of the flow characteristics and the associated morphodynamic response, except for the layer thickness. In the next section, therefore, we investigate further flow characteristics, which were not possible to analyse through the experimental data.

4.6. FURTHER ANALYSIS OF NUMERICAL RESULTS

In Section 4.5 we showed that the model was good at simulating the experimental observations. This gives us confidence to closely investigate the flow and turbulence structure, to determine some characterising parameters and to analyse the sensitivity of the numerical results to some initial conditions. This will be the scope of this section.

4.6.1. LAYER-AVERAGED CONCENTRATION

Fig. 4.11 depicts the spatial development of the layer-averaged concentration C (Equation 4.24) for three slope angles. Clearly, steeper slopes result in a higher C owing to the higher sediment erosion. The results show that C increases in the downstream direction, in the same manner as the layer-averaged velocity U (see Fig. 4.8). This supports the conclusion drawn by *Alhaddad et al.* (2020b) that breaching-generated turbidity currents are self-accelerating. According to *Sequeiros et al.* (2018), self-accelerating flow is characterised by the downstream increase of flow velocity, which is caused by downstream increase in suspended sediment concentration.

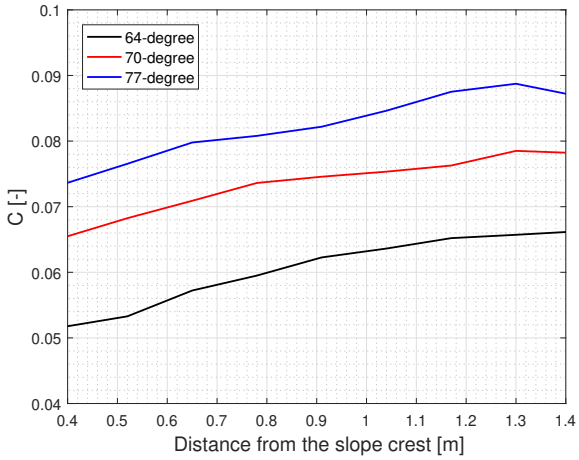

Figure 4.11: Spatial development of the layer-averaged concentration C along the breach face.

4.6.2. SPATIAL EVOLUTION OF BED-NORMAL DENSITY DISTRIBUTION

The bed-normal profiles of the sediment concentrations for Run 3 and Run 6 are depicted in Fig. 4.12. While the turbidity current further travels downslope, the near-bed concentration increases. Moreover, steeper slopes result in higher near-bed concentrations, which can be attributed to the higher erosion rates caused by a larger gravity force and more erosive turbidity currents.

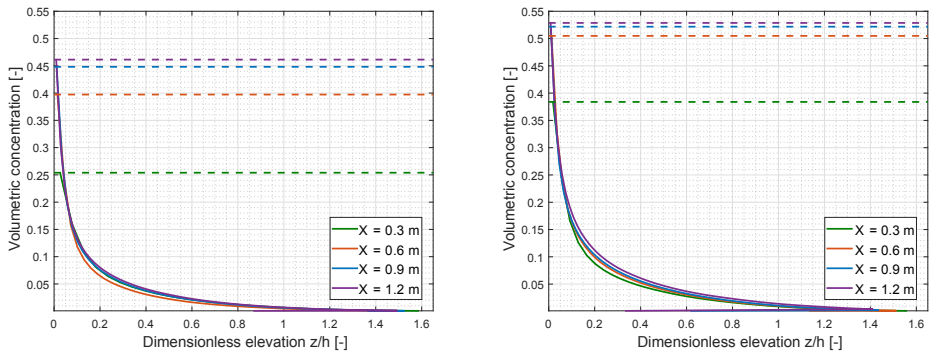

Figure 4.12: Composite plot of numerical concentration profiles spaced by a distance of 0.3 m: (**a**) 64° breach face (Run 3); (**b**) 77° breach face (Run 6); horizontal dashed lines refer to the concentration maximum.

4.6.3. REYNOLDS STRESSES

The Reynolds stress distribution corresponds to the velocity gradient within the flow body as maximum stresses occur where the gradient is largest. The normal Reynolds stresses can be obtained from the turbulent fluctuations of downstream u' and bed-normal velocity w' as

follows:

$$\tau_r = -\rho\overline{u'w'}. \tag{4.25}$$

The Reynolds stresses are calculated using the turbulent velocity components averaged over a 3-second time span. For three different slopes at $x = 1$ m, Reynolds stresses are normalized by ρU^2 and their distribution is shown in Fig. 4.13a. The Reynolds stress increases significantly near the breach face, reaching the largest positive Reynolds stress at $z/h \sim 0.025$, where the bottom boundary layer ends. Around and below the velocity maximum, $z/h = 0.045$-0.085, Reynolds stresses are close to zero. Further upwards, in the outer region of the flow, where the velocity gradient is negative, the Reynolds stress becomes negative, reaching the largest negative Reynolds stress at $z/h \sim 0.45$. This elevation has the largest negative velocity gradient. Above this elevation, the Reynolds stress decreases towards nearly zero at the upper boundary of the flow. It is found that the Reynolds stress takes a self-similar shape.

Fig. 4.13c illustrates the spatial development of Reynolds stress along 64° and 77° breach faces. Owing to the acceleration of the flow downslope, the flow becomes more turbulent, leading to higher Reynolds stresses in the downstream direction. These stresses, as can be seen in Fig. 4.13c, are higher for steeper breach faces, as these result in higher flow velocities.

4.6.4. TURBULENT KINETIC ENERGY

Profiles of turbulent kinetic energy (TKE) are constructed to analyse the bed-normal distribution of the TKE within the flow. The total TKE is calculated using the turbulent velocity components averaged over a 3-second time span as follows

$$TKE = \frac{1}{2}\rho(\overline{u'^2} + \overline{v'^2} + \overline{w'^2}), \tag{4.26}$$

where u' is the streamwise component, v' is the across-stream component and w' is bed-normal component. Numerical TKE normalized by ρU^2 is plotted in Fig. 4.14a for three different slope angles at $x = 1$ m. The TKE profiles show a significant increase of TKE in the bottom boundary layer $z/h \sim 0$-0.025 and then a decrease until $z/h \sim 0.045$, a little below the velocity maximum. Above the elevation of the velocity maximum, the TKE increases again, reaching the largest TKE at $z/h \sim 0.45$, coinciding with the largest negative velocity gradient and largest Reynolds stress. Above this elevation, TKE tends to decrease towards the upper boundary of the flow. The results suggest that TKE takes a self-similar shape.

Fig. 4.14b illustrates the spatial development of TKE along 64° and 77° breach faces. In a similar way to the Reynolds stresses, the TKE increases downslope and is higher for steeper slopes.

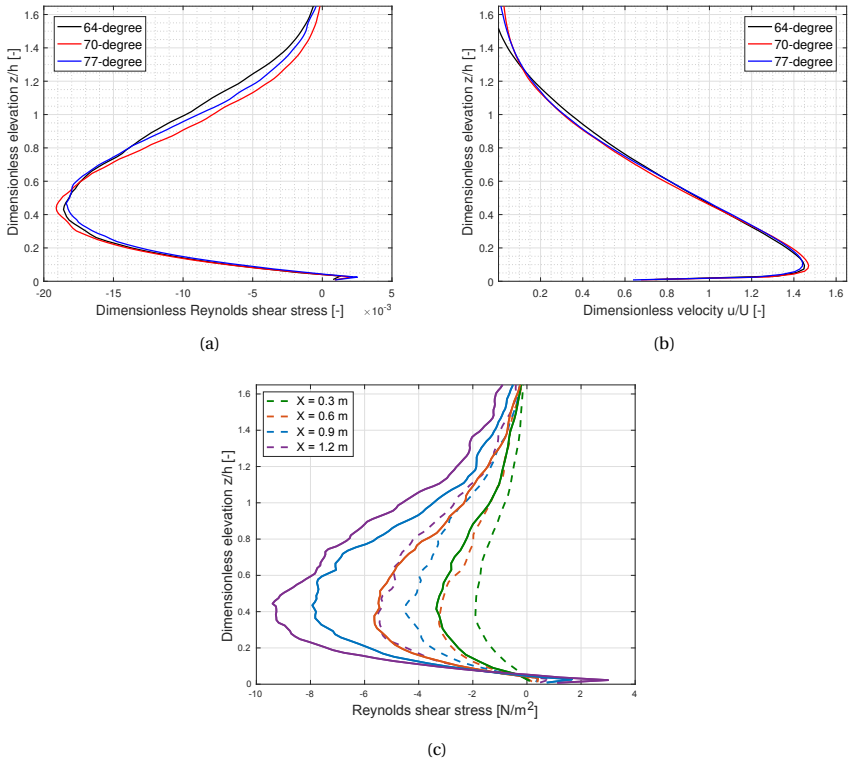

(a) (b)

(c)

Figure 4.13: (**a**) Composite plot of normalized Reynolds stresses profiles at $x = 1$ m for different slope angles; (**b**) Composite plot of dimensionless velocity profiles at $x = 1$ m for different slope angles; (**c**) Composite plot of Reynolds stresses profiles spaced by a distance of 0.3 m: dashed lines correspond to 64° breach face and solid lines correspond to 77° breach face.

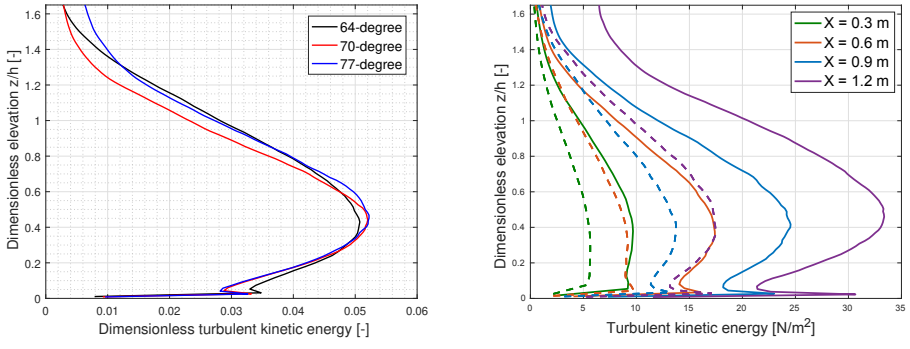

(a) (b)

Figure 4.14: (**a**) Composite plot of normalized TKE profiles at $x = 1$ m for different slope angles; (**b**) Composite plot of TKE profiles spaced by a distance of 0.3 m: dashed lines correspond to 64° breach face and solid lines correspond to 77° breach face.

4.6.5. BED SHEAR STRESS AND BED FRICTION COEFFICIENT

The bed shear stress τ_b determines the erosive power of the flow and can be expressed in terms of a bed friction coefficient C_f, which relates the bed shear velocity u_* to the layer-averaged velocity U as follows

$$C_f = \frac{u_*^2}{U^2} \tag{4.27}$$

This relation is commonly used in depth-averaged models. These are more computationally efficient and can be used to make some preliminary computations. In this study, the value of u_* is calculated using Equation 4.11. The average value of the C_f is calculated here from the numerical results.

The calculated values of C_f show that the bed friction coefficient is not a constant parameter (Fig. 4.15); it decreases downslope. This is because the thickness of the current increases along the streamwise direction, resulting in an increased bulk Reynolds number and, consequently, a decreased drag coefficient (*Salinas et al.*, 2019). The results also show that steeper slopes lead to a lower bed friction coefficient. For the considered slope angles and traveling distance, C_f ranges from 0.028 to 0.006 with an average value of 0.011. This is consistent with the range of values reported in the literature (e.g. *Parker et al.* (1987)).

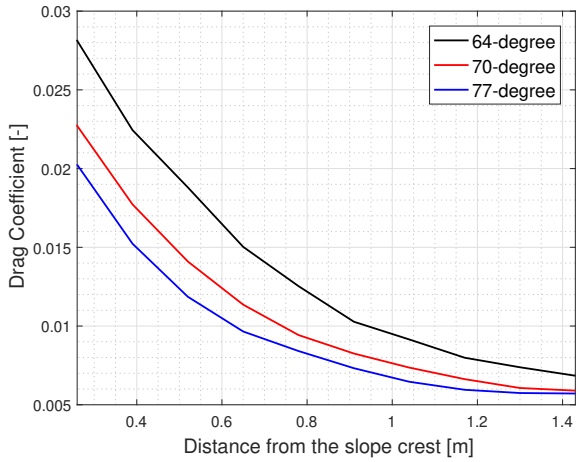

Figure 4.15: Spatial change of bed friction coefficient along the breach face.

4.6.6. INFLUENCE OF *in situ* POROSITY

The experiments of *Alhaddad et al.* (2020b) were all conducted using a constant sand *in situ* porosity $n_0 = 0.4$. To investigate the effect of n_0 on the flow and erosion velocity, an additional numerical simulation for a 67° breach face was run using $n_0 = 0.44$, which corresponds to a sand relative density of 68%. A comparison between the numerical results for $n_0 = 0.4$ (Run 4) and $n_0 = 0.44$ (Run 8) is shown in Fig. 4.16. It can be seen from Fig. 4.16a that higher n_0 results in a higher erosion rate of pure breaching and hence higher total erosion velocities downslope; the average increase in erosion, in the considered case, is significant (47%). Higher n_0 leads to a lower hydraulic gradient (which acts as a stabilizing force) during

shearing, increasing the erosion velocity. As a result, the flow becomes denser and runs faster downslope, as depicted in Fig. 4.16b. The difference of the layer-averaged velocities between the two runs is magnified downstream.

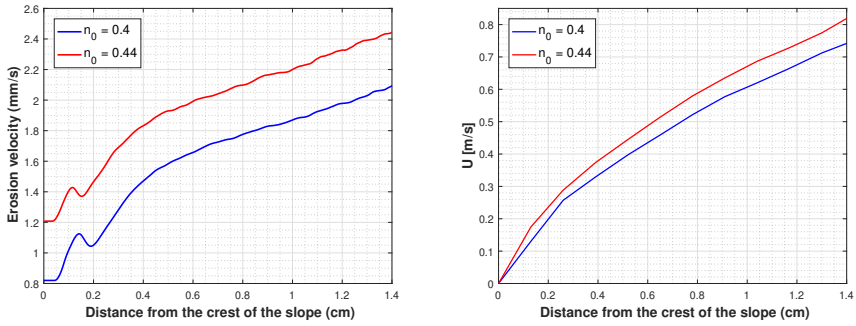

(a) (b)

Figure 4.16: Comparison between numerical results for 67° breach face using different initial porosities n_0 (**a**) erosion velocity; (**b**) layer-averaged velocity.

4.7. CONCLUSION

We utilize a 3D numerical model to conduct large eddy simulations of turbidity currents generated during breaching flow slides. The qualitative and quantitative comparison between experimental and simulation results indicates that the proposed numerical tool can reasonably reproduce several substantial aspects of the flow, such as bed-normal density distribution, and spatial development down the breach face. A limitation of the model is that it underestimates the thickness of the current. Considering the special conditions of breaching, a new breaching erosion closure model is proposed and verified through published experimental data. Good agreement is observed between the experimental and numerically predicted erosion rates. The numerical results confirm the self-accelerating behavior of breaching-generated turbidity currents. Both Reynolds stresses and TKE decrease sharply below their maximum in the bottom boundary layer. In addition, the numerical results reveal that breaching-generated turbidity currents exhibit a self-similar behavior; velocity, concentration, Reynolds stress, and TKE profiles take a self-similar shape. Based on a sensitivity analysis, sand erosion during breaching is found to be susceptible to the *in situ* porosity; the lower the *in situ* porosity, the higher the sand resistance to erosion. If the present numerical model is extended to account for the morphological changes of the breach face and the occurrence of surficial slides, it would serve as a good tool to predict the breaching evolution and stability.

5

General Discussion

In breaching flow slides, when the sand particles peel off from the steep underwater slope (or 'breach face'), they drag the ambient water along, generating downward, turbulent turbidity currents. These currents actively travel over the breach face and directly interact with it in a positive feedback loop. This study aimed at developing a solid understanding of this interaction, so as to improve the predictability of the evolution of the slope failure. This is a critical asset to avoid the risk associated with breaching flow slides and to develop effective mitigation strategies. In an integral way, the results from the analyses presented in Chapters 2-4 will be discussed in this chapter. This aims at reflecting on the conducted research and at indicating the potential implications of the research findings.

The current knowledge of breaching flow slides has been systematically reviewed and analyzed in Chapter 2. The objective was to provide a better insight into the underlying processes and to identify the relevant knowledge gaps, thereby posing open questions and defining key directions for future research. The physical processes governing breaching flow slides from the triggering mechanism until the final deposition of sediment were explained and discussed. Among other knowledge gaps, it was shown that our current understanding of the triggering mechanisms is limited. For instance, some breaching events are still being observed at Amity Point in Queensland, Australia and the trigger of these events is not known (*Mastbergen et al.*, 2019). In this respect, further research is required to understand how breaching is initiated. A key finding of Chapter 2 is that the breaching erosion closure models used in the existing body of research yield considerably different predictions of erosion. Crucially, this results in different predictions of the hydrodynamics of the ensuing turbidity currents, owing to the two-way coupled processes of sediment breaching and turbidity currents. An assessment of the performance of existing erosion closure models was precluded by the absence of flow measurements and the corresponding erosion. To tackle this impediment and to gain a deeper insight into the coupling between the evolution of the breach face and the turbidity current, breaching lab experiments were performed and detailed in Chapter 3.

A series of large-scale experiments was carried out, obtaining direct measurements of breaching-generated turbidity currents and the associated sediment transport. The measurements demonstrated the development of the flow and visualised the structure of its velocity and sediment concentration. Similar to other types of gravity currents, the wall-normal velocity structure of breaching-generated turbidity currents exhibits two distinct regions: an inner region showing a positive velocity gradient, and an outer region thicker than the former region and showing a negative velocity gradient. Owing to the dynamic nature of the breach face and the high sediment concentration directly above it, it was not possible to infer whether or not the flow velocity at the breach face was zero, leaving it as an open question. Analysis of the flow velocities suggested that the velocity profiles of these currents take a self-similar shape, which was confirmed by the numerical results presented in Chapter 4. The sediment concentration profiles were found to decay exponentially away from the breach face until the upper interface of the flow. Dense basal layers with high near-bed concentrations up to 0.5 by volume were observed, demonstrating the complexity of the dynamics of the bottom boundary layer, where the particle-particle and particle-fluid interactions affect the momentum and mass exchanges between the turbidity current and the breach face. Additionally, high near-bed concentrations dampen the turbulence of the bottom boundary layer and may even completely suppress it; the base of turbidity currents has a certain particle suspension capacity beyond which it cannot contain more sediment in

suspension, as that causes complete extinction of boundary layer turbulence (*Eggenhuisen et al.*, 2017). Moreover, high near-bed concentrations retard the pick-up rate of sediment by the flow (*Van Rhee and Talmon*, 2010; *Bisschop*, 2018).

Through the experimental results, it was confirmed that breaching-generated turbidity currents are self-accelerating. They induce an additional shear stress on the breach face, thereby picking up more sediment, which makes the turbidity current denser. As a result, the current expedites downslope, boosting its erosive capacity and leading to higher erosion rates in the downstream direction. This implies that sediment entrainment and acceleration of the turbidity current are coupled in a positive feedback loop. Nevertheless, the experimental data showed that there is a transition down the slope, where the erosion rate begins to decrease, or becomes constant. The process behind this transition was not investigated in Chapter 3, but it is hypothesized that the transition may relate to turbulence damping. The suspended sediments enhance turbulence energy production, thereby promoting the basal shear stress and enabling resuspension of sediment. However, the increased suspended sediment stratification also dampens turbulence, implying that the self-accelerating process may continue until the turbulence production is balanced by turbulence damping. It was also hypothesized, in Chapter 4, that this transition may relate to the increase of near-bed concentration downstream, which leads to larger amounts of sediment transported back to the breach face by turbulent eddies. The self-accelerating behaviour of breaching-generated turbidity currents implies that their velocity may hugely increase in case of long breach faces, causing severe damage to nearby environments and infrastructure. While the current self-accelerates in the stream-wise direction, it may become capable of excavating a submarine canyon as earlier indicated by *Mastbergen and Van Den Berg* (2003). Another implication is that the breaching phenomenon forms a potential trigger for sustained, powerful turbidity currents encountered in deep water.

Owing to the variation of the erosion rate along the breach face (the lower part erodes quicker than the upper part), a sediment overhang develops and eventually collapses and slides downslope under the influence of gravity. Such a surficial slide was always found to occur at the uppermost part of the breach face, considerably enhancing local erosion and fueling the turbidity current. Directly after the occurrence of a surficial slide, the uppermost part of the breach face relaxes towards a milder slope. Monitoring the temporal evolution of the bed morphology showed that the breach face keeps steepening over time until it becomes vertical. At this stage, sand production is at the highest in case of sand mining by stationary suction dredgers.

During the lab experiments, it has been clearly observed that not only is the erosion rate non-uniform along the breach face, but it is also non-uniform across the breach face. The erosion was observed to be the highest almost in the middle of the breach face across the tank, declining towards the tank walls. In other words, the breach face was inwardly curved in the erosion direction. It is speculated that this erosion behaviour is not only a result of the tank wall effects, but also an intrinsic property of the breaching problem. The final morphology of breaching events documented in the literature also takes a concave shape (e.g., *Mastbergen et al.*, 2019). This implies that the three-dimensionality of the sand and turbidity current plays a vital role in breaching flow slides.

In this study, the term 'pure breaching' was adopted to describe the grain-by-grain failure induced by gravity (no flow-induced erosion). Considering the physical theory behind the expression of the wall velocity, this expression represents the process of pure breaching.

This expression was evaluated, and good agreement was found between the expression and experimental results. However, the expression tends to overestimate the erosion rate of pure breaching. This fact should be taken into account when breaching erosion closure models are developed based on the expression of wall velocity. To improve this expression, an empirical correction factor was suggested in Chapter 4. Nonetheless, direct measurements of different grain sizes are needed to examine the general applicability of this correction factor.

A key finding of Chapter 3 is that breaching evolution is mainly governed by the accompanying turbidity currents rather than gravity. In the first place, breaching is induced by gravity due to the over-steepening of the slope caused by a certain trigger. Thereupon, the turbidity current is generated and starts dominating the failure evolution until the end of the breaching event. This current rapidly accelerates downslope and becomes capable of eroding sediments more than the sediments peeling off from the breach face under the influence of gravity alone. Besides, as discussed earlier in this chapter, this current causes the occurrence of surficial slides, promoting local erosion and thereby strengthening itself. Additionally, the turbidity current carries sediments and moves away down the toe of the breach face. The fate of these sediments is highly governed by the turbulence of the turbidity currents. Whether the breaching process is stable or unstable is also mainly controlled by the influence of the turbidity currents (*Van Rhee*, 2015). If the turbidity current is depositional at the downstream region, the height of the breach face will decrease over time until it vanishes. In contrast, if the turbidity current is erosive at the downstream region, the height of the breach face will increase over time, resulting in unstable breaching. This dominant influence of turbidity currents clearly implies that successful numerical simulations of breaching flow slides must be capable of reasonably reproducing the dynamics of turbidity currents and their sediment transport.

The dynamic nature of the breach face, together with the structure and nature of the breaching-generated turbidity currents, makes breaching experiments very difficult to perform. Therefore, measurements of turbulence quantities of the flow were not obtained in this study. This hampers the estimate of the bed shear stress induced by the flow and hence the prediction of erosion along the breach face. The latter is necessary to assess or improve existing breaching erosion closure models. To this end, high-resolution turbulence-resolving simulations were conducted, which was the primary topic of Chapter 4.

Owing to the feedback between the suspended sediments and flow turbulence, the dynamics of turbidity currents are highly complicated. As a result, modelling turbidity currents by depth-averaged equations, as in the the model used in Chapter 2, is a greatly simplified approach (*Kneller and Buckee*, 2000), requiring several empirical closure relations, such as the near-bed concentration, water entrainment at the upper boundary and bed friction coefficient. These empirical relations reduce the accuracy of the simulation results. Therefore, a 3D large-eddy-resolving numerical model was instead used in Chapter 4, providing deeper insights into the flow structure and hydrodynamics of breaching-generated turbidity currents. In this model, the mixture approach was used, combined with the concept of drift velocity. The proposed numerical tool can realistically predict several substantial aspects of the flow, such as vertical density distribution, and spatial development down the breach face. A shortcoming of the model is that it underestimates the thickness of the current and in particular the thickness of the inner region, and the reason behind that remains unexplored. Nevertheless, it is speculated that this underestimation partly relates to the missing feedback from the sand particles to the flow, leading to less momentum exchange and mixing. The

thickness underestimation could also be attributed to the missing interaction between the particles. In the inner region, the particle concentration is much higher than the Bagnold limit (*Bagnold*, 1962), where particle-particle interactions play a role in supporting the particles; energy exchanged by particle collisions aid in keeping them suspended (*Mulder and Alexander*, 2001). The numerical results showed that the layer-averaged concentration and the layer-averaged velocity increase in the downstream direction of the slope, confirming the self-accelerating nature of breaching-generated turbidity currents. The numerical results also indicate that these currents evolve in a self-similar manner. This implies that self-similar solutions to the hydrodynamic equations governing the turbidity current could be derived, thereby greatly simplifying the mathematical problem of solving the flow equations. In addition, the self-similarity allows the scaling of these current.

Evidently, the erosion during breaching is a highly complex process, requiring an understanding of the relevant soil and fluid mechanics. A good breaching erosion closure model must account for all the factors playing a role in the erosion process. These factors can be summarized as follows: the particle-by-particle erosion induced by gravity (pure breaching), the dilatancy-retarded erosion caused by the high-concentration turbidity currents, and the surficial slides. Excluding the latter, the erosion closure model of *Mastbergen and Van Den Berg* (2003) was adopted, extended and validated against the direct measurements of turbidity currents and the associated sediment erosion presented in Chapter 3. Compared to the acceptable accuracy in the field of sediment transport, the prediction accuracy of the suggested erosion closure model is considered high. A sensitivity analysis showed that breaching erosion is susceptible to the *in situ* porosity; lower *in situ* porosity leads to a higher inward hydraulic gradient (acting as a stabilizing seepage force) under shear forces, decreasing the erosion rate.

As noted in Chapter 1, the present research is part of a 4-PhD interdisciplinary project titled 'Understanding Flow Slides in Flood Defences (MPM-Flow)' aiming at the improvement of the Material Point Method (MPM) numerical method to simulate flow slides. In this respect, the direct measurements acquired during the experimental work conducted within this study, together with the other measurements obtained within the whole project, may be utilized for the validation of MPM simulations or other numerical models employed to simulate flow slides. In view of the findings of the current study, model requirements to properly simulate breaching flow slides can be derived. Briefly, the numerical model must have the ability to:

- reproduce two-phase interactions including water, saturated soil, and sediment erosion and deposition,
- identify the soil-water interface, update the bed morphological changes and allow for the movement of the breach face,
- reproduce the dilative behavior of the soil and the build-up of the negative pressure in the soil body,
- model large deformations and reproduce the transition of the soil state from static to yielding for the simulation of the surficial slides,
- reproduce the hydrodynamics and turbulence behavior of the turbidity currents.

Based on these requirements, key directions for future research and development of the MPM may be defined.

6

Conclusions and Recommendations

This chapter presents a recapitulation of the main conclusions of this study followed by a number of suggestions for future experimental and numerical studies on the intriguing topic of breaching flow slides.

6.1. Conclusion

This study primarily aimed at improving the current understanding of the two-way coupled interaction between breaching-generated turbidity currents and the breach face during breaching flow slides by answering the following three key questions:

1. How do breaching-generated turbidity currents evolve along the breach face?
2. What is the influence of turbidity currents on the breaching process?
3. Can we develop an erosion closure model that adequately predicts the erosion during breaching? How should it be formulated?

To pursue the answers to the aforementioned questions, a series of novel large-scale experiments was carried out at the Laboratory of Fluid Mechanics of Delft University of Technology in an experimental setup designed specifically to study breaching flow slides. The experimental findings were complemented by conducting large eddy simulations of breaching-generated turbidity currents. The answers are presented here succinctly.

6.1.1. Research Question 1

During the lab experiments, direct measurements of flow thickness, velocities, and sediment concentrations were obtained, demonstrating the spatial and temporal development of the turbidity currents. In addition, time-varying profiles of the breach face were constructed, detailing the temporal failure evolution. The flow measurements visualize the physical structure of the velocity and sediment concentration within the flow. Similar to turbidity currents triggered by other mechanisms, the wall-normal velocity structure exhibits two

distinct regions: an inner region showing a positive velocity gradient and an outer region showing a negative velocity gradient. Whether the flow velocity at the breach face is zero or not remains an open question, as it has a dynamic nature, retrogressing constantly. The particle concentration within the flow was found to decay exponentially away from the breach face. High near-bed concentrations up to 0.5 by volume were observed. The study of the spatial development of the turbidity currents showed that the layer-averaged velocity of the turbidity current increases in the downstream direction along with the layer thickness and the suspended sediment concentration. Steeper slopes resulted in more powerful turbidity currents and larger flow thicknesses. In other words, currents propagating over steeper slopes have higher streamwise velocities together with larger volumes of water entraining into the flow.

6.1.2. RESEARCH QUESTION 2

The experimental results highlight the vital role of the associated turbidity currents in the failure evolution during breaching flow slides. It was found that these currents considerably increase the erosion down the breach face. On top of that, this promoted erosion increases the amount of suspended sediments captured by the flow and consequently makes it even more energetic, enabling it to pick up more sediments from the breach face, known as a self-accelerating behavior. Owing to the acceleration of the current and the increase of erosion downslope, the lower part of the breach face erodes more quickly than the upper part, resulting in the steepening of the breach face over time. This steepening leads to overhanging and the occurrence of a surficial slide where a coherent mass of sediment collapses. This mass disintegrates and is fed to the turbidity current, boosting its density and hence increasing its erosive capacity. Based on the findings of the existing body of research and the present study, the generated turbidity current seems to start dominating the breaching failure just after its onset until the ultimate deposition of the sediments, although breaching in the first place is a gravity-induced failure. Besides that the turbidity current considerably increases erosion and causes surficial slides, the run-out distance and hence the fate of the sediments are governed by the hydrodynamics of this current. Finally, and most importantly, the behaviour (i.e. depositional or erosional) of the turbidity current determines whether the breaching process is stable (the height of the breach face decreases over time) or unstable (the height of the breach face increases over time).

6.1.3. RESEARCH QUESTION 3

Undoubtedly, sediment erosion during breaching is a complicated process. This is because of the unique nature of this erosion involving particle-by-particle erosion induced by gravity, dilatancy-retarded erosion caused by high-concentration turbidity currents, and surficial slides. A good erosion closure model must account for the role of all these factors in the erosion process. Owing to the several challenges confronted during the lab experiments, it was not possible to directly quantify the flow-induced shear stress mainly through which the turbidity currents pick up sediments from the breach face. Consequently, an advanced 3D numerical tool was required to investigate the flow in more detail and to answer Research Question 3. A new erosion closure model was suggested within this study. Owing to the current limited understanding of the occurrence of surficial slides, their contribution to erosion was not accounted for in the erosion closure model put forward. Using large eddy simulations, this erosion closure model was validated against the experimental results and it

was shown that it has a good predictive ability. The qualitative and quantitative comparison between experimental and simulation results indicated that the proposed numerical tool can reasonably reproduce several substantial aspects of the breaching-generated currents. However, it fails to accurately predict the layer thickness of the flow. The numerical results confirm that breaching-generated turbidity currents are self-accelerating. Furthermore, the velocity, concentration, Reynolds stress, and turbulent kinetic energy profiles of these currents are found to take a self-similar shape. Based on a sensitivity analysis, sand erosion during breaching is found to be susceptible to the *in situ* porosity; denser sand shows higher resistance to erosion. It is believed that the present numerical model would serve as a good tool to predict the breaching evolution and stability, if it is further extended to include the downstream region and to update the morphological changes of the breach face.

6.2. RECOMMENDATIONS

Based on the findings of this study, some directions can be pointed out for future research. The recommendations are divided here into two categories: experimental and numerical.

6.2.1. EXPERIMENTAL STUDY

One single type of sand (d_{50} = 0.135 mm) was used in the lab experiments carried out within this study. Finer and courser grain sizes are recommended to be tested to study the effect of the grain size on the breaching process and the accompanying turbidity currents. Furthermore, the sand used in the experiments was uniformly graded. It is recommended to carry out laboratory experiments using sand containing different grain sizes, as that will be more comparable to the sand conditions in nature. This will also give insights into the effect of grain size distribution on the characteristics and structure of the flow.

The turbidity current makes a turn at the toe of the breach face and then travels down over the downstream region. A hydraulic jump may form somewhere at the transition between the breach face and the downstream region. Investigation of the current at this transition and also over the downstream region is of great relevance for a better prediction of the failure evolution and the run-out distance.

It has been shown in this study that the three-dimensionality plays an important role in the breaching process. Therefore, conducting three-dimensional experiments is recommended to improve our understanding of the failure and turbidity current evolution across the breach face. This in turn will result in a better prediction of the morphological changes during a breaching event.

The initial sandy slopes tested during the experiments were always steeper than the internal friction angle to guarantee that the slope will naturally fail under the impact of gravity. However, in reality, the slopes become steep due to a certain triggering mechanism. To date, as highlighted in Chapter 2, our understanding of such triggering mechanisms remains poor. It is recommended to investigate these experimentally. This will help develop appropriate initial and boundary conditions for numerical models.

The focus of the current experiments was on the hydraulic aspects of the problem. Nevertheless, breaching also involves geotechnical aspects. Therefore, it is recommended to design new experiments to obtain measurements within the sand body along with measurements within the flow including turbulence properties in order to gain a more insightful understanding of the problem in general and of the occurrence of surficial slides in particular. The latter is important to better predict the erosion during breaching and the change of the

hydrodynamics of the turbidity currents.

6.2.2. NUMERICAL STUDY

A limitation of the numerical model proposed in this study is the underestimation of the layer thickness of breaching-generated turbidity currents. It would be useful to explore the reason for this underestimation and to improve the model accordingly. This would enhance the accuracy of the numerical computations and thus the derived knowledge.

The current numerical model was designed to model the turbidity current running down the breach face. It is recommended to add the transition of the slope where the current makes a turn. This requires using a different erosion closure model at the downstream region, as the conditions there are different from the conditions at the breach face. The sand at the breach face is dense, where dilatancy retards the erosion, while the sand at the downstream region is loose, not showing a dilative behavior.

In the numerical simulations conducted within this research, the morphology of the breach face was not updated based on the local erosion. The model can be further developed to account for the morphology change, consequently allowing the prediction of temporal evolution of the failure and the accompanying current.

Given that soil is usually heterogeneous in real life, it would be useful to couple the simulation of breaching-generated turbidity currents to an advanced soil model accounting for the spatial difference in soil characteristics. This will in turn enhance the accuracy of numerical simulations.

REFERENCES

Akiyama, J., and Y. Fukushima (1985), Entrainment of noncohesive bed sediment into suspension, external memorandom no. 195, st, *Anthony Falls Hydraulic Laboratory, U. of Minnessota*.

Alhaddad, S., R. J. Labeur, and W. Uijttewaal (2019), The need for experimental studies on breaching flow slides, in *Proceedings of the second International Conference on the Material Point Method for Modelling Soil-Water-Structure Interaction*, (27), pp. 166–172.

Alhaddad, S., R. J. Labeur, and W. Uijttewaal (2020a), Breaching flow slides and the associated turbidity current, *Journal of Marine Science and Engineering*, *8*(2), 67.

Alhaddad, S., R. J. Labeur, and W. Uijttewaal (2020b), Large-scale experiments on breaching flow slides and the associated turbidity current, *Journal of Geophysical Research: Earth Surface*.

Alhaddad, S., R. J. Labeur, and W. Uijttewaal (2021), Preliminary evaluation of existing breaching erosion models, in *Proceedings of the tenth international conference on Scour and Erosion, Arlington, Virginia, October 17-20*.

Andrieux, O., C. K. Cooper, J. Wood, et al. (2013), Turbidity current measurements in the congo canyon, in *Offshore Technology Conference*, Offshore Technology Conference.

Azpiroz-Zabala, M., M. J. Cartigny, P. J. Talling, D. R. Parsons, E. J. Sumner, M. A. Clare, S. M. Simmons, C. Cooper, and E. L. Pope (2017), Newly recognized turbidity current structure can explain prolonged flushing of submarine canyons, *Science advances*, *3*(10), e1700,200.

Bagnold, R. A. (1962), Auto-suspension of transported sediment; turbidity currents, *Proceedings of the Royal Society of London. Series A. Mathematical and Physical Sciences*, *265*(1322), 315–319.

BBC (2018), Inskip Point: Section of Australian beach collapses into sea, https://www.bbc.com/news/world-australia-45622385, online; accessed 30-11-2019.

Beinssen, K., and D. R. Mastbergen (2017), Flow slides: Understanding their geo-mechanical mechanisms, the threats they pose and how these threats can be managed, in *13th Hydraulics in Water Engineering Conference*, p. 132, Engineers Australia.

Bisschop, F. (2018), Erosion of sand at high flow velocities: An experimental study, Ph.D. thesis, Delft University of Technology.

Bisschop, F., P. Visser, C. van Rhee, and H. J. Verhagen (2010), Erosion due to high flow velocities: A description of relevant processes, *Coastal Engineering Proceedings*, *1*(32), 24.

Bisschop, F., S. Miedema, P. Visser, G. Keetels, and C. van Rhee (2016), Experiments on the pickup flux of sand at high flow velocities, *Journal of Hydraulic Engineering, 142*(7), 04016,013.

Breusers, H. (1977), Hydraulic excavation of sand, *Proceedings International Course in Modern dreding*.

Cantero, M. I., M. Shringarpure, and S. Balachandar (2012), Towards a universal criteria for turbulence suppression in dilute turbidity currents with non-cohesive sediments, *Geophysical Research Letters*, *39*(14).

Carter, L., R. Gavey, P. J. TALLING, and J. T. Liu (2014), Insights into submarine geohazards from breaks in subsea telecommunication cables, *Oceanography*, *27*(2), 58–67.

Cenedese, C., and C. Adduce (2010), A new parameterization for entrainment in overflows, *Journal of Physical Oceanography*, *40*(8), 1835–1850.

Chu, J., M. Ho, W. Loke, and W. Leong (2004), Effects of scour and hydraulic gradient on the stability of granular soil slope, in *second international conference on scour and erosion, Singapore*.

Cossu, R., and M. G. Wells (2012), A comparison of the shear stress distribution in the bottom boundary layer of experimental density and turbidity currents, *European Journal of Mechanics-B/Fluids*, *32*, 70–79.

De Jager, R. (2018), Assessing liquefaction flow slides: beyond empiricism, Ph.D. thesis, Delft University of Technology.

de Wit, L. (2015), 3d cfd modelling of overflow dredging plumes, Ph.D. thesis, Delft University of Technology.

de Wit, L. (2019), 3d cfd modelling of hopper sedimentation, *CEDA dredging conference*.

de Wit, L., and C. van Rhee (2014), Testing an improved artificial viscosity advection scheme to minimise wiggles in large eddy simulation of buoyant jet in crossflow, *Flow, turbulence and combustion, 92*(3), 699–730.

de Wit, L., A. Talmon, and C. Van Rhee (2014a), 3d cfd simulations of trailing suction hopper dredger plume mixing: Comparison with field measurements, *Marine pollution bulletin*, *88*(1-2), 34–46.

de Wit, L., A. Talmon, and C. Van Rhee (2014b), 3d cfd simulations of trailing suction hopper dredger plume mixing: A parameter study of near-field conditions influencing the suspended sediment source flux, *Marine pollution bulletin, 88*(1-2), 47–61.

de Wit, L., C. van Rhee, and A. Talmon (2015), Influence of important near field processes on the source term of suspended sediments from a dredging plume caused by a trailing suction hopper dredger: the effect of dredging speed, propeller, overflow location and pulsing, *Environmental Fluid Mechanics, 15*(1), 41–66.

Deltares (2016), Conductivity type concentration meter, https://www.deltares.nl/app/uploads/2016/04/CCM-Conductivity-type-concentration-meter.pdf, online; accessed 15-08-2018.

Dey, S., and K. Debnath (2001), Sediment pickup on streamwise sloping beds, *Journal of irrigation and drainage engineering*, *127*(1), 39–43.

Dodd, M. S., and A. Ferrante (2014), A fast pressure-correction method for incompressible two-fluid flows, *J. Comput. Phys.*, *273*, 416–434, doi:10.1016/j.jcp.2014.05.024.

Dutta, S., C. Pantano-Rubino, M. I. Cantaero, M. H. Garcia, and G. Parker (2012), Effects of self-stratification on turbidity currents: A large eddy simulation approach, in *Proceedings of the XIX International Conference on Water Resources*, pp. 1–10.

Eggenhuisen, J. T., M. J. Cartigny, and J. de Leeuw (2017), Physical theory for near-bed turbulent particle suspension capacity., *Earth surface dynamics.*, *5*(2), 269–281.

Einstein, H. A. (1950), *The bed-load function for sediment transportation in open channel flows*, vol. 1026, Citeseer.

Eke, E., G. Parker, and R. Wang (2009), Breaching as a mechanism for generating sustained turbidity currents, in *33rd internation association of hydraulic engineering & research congress: water engineering for a sustainable environment, Vancouver, IAHR*.

Eke, E., E. Viparelli, and G. Parker (2011), Field-scale numerical modeling of breaching as a mechanism for generating continuous turbidity currents, *Geosphere*, *7*(5), 1063–1076.

Eke, E. C. (2008), Breaching as a mechanism for generating sustained turbidity currents, Master's thesis, University of Illinois at Urbana-Champaign.

Fukushima, Y., G. Parker, and H. Pantin (1985), Prediction of ignitive turbidity currents in scripps submarine canyon, *Marine Geology*, *67*(1-2), 55–81.

Garcia, M., and G. Parker (1991), Entrainment of bed sediment into suspension, *Journal of Hydraulic Engineering*, *117*(4), 414–435.

Garcia, M., and G. Parker (1993), Experiments on the entrainment of sediment into suspension by a dense bottom current, *Journal of Geophysical Research: Oceans*, *98*(C3), 4793–4807.

Goeree, J. (2018), Drift-flux modeling of hyper-concentrated solid-liquid flows in dredging applications, Ph.D. thesis, Delft University of Technology.

Gray, T. E., J. Alexander, and M. R. Leeder (2005), Quantifying velocity and turbulence structure in depositing sustained turbidity currents across breaks in slope, *Sedimentology*, *52*(3), 467–488.

Hadala, P. F., and V. Torrey (1989), Mississippi riverbank flowslides, *The Art and Science of Geotechnical Engineering*, pp. 13–30.

Hage, S., M. J. Cartigny, E. J. Sumner, M. A. Clare, J. E. Hughes Clarke, P. J. Talling, D. G. Lintern, S. M. Simmons, R. Silva Jacinto, A. J. Vellinga, et al. (2019), Direct monitoring reveals initiation of turbidity currents from extremely dilute river plumes, *Geophysical research letters*, *46*(20), 11,310–11,320.

Harlow, F. H., and J. E. Welch (1965), Numerical calculation of time-dependent viscous incompressible flow of fluid with free surface, *The physics of fluids*, *8*(12), 2182–2189.

Hizzett, J. L., J. E. Hughes Clarke, E. J. Sumner, M. Cartigny, P. Talling, and M. Clare (2018), Which triggers produce the most erosive, frequent, and longest runout turbidity currents on deltas?, *Geophysical Research Letters*, *45*(2), 855–863.

Hsu, S.-K., J. Kuo, C.-L. Lo, C.-H. Tsai, W.-B. Doo, C.-Y. Ku, and J.-C. Sibuet (2008), Turbidity currents, submarine landslides and the 2006 pingtung earthquake off sw taiwan., *Terrestrial, Atmospheric & Oceanic Sciences*, *19*(6).

Hu, P., and Z. Cao (2009), Fully coupled mathematical modeling of turbidity currents over erodible bed, *Advances in Water Resources*, *32*(1), 1–15.

Inman, D. L., C. E. Nordstrom, and R. E. Flick (1976), Currents in submarine canyons: An air-sea-land interaction, *Annual Review of Fluid Mechanics*, *8*(1), 275–310.

Islam, M. A., J. Imran, C. Pirmez, and A. Cantelli (2008), Flow splitting modifies the helical motion in submarine channels, *Geophysical Research Letters*, *35*(22).

Jonkman, S., and T. Schweckendiek (2015), Flood defences, *Lecture Notes CIE5314. Delft: Delft University of Technology*.

Kafaji, I. K. a. (2013), *Formulation of a dynamic material point method (MPM) for geomechanical problems*.

Kneller, B., and C. Buckee (2000), The structure and fluid mechanics of turbidity currents: a review of some recent studies and their geological implications, *Sedimentology*, *47*, 62–94.

Kneller, B. C., S. J. Bennett, and W. D. McCaffrey (1999), Velocity structure, turbulence and fluid stresses in experimental gravity currents, *Journal of Geophysical Research: Oceans*, *104*(C3), 5381–5391.

Komar, P. D. (1971), Hydraulic jumps in turbidity currents, *Geological Society of America Bulletin*, *82*(6), 1477–1488.

Koppejan, A., B. Van Wamelen, and L. Weinberg (1948), *Coastal flow slides in the Dutch province of Zeeland*.

Kramer, S. (1988), Triggering of liquefaction flow slides in coastal soil deposits, *Engineering Geology*, *26*(1), 17–31.

Krause, D. C., W. C. White, D. J. W. Piper, and B. C. Heezen (1970), Turbidity currents and cable breaks in the western new britain trench, *Geological Society of America Bulletin*, *81*(7), 2153–2160.

Kyrousi, F., A. Leonardi, F. Roman, V. Armenio, F. Zanello, J. Zordan, C. Juez, and L. Falcomer (2018), Large eddy simulations of sediment entrainment induced by a lock-exchange gravity current, *Advances in Water Resources*, *114*, 102–118.

Lamb, M. P., W. E. Dietrich, and J. G. Venditti (2008), Is the critical shields stress for incipient sediment motion dependent on channel-bed slope?, *Journal of Geophysical Research: Earth Surface*, *113*(F2).

Lemmin, U., and T. Rolland (1997), Acoustic velocity profiler for laboratory and field studies, *Journal of Hydraulic Engineering*, *123*(12), 1089–1098.

Liu, J. T., Y.-H. Wang, R. J. Yang, R. T. Hsu, S.-J. Kao, H.-L. Lin, and F. H. Kuo (2012), Cyclone-induced hyperpycnal turbidity currents in a submarine canyon, *Journal of Geophysical Research: Oceans*, *117*(C4).

Locat, J., and H. J. Lee (2002), Submarine landslides: advances and challenges, *Canadian Geotechnical Journal*, *39*(1), 193–212.

Lucchese, L. V., L. R. Monteiro, E. B. C. Schettini, and J. H. Silvestrini (2019), Direct numerical simulations of turbidity currents with evolutive deposit method, considering topography updates during the simulation, *Computers & Geosciences*, *133*, 104,306.

Manninen, M., V. Taivassalo, and S. Kallio (1996), On the mixture model for multiphase flow vtt publications 288, *Technical Research Center of Finland*.

Mastbergen, D., and R. Schrijvershof (2016), Sedimentatiepatronen plaat van walsoorden na plaatval 22 juli 2014 [in dutch], *Tech. rep.*

Mastbergen, D., G. van den Ham, M. Cartigny, A. Koelewijn, M. de Kleine, M. Clare, J. Hizzett, M. Azpiroz, and A. Vellinga (2015), Multiple flow slide experiment in the westerschelde estuary, the netherlands, in *Submarine Mass Movements and Their Consequences*, pp. 241–249, Springer.

Mastbergen, D. R., and J. H. Van Den Berg (2003), Breaching in fine sands and the generation of sustained turbidity currents in submarine canyons, *Sedimentology*, *50*(4), 625–637.

Mastbergen, D. R., G. A. van den Ham, M. B. de Groot, T. van der Kaaij, and G. P. Peelen (2014), Retrograding breach flow slides in the netherlands: Observations and numerical modelling (powerpoint presentation).

Mastbergen, D. R., K. Beinssen, and Y. Nédélec (2019), Watching the beach steadily disappearing: The evolution of understanding of retrogressive breach failures, *Journal of Marine Science and Engineering*, *7*(10), 368.

Meiburg, E., and B. Kneller (2010), Turbidity currents and their deposits, *Annual Review of Fluid Mechanics*, *42*, 135–156.

Meiburg, E., S. Radhakrishnan, and M. Nasr-Azadani (2015), Modeling gravity and turbidity currents: computational approaches and challenges, *Applied Mechanics Reviews*, *67*(4), 040,802.

Middleton, G., and J. Southard (1984), Mechanics of sediment transport, *Society for Economic Paleontology and Mineralogy Short Course, 3*.

Miedema, S. A. (2016), Oe4607 introduction dredging engineering. msc offshore and dredging engineering delft university of technology 2nd edition.

Mulder, T., and J. Alexander (2001), The physical character of subaqueous sedimentary density flows and their deposits, *Sedimentology*, *48*(2), 269–299.

Mulder, T., J. P. Syvitski, and K. I. Skene (1998), Modeling of erosion and deposition by turbidity currents generated at river mouths, *Journal of Sedimentary Research*, *68*(1).

Mulder, T., S. Migeon, B. Savoye, and J.-C. Faugères (2001), Inversely graded turbidite sequences in the deep mediterranean: a record of deposits from flood-generated turbidity currents?, *Geo-marine letters*, *21*(2), 86–93.

Nicoud, F., and F. Ducros (1999), Subgrid-scale stress modelling based on the square of the velocity gradient tensor, *Flow Turbulence and Combustion*, *62*, 183–200, doi:10.1023/A:1009995426001.

Normandeau, A., P. Lajeunesse, G. St-Onge, D. Bourgault, S. S.-O. Drouin, S. Senneville, and S. Bélanger (2014), Morphodynamics in sediment-starved inner-shelf submarine canyons (lower st. lawrence estuary, eastern canada), *Marine Geology*, *357*, 243–255.

Nourazar, S., and M. Safavi (2017), Two-dimensional large-eddy simulation of density-current flow propagating up a slope, *Journal of Hydraulic Engineering*, *143*(9), 04017,035, doi:10.1061/(ASCE)HY.1943-7900.0001329.

Ottolenghi, L., and C. Adduce (2016), *LES investigation on entrainment in gravity currents, River Flow 2016: Iowa City, USA, July 11-14, 2016*, Crc Press.

Ottolenghi, L., C. Adduce, R. Inghilesi, V. Armenio, and F. Roman (2016), Entrainment and mixing in unsteady gravity currents, *Journal of Hydraulic Research*, *54*(5), 541–557.

Ottolenghi, L., C. Cenedese, and C. Adduce (2017), Entrainment in a dense current flowing down a rough sloping bottom in a rotating fluid, *Journal of Physical Oceanography*, *47*(3), 485–498.

Parker, G., Y. Fukushima, and H. M. Pantin (1986), Self-accelerating turbidity currents, *Journal of Fluid Mechanics*, *171*, 145–181.

Parker, G., M. Garcia, Y. Fukushima, and W. Yu (1987), Experiments on turbidity currents over an erodible bed, *Journal of Hydraulic Research*, *25*(1), 123–147.

Parsons, J. D., J. W. Bush, and J. P. Syvitski (2001), Hyperpycnal plume formation from riverine outflows with small sediment concentrations, *Sedimentology*, *48*(2), 465–478.

Paull, C. K., P. J. Talling, K. L. Maier, D. Parsons, J. Xu, D. W. Caress, R. Gwiazda, E. M. Lundsten, K. Anderson, J. P. Barry, et al. (2018), Powerful turbidity currents driven by dense basal layers, *Nature communications*, *9*(1), 1–9.

Pedocchi, F., and M. H. García (2012), Acoustic measurement of suspended sediment concentration profiles in an oscillatory boundary layer, *Continental Shelf Research*, *46*, 87–95.

Pelmard, J., S. Norris, and H. Friedrich (2018), Les grid resolution requirements for the modelling of gravity currents, *Computers Fluids*, *174*, 256 – 270, doi:https://doi.org/10.1016/j.compfluid.2018.08.005.

Piper, D. J., and W. R. Normark (2009), Processes that initiate turbidity currents and their influence on turbidites: a marine geology perspective, *Journal of Sedimentary Research*, *79*(6), 347–362.

Pirmez, C., and J. Imran (2003), Reconstruction of turbidity currents in amazon channel, *Marine and petroleum geology*, *20*(6-8), 823–849.

Pratson, L. F., J. Imran, G. Parker, J. P. Syvitski, and E. Hutton (2000), Aapg memoir 72/sepm special publication no. 68, chapter 6: Debris flows vs. turbidity currents: a modeling comparison of their dynamics and deposits.

Prosperetti, A., and G. Tryggvason (2007), *Computational Methods for Multiphase Flow*, Cambridge University Press.

Richardson, J., and W. Zaki (1954), Fluidization and sedimentation–part i, *Trans. Inst. Chem. Eng*, *32*, 38–58.

Rogers, J. D. (2012), Levees, http://web.mst.edu/~rogersda/levees/Mississippi%20Delta%20Region.htm, online; accessed 30-10-2018.

Salaheldin, T., J. Imran, M. Chaudhry, and C. Reed (2000), Role of fine-grained sediment in turbidity current flow dynamics and resulting deposits, *Marine Geology*, *171*(1-4), 21–38.

Salinas, J. S., M. Cantero, M. Shringarpure, and S. Balachandar (2019), Properties of the body of a turbidity current at near-normal conditions: 1. effect of bed slope, *Journal of Geophysical Research: Oceans*, *124*(11), 7989–8016.

Saremi, S. (2014), Density-driven currents and deposition of fine materials, Ph.D. thesis, Technical University of Denmark.

Schiereck, G. J., and H. Verhagen, J (2012), *Introduction to bed, bank and shore protection*, VSSD: Delft, the Netherlands.

Sequeiros, O. E. (2012), Estimating turbidity current conditions from channel morphology: A froude number approach, *Journal of Geophysical Research: Oceans*, *117*(C4).

Sequeiros, O. E., H. Naruse, N. Endo, M. H. Garcia, and G. Parker (2009), Experimental study on self-accelerating turbidity currents, *Journal of Geophysical Research: Oceans*, *114*(C5).

Sequeiros, O. E., R. Mosquera, and F. Pedocchi (2018), Internal structure of a self-accelerating turbidity current, *Journal of Geophysical Research: Oceans*, *123*(9), 6260–6276.

Shanmugam, G. (2018), Slides, slumps, debris flows, turbidity currents, and bottom currents: implications, *Earth Systems and Environmental Sciences, Elsevier Online Module*.

Silva, J. (2020), The influence of underwater embankment properties on breaching failures, Ph.D. thesis, Utrecht University.

Silvis, F., and M. d. Groot (1995), Flow slides in the netherlands: experience and engineering practice, *Canadian geotechnical journal*, *32*(6), 1086–1092.

Simpson, J. E. (1999), *Gravity currents: In the environment and the laboratory*, Cambridge university press.

Smith, J. D., and S. McLean (1977), Spatially averaged flow over a wavy surface, *Journal of Geophysical research*, *82*(12), 1735–1746.

Stagnaro, M., and M. B. Pittaluga (2014), Velocity and concentration profiles of saline and turbidity currents flowing in a straight channel under quasi-uniform conditions, *Earth Surface Dynamics*, *2*(1), 167.

Sulsky, D., Z. Chen, and H. L. Schreyer (1994), A particle method for history-dependent materials, *Computer methods in applied mechanics and engineering*, *118*(1-2), 179–196.

Talling, P. J., C. K. Paull, and D. J. Piper (2013), How are subaqueous sediment density flows triggered, what is their internal structure and how does it evolve? direct observations from monitoring of active flows, *Earth-Science Reviews*, *125*, 244–287.

Talling, P. J., J. Allin, D. A. Armitage, R. W. Arnott, M. J. Cartigny, M. A. Clare, F. Felletti, J. A. Covault, S. Girardclos, E. Hansen, et al. (2015), Key future directions for research on turbidity currents and their depositskey future directions for research on turbidity currents and their deposits, *Journal of Sedimentary Research*, *85*(2), 153–169.

Torrey III, V. H. (1988), Retrogressive failures in sand deposits of the mississippi river. report 2. empirical evidence in support of the hypothesized failure mechanism and development of the levee safety flow slide monitoring system, *Tech. rep.*, Army Engineer Waterways Experiment Station Vicksburg Ms Geotechnical Lab.

Turner, J. (1986), Turbulent entrainment: the development of the entrainment assumption, and its application to geophysical flows, *Journal of Fluid Mechanics*, *173*, 431–471.

Van den Berg, J., A. Martinius, and R. Houthuys (2017), Breaching-related turbidites in fluvial and estuarine channels: Examples from outcrop and core and implications to reservoir models, *Marine and Petroleum Geology*, *82*, 178–205.

Van Den Berg, J. H., A. Van Gelder, and D. R. Mastbergen (2002), The importance of breaching as a mechanism of subaqueous slope failure in fine sand, *Sedimentology*, *49*(1), 81–95.

Van den Ham, G. A., M. B. de Groot, and D. R. Mastbergen (2014), A semi-empirical method to assess flow-slide probability, in *Submarine mass movements and their consequences*, pp. 213–223, Springer.

Van der Schrieck, G. (2012), Lecture notes dredging technology, *Delft University of Technology*.

Van Duinen, A., A. Bezuijen, G. van den Ham, and V. Hopman (2014), Field measurements to investigate submerged slope failures, in *Submarine mass movements and their consequences*, pp. 13–21, Springer.

Van Rhee, C. (2002), On the sedimentation process in a trailing suction hopper dredger, Ph.D. thesis, Delft University of Technology.

Van Rhee, C. (2010), Sediment entrainment at high flow velocity, *Journal of hydraulic engineering*, *136*(9), 572–582.

Van Rhee, C. (2015), Slope failure by unstable breaching, in *Proceedings of the Institution of Civil Engineers-Maritime Engineering*, vol. 168, pp. 84–92, Thomas Telford Ltd.

Van Rhee, C. (2019), Simulation of the breaching process – experimental validation, in *Proceedings of the 22nd World Dredging Conference, Changhai, China*.

Van Rhee, C., and A. Bezuijen (1998), The breaching of sand investigated in large-scale model tests, in *Coastal Engineering 1998*, pp. 2509–2519.

Van Rhee, C., and A. Talmon (2010), Sedimentation and erosion of sediment at high solids concentration, in *Proceedings of the 18th International Conference on Hydrotransport*, pp. 211–222, BHR Group, Cranfield, UK.

Van Rijn, L. C. (1984), Sediment pick-up functions, *Journal of Hydraulic Engineering*, *110*(10), 1494–1502.

Weij, D. (2020), On the modelling of the unstable breaching process, Ph.D. thesis, Delft University of Technology.

Weij, D., G. Keetels, J. Goeree, and C. Van Rhee (2016), An approach to research of the breaching process, *Proceedings of the WODCON XXI, Miami, FL, USA*, pp. 13–17.

Winterwerp, J. C., W. T. Bakker, D. R. Mastbergen, and H. van Rossum (1992), Hyperconcentrated sand-water mixture flows over erodible bed, *Journal of Hydraulic Engineering*, *118*(11), 1508–1525.

Wobbes, E. (2019), Algorithmic improvements of the material-point method and taylor least-squares function reconstruction, Ph.D. thesis, Delft University of Technology.

Xu, J., M. Noble, and L. K. Rosenfeld (2004), In-situ measurements of velocity structure within turbidity currents, *Geophysical Research Letters*, *31*(9).

Yeh, T.-h., M. Cantero, A. Cantelli, C. Pirmez, and G. Parker (2013), Turbidity current with a roof: Success and failure of rans modeling for turbidity currents under strongly stratified conditions, *Journal of Geophysical Research: Earth Surface*, *118*(3), 1975–1998.

Yi, A., and J. Imran (2006), The role of erosion rate formulation on the ignition and subsidence of turbidity current, in *Proceedings of the 4th IAHR symposium on River, Coastal and Estuarine Morphodynamics*, pp. 543–551.

You, Y. (2013), Dynamics of dilative slope failure, Ph.D. thesis, The University of Texas at Austin.

You, Y., P. Flemings, and D. Mohrig (2012), Dynamics of dilative slope failure, *Geology*, *40*(7), 663–666.

You, Y., P. Flemings, and D. Mohrig (2014), Mechanics of dual-mode dilative failure in subaqueous sediment deposits, *Earth and Planetary Science Letters*, *397*, 10–18.

Zordan, J., C. Juez, A. J. Schleiss, and M. J. Franca (2017), Experimental results on sediment entrainment by gravity currents, in *Proceedings of the 37th IAHR World Congress*, EPFL-CONF-230427, pp. 1453–1458.

Zordan, J., C. Juez, A. J. Schleiss, and M. J. Franca (2018), Entrainment, transport and deposition of sediment by saline gravity currents, *Advances in Water Resources*, *115*, 17–32.

ACKNOWLEDGEMENTS

First and above all, I would like to thank Allah, the Lord Almighty, for granting me the opportunity, determination and capability to conduct this research and for blessing me with very kind people who have been my support in my personal and academic life.

I would like to express my deep and sincere gratitude to my promotor Wim Uijttewaal and co-promotor Robert Jan Labeur for thier encouragement, guidance, academic support, valuable suggestions and insightful comments on my work. Wim, words are not adequate to thank you for believing in me and giving me the chance to carry out this research. Robert Jan, thank you for teaching me how to conduct proper research and for critically reviewing my papers and dissertation. Not only did your supervision promote the quality of my research, but also my own way of thinking.

I was very pleased to cooperate with Lynyrd de Wit in conducting the large eddy simulations. Lynyrd, many thanks for providing me with your code, for the fruitful discussions we had, and for your quick responses even outside your working hours. Furthermore, I would like to thank my project colleagues, Marco Bolognin and Joana Silva, for the interesting discussions. I would also like to thank the members of my doctoral committee for reading my dissertation and taking part in the PhD defense.

A special acknowledgement is necessary for Sander de Vree, Jaap van Duin, Arno Doorn, Pieter van der Gaag, Frank Kalkman and Rob van Dijk for their technical support throughout my experimental work. My experiments would not have been successful without your assistance.

I wish to express my deep appreciation to my friends and colleagues Stuart Pearson and Alejandra Mancheño. Thank you so much for being such great friends, for your continuous support, and of course for the nice weekend's dinners. Stuart, I remember that my English was weak when I first met you in September, 2014. You have played a major role in improving my English, in particular my writing skills. Thanks a lot for being always willing to give me feedback on my writing. I would also like to thank my friend Tolga Cömert for helping me write the summary of this dissertation in Dutch and my friend Mohammed Almadhoun for designing the cover page of this dissertation.

I owe everything to my lovely parents, who encouraged and helped me at every single step of my personal and academic life and longed to see this achievement comes true. Mom and Dad, thank you for your sincere prayers. Although you were not physically present with me during my PhD journey, I know your kind heart was always with me. There is no greater blessing in my life than you, my wonderful parents. My heartfelt gratitude is due to my loving brothers and sisters for their encouragement and perpetual love.

My deep appreciation goes to Hadda Machouahi for her endless assistance and for being always ready to lend a helping hand. My dear Hadda, how nice was to know you! Since then, I truly feel that I have a family in the Netherlands. I have difficulties finding the right words to express my gratitude to you, but I really hope that I can repay your kindness and favour.

I would like to convey my immense and special thanks to my lovely wife, Nour. Thanks a lot for bearing with me since we married and for sharing my sad and happy moments. You

were always there for me when times got hard, telling me the words I genuinely needed to hear to keep going. My life is now much more beautiful with you and our newborn son, Mousa.

Last but not least, I gratefully acknowledge the The Dutch Research Council (NWO Dutch: Nederlandse Organisatie voor Wetenschappelijk Onderzoek) for funding my PhD work and make it possible.

Said M. S. Alhaddad
Delft, August 19, 2020

LIST OF FIGURES

LIST OF TABLES

CURRICULUM VITÆ

Said M. S. ALHADDAD

20-02-1991 Born in Gaza, Palestine.

EDUCATION

2008–2013 Bachelor of Science (BSc.), Civil Engineering
Islamic University of Gaza (IUG), Palestine.

2014–2016 Master of Science (MSc.), Coastal and Marine Engineering and Management
Norwegian University of Science and Technology (NTNU), Trondheim, Norway,
Delft University of Technology, The Netherlands.

2016-2020 Doctor of Philosophy (PhD)
Delft University of Technology, The Netherlands.
Thesis: Breaching Flow Slides and the Associated Turbidity Currents: Large-Scale Experiments and 3D Numerical Modelling
Promotor: Prof. dr. W.S.J Uijttewaal
Copromotor: Dr. R.J Labeur

AWARDS

2009 IUG Honour Scholarship

2011 Award of World Assembly of Muslim Youth

2012 Award of IUG Creative Projects

2014 Erasmus Mundus Full Scholarship

List of Publications

Journal Publications

3. **S. Alhaddad**, R.J. Labeur, L. de Wit and W. S. J. Uijttewaal, *Modelling of Breaching-Generated Turbidity Currents Using Large Eddy Simulations*, Journal of Marine Science and Engineering, **8 (9)**, 728 (2020).

2. **S. Alhaddad**, R.J. Labeur, and W. S. J. Uijttewaal, *Large-scale Experiments on Breaching Flow Slides and the Associated Turbidity Current*, Journal of Geophysical Research: Earth Surface **125**, e2020JF005582 (2020).

1. **S. Alhaddad**, R.J. Labeur, and W. S. J. Uijttewaal, *Breaching Flow Slides and the Associated Turbidity Current*, Journal of Marine Science and Engineering, **8 (2)**, 67 (2020).

Conference Proceedings

3. **S. Alhaddad**, R.J. Labeur, and W. S. J. Uijttewaal, *Preliminary Evaluation of Existing Breaching Erosion Models*, In Proceedings of the tenth international conference on Scour and Erosion, Arlington, Virginia October, 17-20 2021.

2. **S. Alhaddad**, R.J. Labeur, and W. S. J. Uijttewaal, *Large-Scale Experimental Investigation of Breaching Flow Slides*, NCK Days Conference, March 21 2019, Enkhuizen, the Netherlands, **pp. 25**.

1. **S. Alhaddad**, R.J. Labeur, and W. S. J. Uijttewaal, *The need for experimental studies on breaching flow slides*, In Proceedings of the second international conference on the material point method for modelling soil-water-structure interaction, Cambridge, UK, 8–10 January 2019, **pp. 166–172**.

Other Scientific Contributions

3. **S. Alhaddad**, R.J. Labeur, and W. S. J. Uijttewaal, *Soil-water interaction in breaching flow slides*, Flow Slides Symposium, 21 February 2018, Delft, The Netherlands.

2. **S. Alhaddad**, R.J. Labeur, and W. S. J. Uijttewaal, *Understanding Soil-water Interaction as Relevant to Flow Slides*, Poster at the winter school, 16-20 January 2017, Grenoble, France.

1. S. Pearson, I. Samardzija, **S. Alhaddad**, T. Amarachaharam, J. Darnall and A.M. Serrano, *Use of Compartment Dikes as a Flood Management Strategy in Schouwen-Duiveland*, Multidisciplinary Project, 2015, Delft University of Technology.